SAND2013-1412P

Thermomechanical-Hydrological and Chemical (TMHC) Model Development

(FCRD-UFD-2013-000064)

Fuel Cycle Research & Development

Prepared for
U.S. Department of Energy
Used Fuel Disposition Campaign

Carlos F. Jové Colón, Teklu Hadgu, James E. Bean, Mario J. Martinez, José G. Argüello, Christi Leigh, Francis D. Hansen (SNL)

December 14th, 2012

SAND 2012-XXXXX

Prepared by:

Sandia National Laboratories

Albuquerque, New Mexico 87185

Sandia National Laboratories is a multi-program laboratory managed and operated by Sandia Corporation, a wholly owned subsidiary of Lockheed Martin Corporation, for the U.S. Department of Energy's National Nuclear Security Administration under contract DE-AC04-94AL85000.

U.S. DEPARTMENT OF ENERGY

Sandia National Laboratories

AKNOWLEDGEMENTS

The authors acknowledge our gratitude to Charles R. Bryan (SNL), Greg Roselle (SNL), Yongliang Xiong (SNL), Larry Brush (SNL), Peter Swift (SNL), Kevin McMahon (SNL), William Spezialetti (DOE NE-53), Prasad Nair (DOE NE-53), Mark Tynan (DOE NE-53), and Tim Gunther (DOE NE-53) for their helpful discussions on topics covered in this report.

SUMMARY

Disposal of heat generating waste in salt is one of the alternatives to be investigated as part of a generic approach towards the assessment of high level waste (HLW) long-term disposition. The assessment of generic Engineering Barrier System (EBS) concepts also comprises the analysis of salt and material responses to heating in the analysis of barrier performance. This analysis takes advantage of sophisticated approaches to the evaluation of EBS processes through the use and/or development of modeling methodologies to evaluate coupled physico-chemical phenomena. The main goal of this activity is to leverage existing computational models and tools to evaluate, and when possible, coupled TM and TH phenomena in salt under subsurface repository conditions, with the added focus on brine accessibility and moisture transport. The chemistry of brine-salt interactions is analyzed through thermodynamic analysis of multiphase multicomponent chemical equilibria as a function of solution concentration and temperature. The current evaluation of key processes to EBS performance in this report is presented as follows:

- **(Part I) Geochemical Aspects of Brine Evaporation Chemistry and Solubilities at Elevated Temperatures** – Geochemical approaches to the modeling of brine evaporation elucidate important chemical trends as a function of evaporation extent. This analysis allows for the retrieval of thermodynamic constants through mapping of invariant point equilibrium compositions of multiphase mineral salt assemblages. Further, the analysis of soluble salts in the Mg-Cl-H_2O system permits the evaluation of $MgCl_2$ hydrate salt solubility as a function of temperature and the generation of acidic brines.
- **(Part II) First Principles Modeling of Complex Salts** –Exploitation of first principle approaches permits the rigorous theoretical analysis of thermal properties for complex salts on the system K-Mg-Cl-H_2O when this data is either lacking or hard to obtain. Thermal properties at constant, equilibrium volume (i.e., the total energy U, the phonon (Helmholtz) free energy F, entropy S, and isochoric heat capacity C_v) and at constant pressure (i.e., the Gibbs energy G and isobaric heat capacity C_P) were reported. These properties are based on density functional perturbation theory calculations.
- **(Part III) Coupled Thermal-Mechanical (TM) Modeling of Salt** – This work investigates the effects of variable heat loading on salt mechanical response that could affect alcove closure rate. These TM analyses provide estimates of the time for the crushed salt backfill to compact to levels approaching intact salt density.
- **(Part IV) Thermal-Hydrologic and Thermal-Hydrologic-Mechanical Modeling** – Three-dimensional simulations were carried out to further understand the thermally driven processes affecting Thermo-Mechanical (TM), Thermo-Hydrology (TH), and coupled THM modeling as a result of decaying heat from a waste package or canister. The simulations provided distributions of temperature, saturation and mass of vapor for different input conditions, predicting thermal and moisture front propagation. These also provided sensitivity of output to DRZ and crushed salt property parameters.

FCT Document Cover Sheet

Name/Title of Deliverable/Milestone	Thermomechanical-Hydrological and Chemical (TMHC) Model Development
Work Package Title and Number	DR Salt R&D - SNL / FT-13SN081803
Work Package WBS Number	1.02.08.18
Milestone Number	M3FT-13SN08180335
Responsible Work Package Manager	Carlos F. Jove Colon (Name/Signature)
	December 14, 2012 (Date Submitted)

Quality Rigor Level for Deliverable/Milestone	☒ QRL-3	☐ QRL-2	☐ QRL-1 ☐ Nuclear Data	☐ N/A*

This deliverable was prepared in accordance with Sandia National Laboratories *(Participant/National Laboratory Name)*

QA program which meets the requirements of
☐ DOE Order 414.1 ☐ NQA-1-2000 ☒ Other: DOE QA Order

This Deliverable was subjected to:
☒ Technical Review ☐ Peer Review

Technical Review (TR)
Review Documentation Provided
☐ Signed TR Report, or
TR Report No.: _____
☐ Signed TR Concurrence Sheet (attached), or
☒ Signature of TR Reviewer(s) below

Peer Review (PR)
Review Documentation Provided
☐ Signed PR Report, or
PR Report No.: _____
☐ Signed PR Concurrence Sheet (attached), or
☐ Signature of PR Reviewers below

Name and Signature of Reviewers

(Name/Signature)	(Date)
Andrew W. Miller	12/13/2012

*Note: In some cases there may be a milestone where an item is being fabricated, maintenance is being performed on a facility, or a document is being issued through a formal document control process where it specifically calls out a formal review of the document. In these cases, documentation (e.g., inspection report, maintenance request, work planning package documentation, or the documented review of the issued document through the document control process) of the completion of the activity along with the Document Cover Sheet is sufficient to demonstrate achieving the milestone. QRL for such milestones may also be marked N/A in the work package provided the work package clearly specifies the requirement to use the Document Cover Sheet and provide supporting documentation.

CONTENTS

Part IV - Thermal-Hydrologic and Thermal-Hydrologic-Mechanical Modeling

FIGURES

Part I - Geochemical Aspects of Brine Evaporation Chemistry and Solubilities at Elevated Temperatures

Part II - First Principles Modeling of Complex Salts

Part III - Coupled Thermal-Mechanical (TM) Modeling of Salt

Part IV - Thermal-Hydrologic and Thermal-Hydrologic-Mechanical Modeling

TABLES

Part I - Geochemical Aspects of Brine Evaporation Chemistry and Solubilities at Elevated Temperatures

Part III - Coupled Thermal-Mechanical (TM) Modeling of Salt

Part IV - Thermal-Hydrologic and Thermal-Hydrologic-Mechanical Modeling

ACRONYMS

3D	Three Dimensional
DFT	Density Functional Theory
DFPT	Density Functional perturbation Theory
DOE	Department of Energy
DOS	Densities of States
DRZ	Disturbed Rock Zone
EBS	Engineered Barrier System
EDZ	Excavated Disturbed Zone
ERZ	Excavated Rock Zone
FCRD	Fuel Cycle Research and Development
FEP	Features, Events, and Processes
GGA	Generalized Gradient Approximation
HLW	High-Level nuclear Waste
KS	Kohn-Sham
MT	Metric Ton
NBS	Natural Barrier System
NE	DOE-Nuclear Energy
PA	Performance Assessment
RD&D	Research, Development, and Demonstration
R&D	Research and Development
RDO	Repository Design Optimization
RH	Relative Humidity
SNL	Sandia National Laboratories
THM	Thermal-Hydrological-Mechanical
TM	Thermal-Mechanical
THMC	Thermal-Hydrological-Mechanical-Chemical
UFDC	Used Fuel Disposition Campaign
VASP	Vienna *ab initio* simulation package
WIPP	Waste Isolation Pilot Plant
XRD	X-ray Diffraction
YMP	Yucca Mountain Project

Geochemical Aspects of Brine Evaporation Chemistry and Solubilities at Elevated Temperatures

(Part I)

1. Importance of Coupled Processes for HLW Disposal in Salt

1.1 Introduction

The U.S. Department of Energy's Office of Nuclear Energy (DOE-NE) has adopted a generic approach to evaluate potential disposal pathways for high-level radioactive wastes that currently have no disposal options in the United States. This includes both high-level radioactive waste (HLW) and spent nuclear fuel (SNF) from both commercial nuclear power generation and atomic energy defense activities. Disposal in salt has been considered as potential option for long-term disposition of heat-generating nuclear waste. The engineered barrier system (EBS) includes all material comprised within the excavated disposal domain including waste package, backfill (buffer if considered), and liners/seals. Post-closure analysis and development of long-term repository design concepts for the safety assessment is an iterative process that combines the results of field, laboratory, and modeling studies. This information is key to the adequate evaluation of predictive methods and approaches when analyzing responses to model input parameters affecting the performance of repository key elements such as the EBS. For this reason, the importance of evaluating the predictive capability of THMC process models based on information gathered from engineered barrier experiments has been emphasized by researchers in European and USA nuclear waste repository programs (Gens et al., 2010; Gens et al., 2009; Guimaraes et al., 2007; Guimaraes et al., 2006, 2010; Olivella et al., 2011; Rutqvist et al., 2009a; Rutqvist et al., 2008; Rutqvist et al., 2009b; Rutqvist et al., 2011; Rutqvist et al., 1991). Another important aspect is the passing of information between the near-field and process models from other domains such as the far-field.

Crushed salt backfill is the main barrier material in close contact with the waste package and it has very different properties from that envisioned for clay and crystalline rock. The safe containment and long-term isolation of nuclear waste in salt is strongly reliant on the consolidation and thermal properties of the salt media, whether intact or in crushed form. Crushed salt is initially porous and can have relatively small amounts of water present in pores or adsorbed at solid surfaces. In addition, brine pockets and fluid inclusions can produce solutions that can be mobilized by heat generating waste. Therefore, thermal-Hydrological-Mechanical-Chemical (THMC) processes that are coupled can manifest in various spatial and time scales in this disposal environment. Figure 1 shows the main processes affecting EBS materials in the near-field along with information interfacing between the far-field and waste package process models for these domains. It also illustrates the transport and chemical couplings that can affect EBS performance noting their importance when quantifying fluxes between the near- and far-field domains.

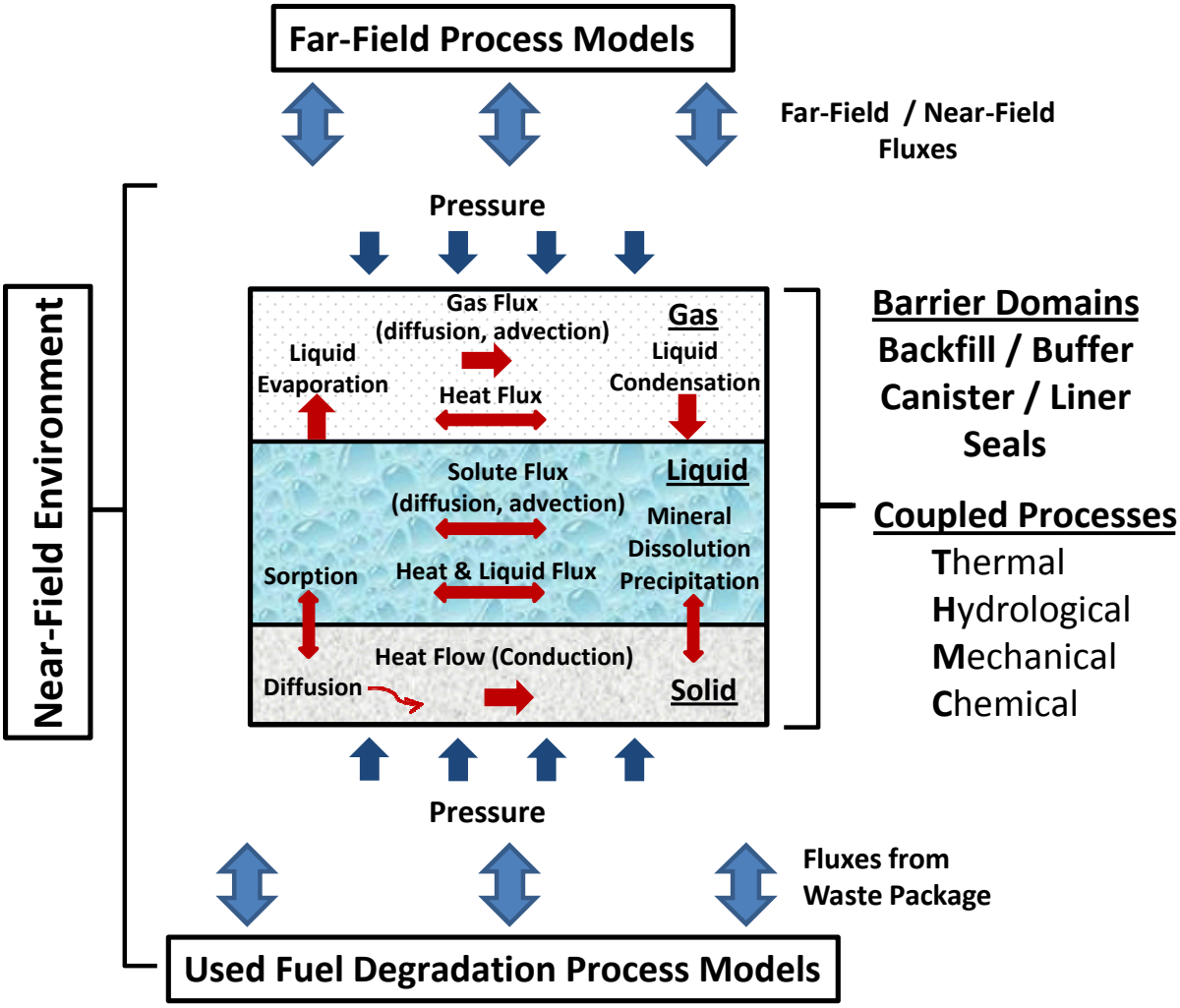

Figure 1. EBS coupled process phenomena (center) and interrelations between process models from other domains (modified after Olivella et al. 2011)

The high ranking of EBS processes affecting barrier performance and their role on radionuclide transport are described in the UFDC Disposal R&D Roadmap report (Nutt et al., 2011). These topics include waste form, THM processes, waste container, radionuclide speciation and solubility, and buffer/backfill material. The priority rankings for EBS components such as buffer/backfill and seal/liner materials are summarized in Table 1 after buffer/backfill and seal/liner materials. This effort will examine the thermodynamics of salt phase equilibria in the multicomponent system Ca-K-Mg-Na-Cl-SO_4-H_2O with thermodynamic data sets applicable to a wide range of temperatures. Such effort could expand and refine existing thermodynamic databases for this salt system at elevated temperatures and identify potential knowledge gaps in the evaluation of brine interactions at these conditions. The results of this effort should include geochemical evaluation of experimental data sets generated at elevated temperatures from various WIPP test programs (observations of acid brine generation from past heater test experiments).

Table 1. Summary of the priority ranking for the EBS for buffer/backfill and seal/liner materials with associated FEPs (Nutt et al., 2011).

BUFFER / BACKFILL (media type) →	Clay	Salt	Crystalline	Mixed Materials
2.1.04.01: BUFFER/BACKFILL	High	Medium	Medium	Medium
2.1.07.02, .03, .04, 09: MECHANICAL PROCESSES	Medium	Medium	Medium	Medium
2.1.08.03, .07, .08: HYDROLOGIC PROCESSES	Medium	Medium	Medium	Medium
2.1.09.01, .03, .07, .09, .13: CHEMICAL PROCESSES - CHEMISTRY	Medium	Medium	Medium	Medium
- Radionuclide speciation/solubility	High	High	High	High
2.1.09.51, .52, .53, .54, .55, .56, .57, .58, .59, .61: CHEMICAL PROCESSES – TRANSPORT	Medium	Medium	Medium	Medium
- Colloid facilitated transport	Low	Low	Low	Low
2.1.11.04: THERMAL PROCESSES	Medium	Medium	Medium	Medium
2.1.12.01, .02, .03: GAS SOURCES AND EFFECTS	Medium	Medium	Low	Low
SEAL / LINER MATERIALS →	**Cement**	**Asphalt**	**Metal**	**Polymer**
2.1.05.01: SEALS	Medium	Medium	Medium	Medium
2.1.07.02, .08, .09: MECHANICAL PROCESSES	Medium	Medium	Medium	Medium
2.1.08.04, .05, .07, .08, .09: HYDROLOGIC PROCESSES	Low	Low	Low	Low
- Flow through seals	Medium	Medium	Medium	Medium
2.1.09.01, .04, .07, .09, .13: CHEMICAL PROCESSES – CHEMISTRY	Medium	Medium	Medium	Medium
- Radionuclide speciation/solubility	High	High	High	High
- Advection, diffusion, and sorption	Medium	Medium	Medium	Medium
2.1.11.04: THERMAL PROCESSES	Medium	Medium	Medium	Medium

Note:

1. FEP number lists delimited by commas show only the change in the fourth field of the FEP

Brine availability in the disposal system may occur as a consequence of the TMH response of the salt due to excavation and emplacement of heat-generating waste. Also, high temperatures can result in decrepitation of fluid inclusions that can release trapped brine. Characterization of brine chemistry has been conducted through testing done as part of the WIPP located in southeast New Mexico (Lambert, 1992; Stein and Krumhansl, 1988). Relatively little work has been done evaluating this information in the context of generic salt disposal applications to assess the usefulness of these data.

The potential effects of brine chemistry and its importance to high temperature interactions within the context of waste material experimentation are described by Molecke (1983). The report by Molecke (1983) author also evaluates the potential for acid brine formation based on the brine-mineral equilibria of salt solids in the $MgCl_2$-H_2O system as function of temperature. The occurrence of acid brine formation can have deleterious corrosion effects when contacting metallic barrier materials including waste canister. In addition, temperatures in the excavated disturbed zone, permeability generation and healing, reduction in permeability of crushed salt, and temperature distribution at a large scale will be evaluated. The accurate representation and interplay of these coupled processes lead towards a comprehensive assessment of the generation and fate brine and associated moisture transport in salt. Also, the potential coexistence of acid brine with salt solids needs to be evaluated to assess the complex nature of solution-mineral equilibria in multicomponent systems.

1.2 Evaluation of Brine Chemistry in Salt Formations: Fluid Inclusions and Brine Seeps

Bedded and domal salt deposits are geologic evidence of large-scale basinal evaporation processes whether these are of marine or non-marine origin. The formation of these geologic deposits has been the subject of many studies (Hsü, 1972; Lotze, 1957; Zharkov and I□A□nshin, 1981) and their origins from evaporite-related processes has been comprehensively evaluated from the standpoint of major ion (Mg^{++}, Ca^{++}, Na^{+}, K^{+}, SO_4^{--}, Cl^{-}) brine chemistry and salt mineral phase relations (Braitsch, 1971; Hardie, 1968, 1982, 1984, 1991, 1996; Hardie and Lowenstein, 2004; Kovalevych et al., 2002; Lowenstein and Hardie, 1985; Lowenstein et al., 2003; Lowenstein et al., 2001). The major ion chemistry of brines trapped in halite fluid inclusions has been used to study variations in seawater chemistry from ancient evaporite basinal deposits in locations from around the world (Ayora et al., 1994; Bein et al., 1991; Cendon et al., 2008; Cendon et al., 2006; Demicco et al., 2005; Garcia-Veigas et al., 2011; Garcia-Veigas et al., 1992; Hardie, 1996, 1998; Horita et al., 2002; Kovalevich et al., 1998; Lowenstein and Timofeeff, 2008; Lowenstein et al., 2005; Roedder et al., 1987; Stein and Krumhansl, 1988; Timofeeff et al., 2001; Timofeeff et al., 2006). Krupp (2005) studied the chemistry of brines from seeps and confined as groundwater pockets in potash-bearing deposits (Riedel mine; domal salt). Lambert (1992), and Stein and Krumhansl (1988) studied brines and fluid inclusions, respectively, of the Salado (bedded salt) formation in southeastern New Mexico. These studies on brine chemistry emphasize the importance of the water-rock interactions resulting in salt dissolution and alteration of the evaporite deposits. Such diagenetic alteration of the evaporite rock can result in salt recrystallization and thus trapping of fluids that are of non-marine origin (Stein and Krumhansl, 1988). The chemistry of such diagenetic fluid inclusions can be markedly different from primary inclusions of marine origin and could result in scattering of solution chemistry data and alteration of evaporation trends. A major aspect of brine chemistry trapped in salt rock fluid inclusions is the immediate contact of this fluid with heat generating waste in a disposal alcove backfilled with crushed salt. As stated previously, many studies in the last two decades have been devoted to the characterization of major ion chemical trends on analyzed fluid

inclusions to elucidate secular variations in seawater chemistry (Lowenstein et al., 2005). The geologic significance of such variations in seawater chemistry (although quite interesting) is beyond the scope of the current analysis. On the other hand, such characterization studies provide a wealth of fluid inclusion chemical data representative of evaporative chemical trends reaching very concentrated levels. These brine chemistry trends are key for the following reasons:

- It provides a wide-ranging geochemical mapping of evaporative fluid chemistries in salt deposits.
- Such geochemical mapping can serve as a "roadmap" for the expected evaporation trends that could result from brine heating.
- These data sets can be used in the testing and validation of geochemical code predictions in the evolution of brine chemistry as a result of brine evaporation.
- Further, this test and validation of theoretical approaches to describe vapor-solution-mineral equilibria is important in the mapping of invariant point solution composition typical of multiphase multicomponent salt systems.

Given their rather extreme concentrations, the focus of the current study is on $MgCl_2$-rich brines and their relevance to potentially produce acidic brines. The occurrence of magnesium chloride brines is rare and it's mainly restricted to fluid inclusions. However, there is an example of magnesium chloride brine seeps from the Riedel mine (Zechstein era; Germany) as reported by Krupp (2005). This author also notes the worldwide occurrence of thick bischofite ($MgCl_2 \bullet 6H_2O$) deposits suggesting a less rare occurrence of concentrated magnesium chloride brines in evaporite deposits.

1.3 Compositional Mapping and Reaction Path Modeling of Concentrated Magnesium Brines from Fluid Inclusion and Brine Chemistry Data

The data collected from the aforementioned studies focuses on the chemistry of brine trapped in fluid inclusions in salt deposits. These data is based on the analysis primary brine inclusions, that is, those generated by evaporation of primordial seawater, and not from subsequent salt recrystallization or altered samples. This type of brine inclusion provides the brine chemistry used to resolve seawater evaporation paths considered by these authors. The work of Timofeeff et al. (2001) exemplifies the approach needed in the chemical analysis of fluid inclusion to establish the validity of characterizing ancient seawater chemistry. Advancements in the microscopic analysis of small fluid inclusions have greatly improved the compositional characterization of primary brines trapped in halite (Lowenstein et al., 2001; Timofeeff et al., 2001). Lowenstein et al. (2001) evaluated the systematic changes in brine inclusion chemistry in halite samples obtained from various worldwide locations and ages. An important observation of Lowenstein et al. (2001) is that none of the brine chemistries from ancient halite fluid inclusions and the defined evaporation trends resemble that of modern seawater evaporation. Seawater

evaporation trends from a primordial source (i.e., no recycling or alteration through nonmarine diagenetic interactions) are mainly determined by the brine major ion chemistry and the equilibrium with respect to salt phases throughout the evaporation path. Given the focus of the current study on $MgCl_2$-rich brines, the compiled data sets provide an exceptional opportunity to describe the chemistry of natural brines that have undergone very large extents of evaporation. It should be noted that the focus here is mainly on the magnesium chloride compositional mapping of evaporated brines and not in the variations of seawater chemistry in ancient times. This is discussed in detail by Lowenstein et al. (2001) and others.

The seawater evaporation data of McCaffrey et al. (1987) was used as the base-case for modern seawater evaporation. These data is from the Morton solar salt ponds on Great Inagua Island, Bahamas, and has been considered as a reference compositional trend for evaporation of modern seawater. It has also been used for comparison with fluid inclusion chemical data for evaporated paleoseawater (Timofeeff et al., 2001). At the Morton solar salt facility, halite is precipitated by allowing seawater to evaporate in a series of reservoirs. The final brine achieves a concentration factor of about 40 with respect to seawater (Mariner, 2007; McCaffrey et al., 1987). The use of this data set has various advantages as the basis for modern seawater evaporation due to controls on meteoric influxes into these saline reservoirs thus preventing large mixing effects. Moreover, the evaporation data of McCaffrey et al. (1987) have been used in the Yucca Mountain Project (YMP) to validate the In-Drift Precipitates/Salts Model, salt solubility data, and the Pitzer database used in the modeling of evaporation paths (Mariner, 2007). The brine seep data of Krupp (2005) is also used in this study given its concentrated nature in magnesium chloride and it also represents a natural brine that have potentially undergone large extents of evaporation.

The compiled brine chemistry data is depicted in Figure 2a. Notice that three distinct trends can be defined on the basis of magnesium chloride concentrations: modern seawater, Precambrian/Permian, and Cambrian/Silurian/Albian-Cenomanian. These trends are depicted better in Figure 2b without the data scatter. These geologic time designations are adopted in this work for consistency with Lowenstein et al. (2001) in the model comparisons. The different evaporative evolutionary trends are mainly due to differences in the primordial brine compositions. Brine chemistry can be altered during the evaporation path by mixing with other solution fluxes and/or in equilibrium with salt solids. The analysis of Krupp (2005) advances the scenario of having such mixing to then produce very concentrated brine seeps from the Riedel mine. An example of this will be given on the basis of reaction path modeling using the computer code EQ3/6 (version 8.0) (Wolery and Jarek, 2003) to generate evaporation trends and map the continuous changes in brine chemistry. The sources of thermodynamic data and their analysis are described in Mariner (2007) and Jové Colón (2005). The thermodynamic database inputs contain the necessary parameter data to conduct solution-salt equilibrium calculations at elevated temperatures. The evaporation trends generated by the EQ3/6 were conducted by reaction path modeling in reaction progress mode to progressively concentrate a starting seawater composition by removal of H_2O solvent mass. Details on the concepts of reaction path modeling as applied to solution-mineral interactions are given in Helgeson (1968, 1970). The

temperature used in the Great Inagua Island seawater evaporation runs is 31.25°C which is the average of the reported temperatures in the brine samples at this locality. Exploratory runs between this temperature and 25°C did not result in significant differences between evaporation path calculations. This temperature is consistent with the work of McCaffrey et al. (1987) for the seawater evaporation in solar ponds at this location. The extent of evaporation as a result of H_2O solvent removal is allowed to advance until the reaction path produces the equilibrium salt mineral assemblage to constrain the brine chemistry. This type of analysis requires the inclusion (and suppression) of minimal set of solids that accurately represents the equilibrium mineral assemblage of interest. If many solids in the chemical system of interest are allowed to precipitate throughout the reaction path calculation then the resulting evaporation trend would be affected. Therefore, the evaluation of mineral inclusion/suppression in the model input constraints needs to be reconciled with observed (or anticipated) salt mineral assemblage to obtain meaningful results. The salt mineralogy in bedded and domal salt deposits has been investigated in detail leading to simplified major mineral assemblages that closely corresponds to those adopted in this study.

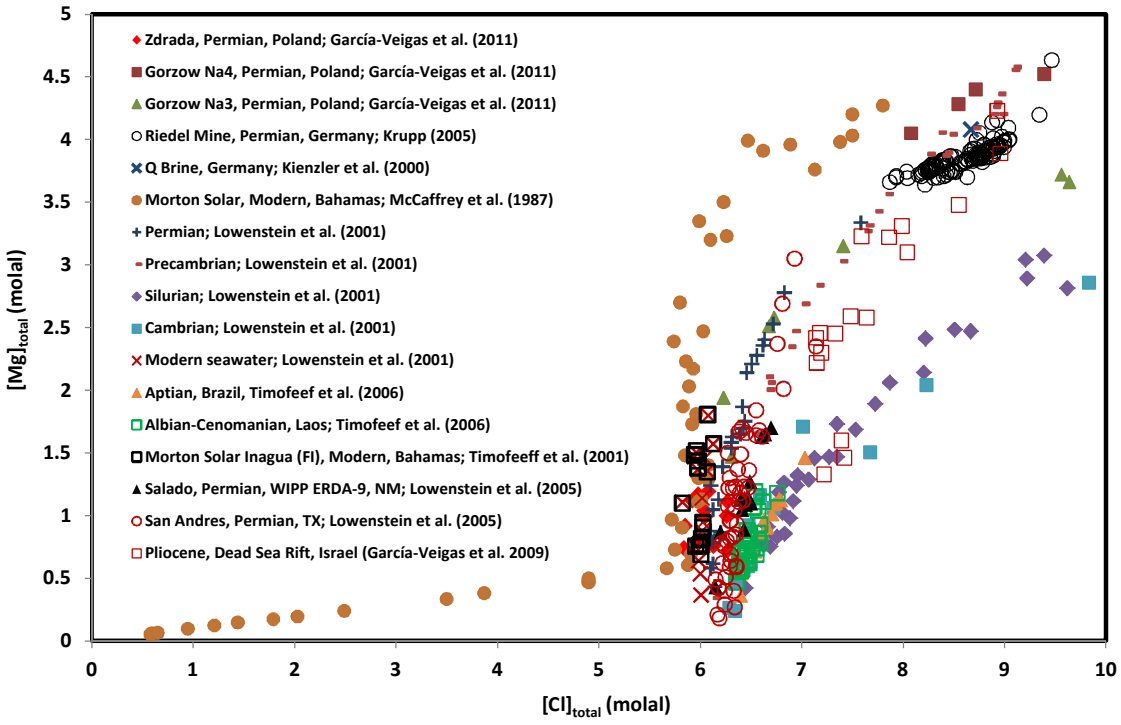

Figure 2a. Compilation of Mg and Cl concentrations from fluid inclusion and brine chemistry. The data by Lowenstein et al. (2001) with geologic time designations only comprises various localities.

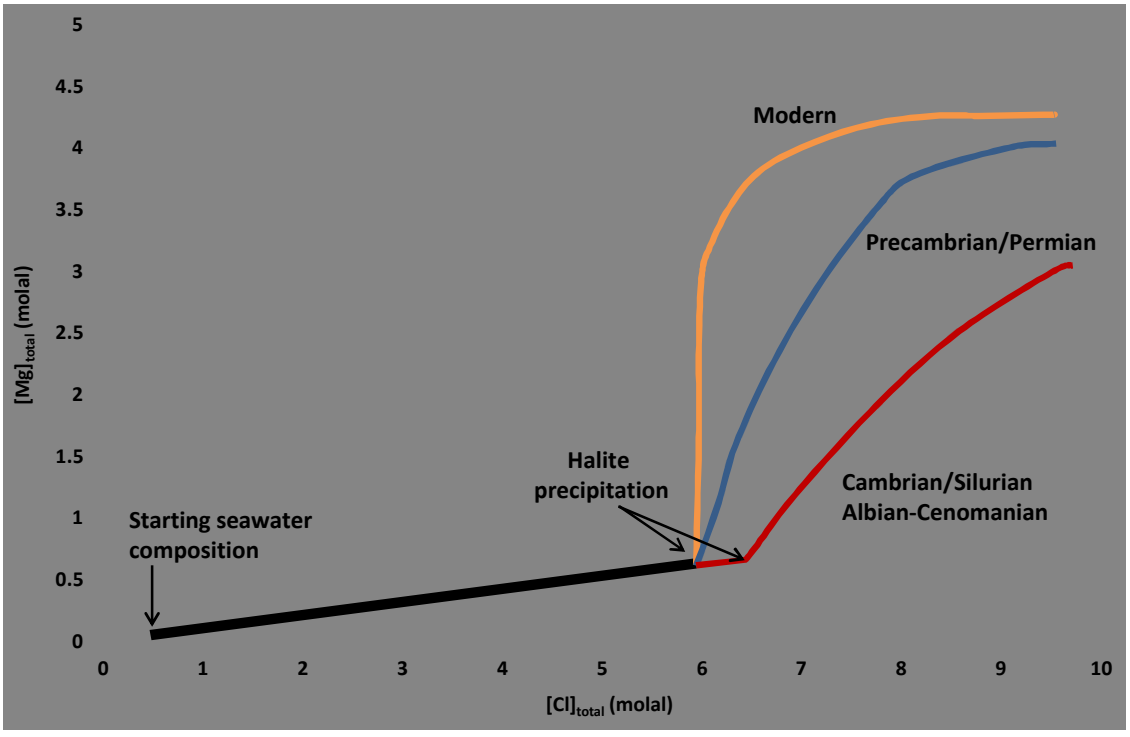

Figure 2b. Generalized depiction of Mg and Cl concentrations trends from Figure 2a with geologic time designations after Lowenstein et al. (2001).

Figure 3 show EQ3/6 reaction path modeling results of Mg and Cl concentrations for the evaporation of two seawater chemistries: Great Inagua Island (McCaffrey et al., 1987) and seawater benchmark composition (Nordstrom, 1979). The two evaporation trends are compared to the Great Inagua Island seawater evaporation data and the modern seawater data and trend given by Lowenstein et al. (2001). Notice the good agreement between data and computed trends for modern seawater compositions. The small differences are attributed to minor differences in the major ion composition of the starting seawater compositions. This result illustrates the susceptibility to relatively small differences in brine chemistry when influencing the resulting evaporation path beyond the halite precipitation or chemical divide at a Cl concentration of ~6.1 molal. An important assumption in these set of evaporations runs is the suppression of all salt solids except halite so the change trend as a result of the precipitation of this phase is captured. This is necessary in order to closely represent the modern seawater evaporation trend. The effect of including sylvite in reaction path results in no significant consequence to the evaporation trend up to Cl concentrations of ~6.9 molal. Beyond this value, the trend diverges from the one for halite only towards increasing Mg concentration coinciding with the trend for the seawater benchmark composition of Nordstrom (1979).

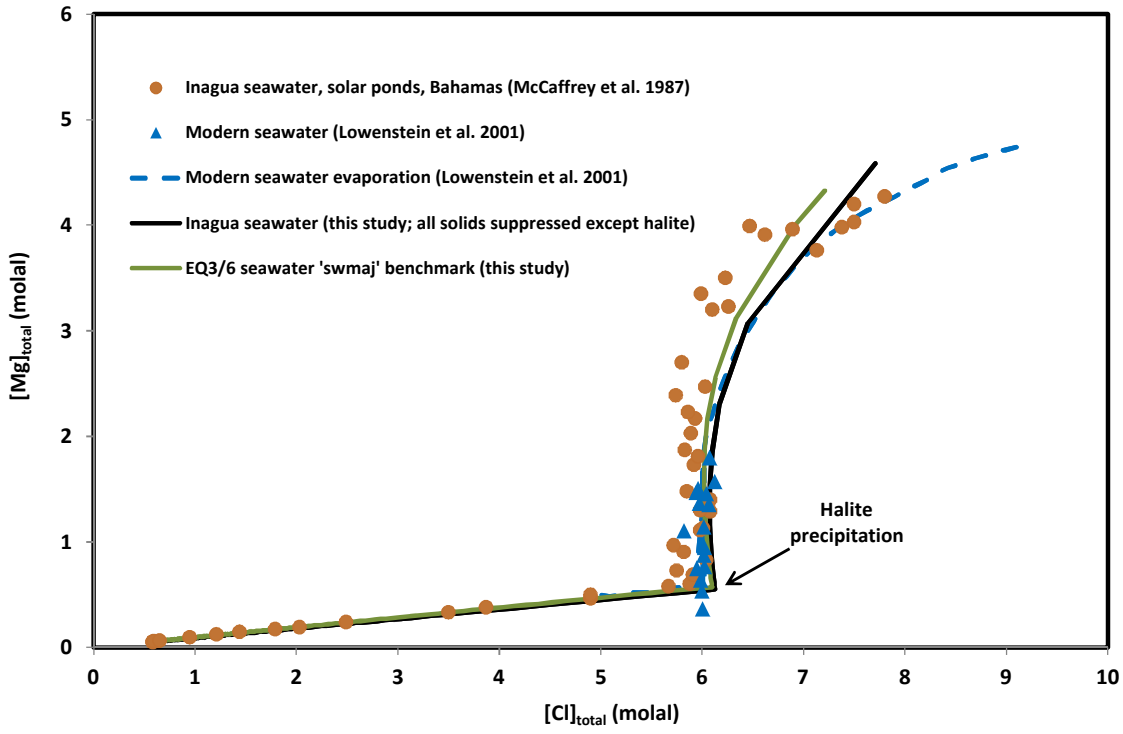

Figure 3. Mg and Cl concentrations and computed evaporation path for modern seawater (see text). Calculated curves with EQ3/6 are computed at a temperature of 31.25°C.

The other evaporation trends to be evaluated are the ones designate by geologic times such as Precambrian/Permian and Cambrian/Silurian/Albian-Cenomanian. This geologic time designations corresponds to those assigned by Lowenstein et al. (2001) to evaporation trends

given by fluid inclusion chemistry from salt samples having similar ages but from different locations.

Given that minor differences in the major ion composition can cause significant changes in the evaporation trends beyond halite precipitation or chemical divide, the reaction path calculations were tailored by adding NaCl and KCl salt components to the starting brine composition. Addition of other salt components such as Mg, Ca, or SO_4 was not investigated at this point and is a topic of a future study. Adding NaCl and KCl in stoichiometric amounts would have more evident effect on the evaporation path with respect to major salt phases that would precipitate earlier than Mg-Cl salts. The salt mineral assemblage considered in these reaction path calculations is composed of the following unsuppressed solid phases:

- Anhydrite ($CaSO_4$)
- Halite (NaCl)
- Sylvite (KCl)
- Carnallite ($KMgCl_3 \bullet 6H_2O$)
- Bischofite ($MgCl_2 \bullet 6H_2O$)
- Kieserite ($MgSO_4 \bullet H_2O$)
- Polyhalite ($K_2MgCa_2(SO_4)_4 \bullet 2H_2O$)

The choice for only considering this set of minerals is based mainly on two reasons:

- These phases are representative for the invariant salt mineral assemblage in the system Ca-K-Mg-Na-Cl-SO_4-H_2O as described in the studies by Kropp et al. (1988), Kropp and Holldorf (1988), and Krupp (2005). Evaporation of brines in this system will result in halite saturation (i.e., halite + salts + brine) where this phase exerts important controls on the resulting salt assemblage (Eugster et al., 1980; Krupp, 2005). Moreover, the Riedel mine brine compositions that are rich in Mg falls within the saturation boundaries of these minerals as described in Krupp (2005).
- Thermodynamic data at elevated temperatures exist for these phases allowing for the evaluation of salt solubilities at above-ambient conditions. Moreover, this set of salt minerals defines invariant point phase assemblages as a function of temperature, for example, the solubility of polyhalite which is discussed in a later section.

There are other phases whose composition fall into this system, for example: glaserite ($NaK_3(SO_4)_2$), glauberite ($Na_2Ca(SO_4)_2$), kainite ($KMgClSO_4 \bullet 3H_2O$), syngenite ($K_2Ca(SO_4)_2 \bullet H_2O$), görgeyite ($K_2Ca_5(SO_4)_6 \bullet H_2O$), picromerite ($K_2Mg(SO_4)_2 \bullet 6H_2O$), bloedite ($Na_2Mg(SO_4)_2 \bullet 4H_2O$), and langbeinite ($K_2Mg_2(SO_4)_3$). Some (if not most) of these minerals are in the YMP Pitzer database but don't have thermodynamic data at high temperatures; with the exception of glauberite and syngenite. The reaction path calculations indicate that these salts don't saturate persistently or as often throughout the evaporation calculation when saturated salts

from selected set dominated the equilibrium assemblage. The same applies to $MgSO_4$ salts where sulfate solubility is mainly controlled by anhydrite and kieserite. Carbonate-bearing phases are also excluded from this analysis given the much added complexity to the assessment of phase relations and salt solubility. However, these are also important given their influence on Ca solubility (e.g., calcite) and potentially Mg bearing carbonate minerals (magnesite) that occur in evaporite deposits.

The reaction path calculations were conducted by adding either NaCl (halite), KCl (sylvite), or both to the Inagua starting seawater composition. The purpose of adding these phases as titrant in the code run is to effectively add major salt components (NaCl and KCl) in stoichiometric amounts to a modern seawater composition. The amounts added are relatively small, on the order of 0.1 moles (halite) and 0.01 to 0.05 moles (sylvite). These reactant masses are exhausted early and prior to the attainment of saturation with respect to either of these two salts. As shown in Figure 4, the effect of adding NaCl only is to lower the Mg concentration beyond the halite precipitation point closely corresponding to the Precambrian/Permian trend. Addition of both NaCl and KCl (NaCl/KCl = 10) result in further lowering of Mg concentration and matching the Precambrian/Permian trend, including the Riedel mine Mg-Cl brine seeps studied by Krupp (2005). Addition of more KCl (NaCl/KCl = 5) produces even lower Mg concentrations closely corresponding to those of the Dead Sea rift fluid inclusion compostions of Pliocene age. The effect of adding more KCl (NaCl/KCl = 2) is to lower the Mg concentration to the point it matches the Cambrian/Silurian/Albian-Cenomanian evaporation trend up to a Cl concentration of ~7.4 molal. There is also reasonable agreement between the predicted Mg-Cl compositional trends and the fluid inclusion chemistry for the Pliocene Sedom formation in the Dead Sea Rift. However, scatter in the Dead Sea Rift data precludes from any definitive interpretation based on these comparisons and overall the fluid inclusions tend to have high K concentration. One notable aspect of the evaporation trend is the influence of sylvite saturation causing the trend to shift from the Cambrian/ Silurian/Albian-Cenomanian trend towards higher Mg concentrations with increasing evaporation extent. This behavior is also reflected on the behavior of K vs. Cl concentration in Figure 5 where the predicted trend is in good agreement with the data. This comparison with a much younger evaporite formation is a good test of the predictive capability of the evaporation model. An unusual result was obtained when the NaCl/KCl = 2 and sylvite formation was suppressed. The resulting curve is in very good agreement with the Cambrian/ Silurian/Albian-Cenomanian evaporation trend but sylvite is saturated at a Cl concentration above ~7.4 molal. This result is interesting given that it matches the Mg-Cl trend which is unique relative to others but the fact that sylvite needs to be suppressed calls for caution in its interpretation. More runs with different input constraints are needed to better assess evaporative trend behavior.

The general agreement between predicted evaporation chemistries in multiphase multicomponent salt systems constrained by representative mineral assemblages in natural evaporite deposits is a good indication of the usefulness of reaction path modeling to evaluate brine chemistry during progressive evaporation. Even when recent fluid inclusion chemical data have provided a wealth of information about highly concentrated brines in rock salt, there is still the necessity to expand

the wide range of fluid chemistries along with accurate characterization of co-existing salt phases to further develop predictive models. Moreover, major ion chemistry needs to be complemented by isotope studies and comprehensive characterization of salt phase paragenesis.

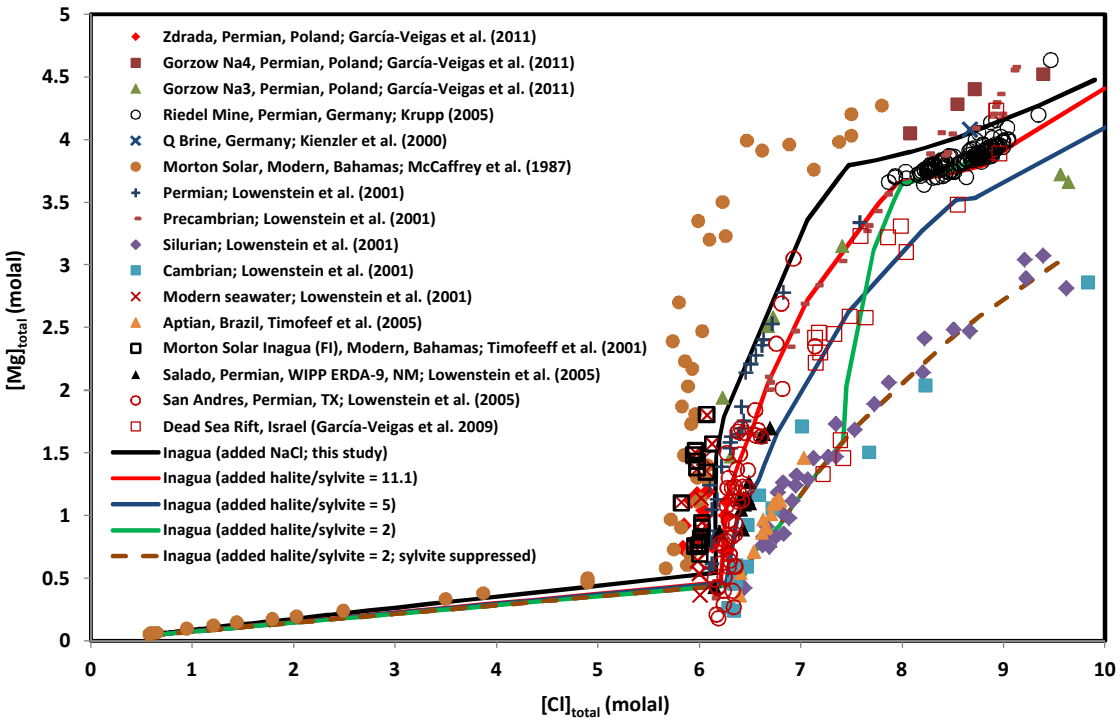

Figure 4. Comparison of Mg and Cl concentrations trends from fluid inclusion and brine chemistry with predicted evaporation calculations using EQ3/6. The Albian-Cenomanian data for Laos (Timofeeff et al., 2006) was omitted to add clarity.

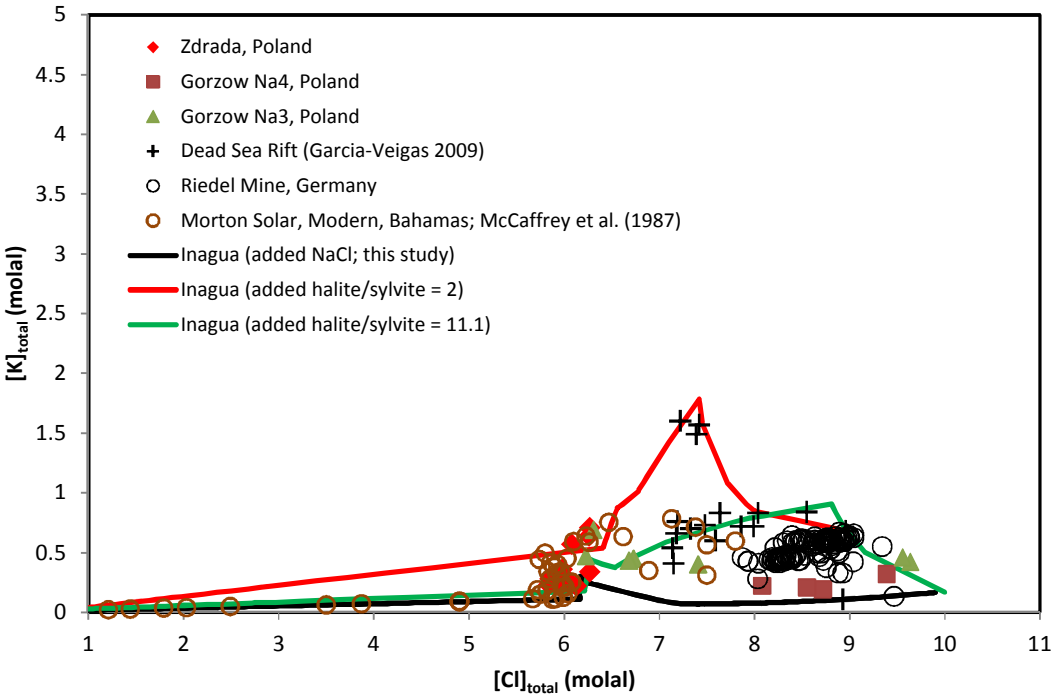

Figure 5. K and Cl concentrations in fluid inclusion from various locations. The data by Krupp (2005) corresponds to brine seeps from the Riedel mine, Germany.

1.4 Evaluation of Polyhalite Solubility and Evaporation Simulations at Elevated Temperatures

Polyhalite ($K_2MgCa_2(SO_4)_4 \bullet 2H_2O$) is a common accessory triple-salt mineral observed in evaporative rock salt deposits. This mineral and related salt phases has been studied by multicomponent phase equilibrium relations in the quinary/hexary system Ca-K-Mg-(Na)-Cl-SO_4-H_2O (Voigt, 2001; Wollmann et al., 2008). Some experimental studies have investigated the solubility of polyhalite (Bodaleva and Lepeshkov, 1956; Conley et al., 1938; D'Ans, 1933; Kropp et al., 1988; Kropp and Holldorf, 1988; Lepeshkov and Novikova, 1958; Perova, 1970) but few have been conducted at temperatures beyond 100°C. Risacher and Fritz (1984) studied the solubilities of evaporite minerals as a function of temperature (up to 300°C) using estimations of thermodynamic properties of equilibrium reactions between salt and the aqueous electrolyte phase. These thermodynamic estimations were based on the entropy contributions in the salt solubility reactions as a function of temperature. For hydrated (double or triple) salts, this approach estimates the entropy of these minerals as the sum of the entropies of its main salt components. For example, for the mineral polyhalite the breakdown of phase components is represented as $2K_2SO_4 \bullet MgSO_4 \bullet 2CaSO4 \bullet 2H_2O$. Although such approach has been used in the extrapolation of thermodynamic properties of solids, it can suffer from accuracy issues at temperatures above 100°C, particularly for hydrated phases. Nevertheless, such approach makes provisions for solubility estimates with often adequate levels of consistency with experimental studies.

Other studies have focused on the thermal stability of polyhalite to resolve the phase decomposition temperature which is relevant to disposal of heat generating waste in salt (Fischer et al., 1996; Wollmann et al., 2008). These studies concluded that polyhalite thermally decompose at peak temperatures in the neighborhood of 280°C, concomitantly with phase dehydration. The product of this thermal composition is anhydrite plus a triple salt where the latter undergoes further reaction to form two solid solutions (Fischer et al., 1996).

The solubility of polyhalite is determined by the complex equilibria in a multiphase multicomponent salt system where equilibrium solutions are highly concentrated in Mg and Cl. The complexity of such system is demonstrated by the wide scatter of retrieved solubility constants from experiments at various temperatures. This scatter is usually attributed to difficulties associated with kinetic hindrances in the attainment of phase equilibria, metastable persistence of salt phases at various temperatures, and in many cases lack of accurate salt phase characterization of the resulting mineral assemblage. These complications are exacerbated in experiments at temperatures close to ambient which require long equilibration times where data is often insufficient. The experimental studies of Kropp et al. (1988), and Kropp and Holldorf (1988) investigated the equilibrium relations of salt phases in the hexary system Ca-K-Mg-Na-Cl-SO_4-H_2O. These studies focused on the analysis of solution compositions determined by invariant points defined by the coexistence of salt mineral assemblage in this system. The solubility data by Kropp et al. (1988) was based on a large set of experiments that allowed for equilibration times of up to 50 days at temperatures close to ambient. Wollmann (2010) conducted a comprehensive analysis of polyhalite equilibria to estimate solubility constants by evaluating existing experimental data from a wide range of sources. The analysis of Wollmann (2010) results in the retrieval of solubility constants for polyhalite as a function of temperature on the basis of a large body of data but it also advances comparisons of stability relations with respect to other salt minerals. Such analysis is equivalent or at least conforms to a mapping of equilibrium solution compositions determined by invariant points of salt mineral assemblages. This work also provides a review of existing experimental data and its limitations for use in the retrieval of solubility constants for polyhalite.

The current solubility analysis of polyhalite at elevated temperatures focuses on the prediction of Mg concentrations in solution constrained by multiphase multicomponent equilibria in the system Ca-K-Mg-Na-Cl-SO_4-H_2O as a function of temperature. The main source of Mg^{+2} concentrations used to constrain the current solubility analysis is from the data tabulations of Kropp and Holldorf (1988). These authors provide an encompassing mapping of invariant point salt mineral assemblage and associated solution compositions up to temperatures of 110°C.

The two invariant point salt mineral assemblages chosen for this analysis based on the work of Kropp and Holldorf (1988) are:

- halite-sylvite-anhydrite-carnallite-polyhalite
- halite-sylvite-anhydrite-kieserite-carnallite-polyhalite

These salt assemblages were selected because high temperature thermodynamic data for these phases along with Pitzer parameter data for this multicomponent system is available. Moreover, this Mg-bearing mineral assemblage is common to bedded salt deposits and it is also related to the focus of this study on Mg-bearing brines at elevated temperatures. The invariant point mapping was also performed using the computer code EQ3/6 (Wolery and Jarek, 2003) along with the Pitzer thermodynamic database developed for the YMP (Jové Colón, 2005; Mariner, 2007). The sources of thermodynamic data and details on the database development are described in Mariner (2007) and Jové Colón (2005). This thermodynamic database covers a fairly extensive set of salt solids and Pitzer interaction parameters up to temperatures of 250°C for the relevant salt species. EQ3/6 code runs were conducted in reaction path mode to progressively concentrate an initially briny solution by removal of H_2O solvent mass. The extent of evaporation as a result of this reaction path code run is allowed to proceed until the desired invariant point salt mineral assemblage used to constrain the Mg concentration in solution is obtained. That is, the saturation state of the minerals defining the invariant point salt assemblage is continuously mapped with progressive H_2O mass removal from solution. This approach is identical to the one used for the generation evaporation path trends described in a previous section but with a different initial solution composition and mineral suppressions.

The logK value for polyhalite at 25°C (logK = -13.7441) in the YMP Pitzer database is from Harvie et al. (1984). Wollmann (2010) advanced a logK value for polyhalite at 25°C calculated from enthalpy of dissolution data at ~40°C but the one given by Harvie et al. (1984) is retained for used in this solubility calculations. This logK value is in good agreement with that given by Risacher and Fritz (1984) and that extrapolated to 25°C reported by Wollmann (2010). The logK values at temperatures above 25°C were retrieved by adjusting the logK – temperature grid until the Mg concentration closely matches the invariant point solution composition given by Kropp and Holldorf (1988), constrained by the halite-sylvite-anhydrite-carnallite-polyhalite salt assemblage. Figure 6 shows the results of EQ3/6 code predictions compared to the Mg concentration data of Kropp and Holldorf (1988) for the two invariant point salt mineral assemblages selected for this analysis. Kropp and Holldorf (1988) observed the presence of kieserite in the halite-sylvite-anhydrite-carnallite-polyhalite assemblage at a temperature of 89°C. The EQ3/6 code predicts saturation with respect to this phase before reaching this temperature. No phase saturation constraint with respect to inclusion of this phase was considered in the retrieval of polyhalite solubility constants at temperatures of 89°C and above. The reason for this modeling choice is that kieserite is predicted close to saturation at these temperatures and adding this phase in the mineral assemblage produces Mg concentration values that are hard to reconcile the experimental solubility data. Therefore, adjustment of logK values

for kieserite would have been needed in addition to polyhalite to further a closer match to the Mg concentration data. Such adjustment of the kieserite logK was not considered given that this could translate in a break in internal consistency with the existing Mg-bearing salt thermodynamic data used in the calculations and the uncertainty levels in Mg concentrations are not clearly defined by Kropp and Holldorf (1988). Still, adjustments to kieserite (in addition to polyhalite) logK values were explored and these do not translate in significant improvements to the data "fit" nor does it results in significant differences to the existing kieserite logK data. Given the relative insensitiveness of the kieserite logK, all polyhalite solubility data "fitting" at temperatures of 89°C and above was done excluding kieserite from the halite-sylvite-anhydrite-carnallite-polyhalite invariant assemblage. Even with this assumption, the resulting logK values for polyhalite at these temperatures are in good agreement with those given by Risacher and Fritz (1984) and Wollmann (2010) (see Figure 7). It should be noted that the spread in solubility constants determined from experimental data as depicted by the vertical lines in Figure 7 exemplifies the level of uncertainty in these values. Still, the retrieved solubility constants are in good agreement with the experimental data trends up to a temperature of 100°C. The logK value at 150°C is based on extrapolation of the experimental invariant point value of Kropp and Holldorf (1988) at 110°C. The lack of solubility data at temperatures between 100°C and 150°C renders this logK value as highly uncertain. The reason for extrapolating to 150°C is due to the rather coarse logK – temperature grid in EQ3/6 logK data blocks at temperatures above 100°C. Such lack of experimental data beyond 100°C indicates an important data gap for this salt phase in this system. The retrieved logK values are listed in Table 2. This analysis demonstrate the usefulness of the invariant point mapping in salt systems using the EQ3/6 code to evaluate salt mineral saturations as a function of temperature. Such analysis is key to the analysis of brine evaporation and the expected compositional trends that can be expected in disposal salt environments for heat generating waste.

Table 2. Retrieved logK values for the reaction polyhalite = Mg^{++} + 2 Ca^{++} + K^{+} + 4 SO_4^{-} + 2 H_2O (see text)

T(°C)	LogK (this study)
25	-13.7441
35	-14.0522
50	-14.725
60	-15.2
75	-15.8295
85	-16.1138
100	-16.7
110	-17.86
150	-24.5[(a)]

[(a)] Value extrapolated to fit invariant point compositional data at 110°C.

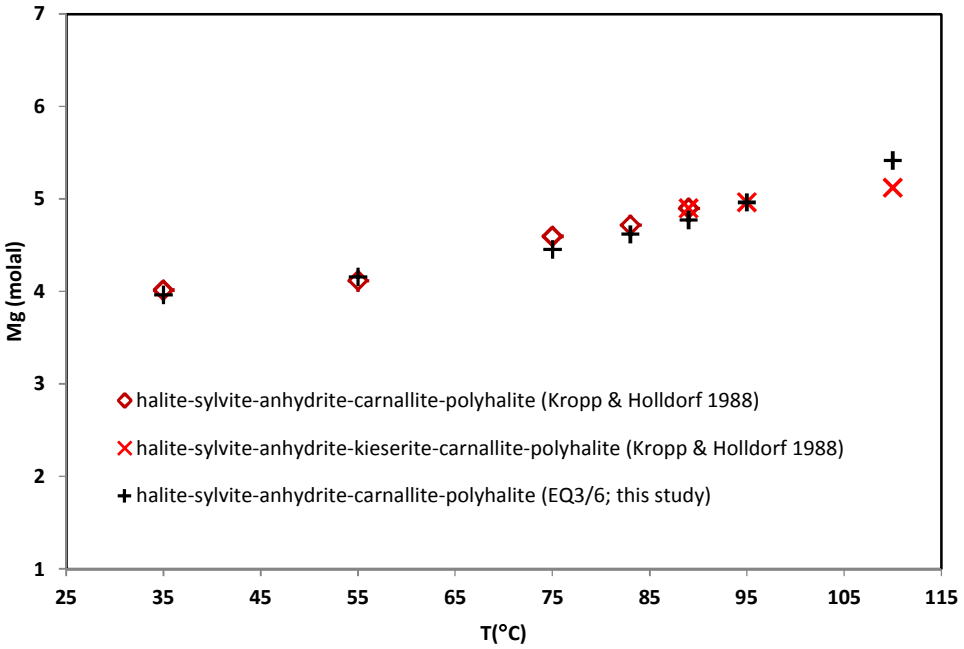

Figure 6. Mg concentrations in solution at saturation with respect invariant point salt assemblages in the system Ca-K-Mg-(Na)-Cl-SO_4-H_2O as a function of temperature. Notice the good agreement between EQ3/6 code predictions and the Mg concentrations given by Kropp and Holldorf (1988).

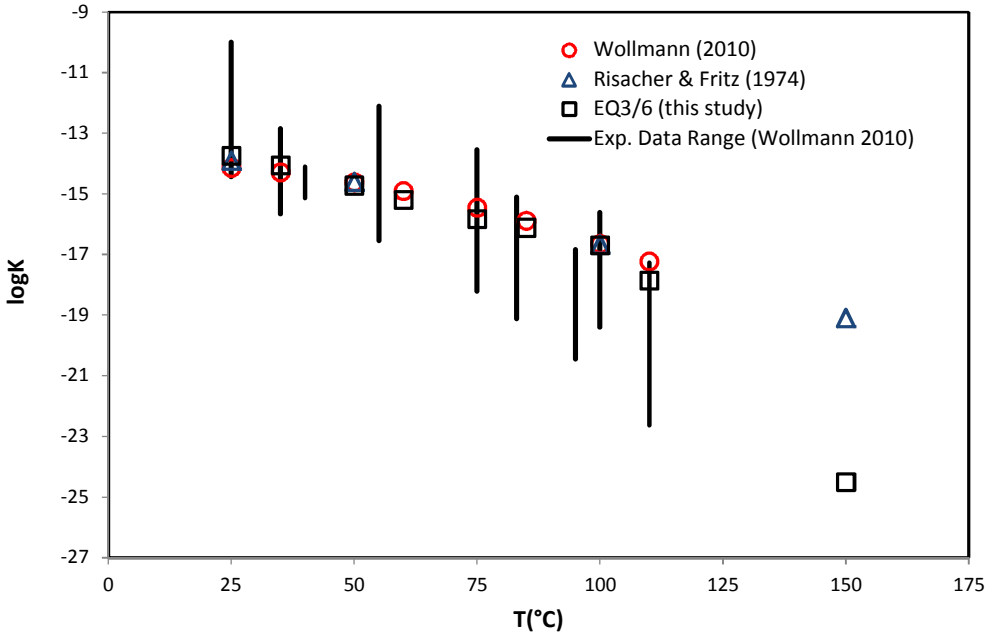

Figure 7. LogK values as a function of temperature for polyhalite solubility. Notice the good agreement between values obtained in the current analysis (EQ3/6) and those given elsewhere. Solid vertical lines indicate the logK range based on reported solubility data at each temperature. The logK value at 150°C should be regarded as highly uncertain since it was based on one invariant point composition datum at 110°C.

1.5 Evaluation of Brine Chemistry at Elevated Temperatures

1.5.1.1 Acid Gas Generation and acid brine Condensation

Acid brine generation was noticed in a heater test at WIPP (Molecke, 1986) where it may have cause failure of the heating device. The generation of acidic conditions as a result of high temperature brine interactions in salt repositories can be adverse to barrier performance of heat generating waste. Acid brine generation from brine-salt interactions can be a complex process that depends on pressure, temperature, and chemical conditions of the local environment. For example, acid brine can be produced from the condensations of acid gas species as a consequence of temperature differences when hot gas condenses in cooler regions where the relative humidity (RH) reaches 100%. Another way of generating acid brine is by evaporation of a solution that reaches high concentrations allowing for equilibria between an HCl-rich acid gas vapor phase, the hot electrolyte solution, and a salt solid (if the solubility limit is attained). However, acid gas generation requires the solution be in contact or in close proximity with a fairly concentrated electrolyte. This electrolyte must be chloride-rich in order to produce the necessary partial pressures of HCl(g) as delineated by the following reactions (C. R. Bryan 2012, personal communication):

$$HCl_{(aq)} \leftrightarrow HCl_{(g)} \qquad (1)$$

$$HCl_{(aq)} \leftrightarrow H^{+} + Cl^{-} \qquad (2)$$

The equilibria between HCl in the aqueous and gas phase given by reaction (1) can be represented as a mass action law expression:

$$K_{(1)} = \frac{f_{HCl_{(g)}}}{a_{HCl_{(aq)}}} \qquad (3)$$

where $K_{(1)}$ is the solubility constant for reaction (1), $f_{HCl_{(g)}}$ is the fugacity of HCl in the vapor phase, and $a_{HCl_{(aq)}}$ is the activity of HCl in the aqueous phase. The mass action law expression for reaction (2) is given by:

$$K_{(2)} = \frac{a_{H^{+}} a_{Cl^{-}}}{a_{HCl_{(aq)}}} \qquad (4)$$

where $K_{(4)}$ is the solubility constant for reaction (4) and $a_{H^{+}}$, $a_{Cl^{-}}$, and $a_{HCl_{(aq)}}$ are the activities of the H^{+}, Cl^{-}, and $HCl_{(aq)}$ in the aqueous phase, respectively. The above generalized reactions describe the equilibria between $HCl_{(g)}$ and the aqueous phase noting that evaluating pH requires the simultaneous treatment of these two reactions. The solubility constants in these expressions (reactions 3 and 4) are strongly dependent on temperature. Similarly, the activities of aqueous

species are also dependent on temperature and electrolyte concentration where the computation of activity coefficients requires the use of the Pitzer or other approaches in the treatment of highly concentrated electrolytes. This is needed to obtain accurate information of these properties at elevated temperatures to evaluate $f_{HCl_{(g)}}$ or the partial pressures of HCl at equilibrium with the brine phase. The equilibrium pH can also be affected by the presence of buffer species (e.g., carbonates, Mg chlorides) in the aqueous phase and a multicomponent multiphase analysis of chemical equilibria is necessary to accurately examine this process. For example, acidic mineral phases such as bischofite ($MgCl_2 \bullet 6H_2O$) and carnallite ($KMgCl_3 \bullet 6H_2O$) can be stable in acidic brines. Equilibrium with other phases in addition to reactions (1) and (2) makes this equilibrium problem even more complex. This is compounded by the fact that activity coefficients of the major ions in solution are a complex function of electrolyte concentration and temperature. Such analysis requires the use of sophisticated methods and approaches to compute chemical equilibria and related interactions as a function of temperature and electrolyte concentration. Therefore, the necessary inputs in the form of thermodynamic data applicable to the temperature and concentration range of interest needs to be acquired, analyzed, implemented, and tested to gain confidence in the predictive capability of this modeling approach.

1.5.1.2 Acid brine Generation in the Heater Test at the WIPP Site

Molecke (1986) observed a sharp drop in pH in brine condensate obtained from a heater test at Room B at the WIPP site. Molecke (1986) suggested that decomposition of Mg chloride salts led to the generation of $HCl_{(gas)}$ that then condensed as a low pH solution. The suggested reaction can be exemplified by the $MgCl_2 \bullet 4H_2O$ degradation to an anhydrous product:

$$MgCl_2 \bullet 4H_2O \rightarrow MgO + 2HCl_{(g)} + 3H_2O \qquad (5)$$

$MgCl_2 \bullet 4H_2O$ equilibrium solubility in an aqueous phase can also be expressed as:

$$MgCl_2 \bullet 4H_2O \leftrightarrow Mg^{++} + 2Cl^{-} + 4H_2O \qquad (6).$$

Therefore, phases like $MgCl_2 \bullet 6H_2O$ and associated hydrates needs to be characterized and evaluated given their influence on chloride concentration and potentially acidic brines. Krumhansl (1989) correlated the pH drop with extreme levels of evaporation which is consistent for the type of reactions (5) and (6) as suggested by Molecke (1986). The WIPP brines initially contain fairly high levels of Mg (35 ppm in the MIIT experiment) which would become concentrated at high levels of evaporation. However, the concentrations of some species in solution show different behavior when correlated with evaporation extent suggesting that equilibrium with respect solubility-controlling solids (i.e., salts) may have occurred.

Molecke (1986) also included an analysis from J.L. Krumhansl of the solid salt samples that formed at the failed heater. The collected salts (listed below) were present in various amounts:

- Halite (NaCl)
- Carnallite ($KMgCl_3 \bullet 6H_2O$)
- Bischofite ($MgCl_2 \bullet 6(H_2O)$
- Sylvite (KCl)
- Anhydrite ($CaSO_4$)
- Periclase (MgO)
- Hydromagnesite ($Mg_5(CO_3)_4(OH)_2 \bullet 4H_2O$)

The primary salts in the samples are halite and carnallite. As described in Molecke (1986), Krumhansl considered a set of decomposition reactions for Mg chloride solids to HCl and MgO. Krumhansl conducted an analysis to compute the condensate pH assuming equilibrium with $MgCl_2$ hydrate. The calculated trends of condensate pH versus temperature show a good correspondence with that measured at temperatures above 100°C. In that memo, Krumhansl also concluded that generation of acid brine could be described in terms of Mg-bearing salts since the non-negligible presence of other components such as Ca would have required higher temperatures to generate such a sharp drop in pH.

Although the analysis and arguments of Krumhansl were well constrained and thoughtful on the basis of solution-mineral-equilibria, it still has gaps and it is based on assumptions that need further analysis. The complexity of acid brine generation requires the use of state-of-the-art thermodynamic tools and methods along with the relevant thermodynamic data to calculate solubilities and activities of aqueous species at elevated temperatures in multiphase multicomponent system. The process that needs to be addressed in this task is the condition at which RH is at or exceeds the deliquescence relative humidity (DRH) of salt. More important, the equilibria in the Mg-Cl-H_2O salt system needs to assessed on the basis of temperature and stability relations between various $MgCl_2$ hydrates. Therefore, thermodynamic analysis of this salt system needs to be developed for the description of acid brine formation from heat generating waste.

1.5.1.3 Modeling Approaches and Required Thermodynamic Data

To address the abovementioned processes using thermodynamic principles of chemical equilibria, the computer code EQ3/6 (Wolery and Jarek, 2003) and YMP database development (Jové Colón, 2005; Mariner, 2007) will be used to assess the solubility relationships and pH as a function of temperature. Section 1.4 provides a description on how the code and database can be used in this type of calculation. The current thermodynamic databases have an internally-consistent data set for $MgCl_2$-HCl-H_2O salt system including Pitzer parameter data. Details on the development of these data are given in Jové Colón (2005) and Mariner (2007). The thermodynamic data for $MgCl_2$-H_2O solids and Pitzer parameters for this system are from Pabalan and Pitzer (1987). Pitzer parameter for HCl at elevated temperatures and pressures were obtained from Holmes et al. (1987). Pitzer parameters from other major ion components (Na, K,

Cl, SO4--) are from Greenberg and Moller (1989). The retrieval of all these thermodynamic parameters within the YMP Pitzer thermodynamic database is documented in Jové Colón (2005) and Mariner (2007).

The evaluation was focused on the solubility as a function of temperature for the following $MgCl_2$ phases:

- Bischofite ($MgCl_2 \bullet 6(H_2O)$)
- $MgCl_2 \bullet 4(H_2O)$
- $MgCl_2 \bullet 2(H_2O)$

The solubility and pH mapping as a function of temperature of these Mg chloride salts was done by EQ3/6 reaction path modeling. The code runs were set to attain saturation by adding $MgCl_2$ (chloromagnesite) to an initial solution close to bischofite saturation ([Mg] = 5.36 molal; [Cl] = 10.9 molal) at 25°C. The addition of $MgCl_2$ effectively increases the Mg and Cl solution concentration in stoichiometric amounts until attaining phase saturation at a given temperature.

1.5.1.4 Results and Discussion

The results of this analysis are depicted in Figure 8 where a plot of solubility (left y-axis) and computed pH (internal scale or Pitzer; right y-axis) are given as a function of temperature. The saturation molalities for each of the $MgCl_2$ hydrate phases maps are consistent with those given by Pabalan and Pitzer (1987) up to a temperature of 200°C. The code predicts the solubility and extent of bischofite stability up to a temperature of ~112°C which is consistent with the work of Pabalan and Pizer (1987). The transition temperature from $MgCl_2 \bullet 4(H_2O)$ to $MgCl_2 \bullet 2(H_2O)$ is predicted at ~174°C which is in agreement with the ~177°C value given by Pabalan and Pitzer (1987). Other studies such as those of Christov (2005, 2009) and Balarew et al. (2001) have evaluated solubility relation and thermodynamic data for the Mg-Cl-H_2O system up to 100°C and high concentrations. Christov (2009) utilizes solubility and parameter data comparable to that from the work of Pabalan and Pizer (1987) but with the addition HCl Pitzer parameters to the model.

The saturation molalities (equivalent to total Mg molal concentration) for bischofite up to 100°C reported by Christov (2009) are compared with the results obtained in this study as shown in Figure 9. Overall, the comparison shows very good agreement between both bischofite solubility calculations but minor discrepancies exists at low temperatures. The reason for these discrepancies is probably due to relatively minor differences in logK values of the salt solubility reactions and Pitzer parameter data. Such minor discrepancies could arise from preferential weighing in the fitting of solubility data, particularly within a wide temperature range such as this case. Also, the choice of binary and ternary Pitzer parameters as a function of temperature and the parameterization approach itself can weigh into these discrepancies although their influence appears to be relatively minor. Christov (2009) describes the differences between Pitzer parameters for the Mg-Cl_2-H_2O from Pabalan and Pitzer (1987) and those in his study to be relatively minor. However, the study by Pabalan and Pitzer (1987) doesn't explicitly considers Pitzer interaction parameters for HCl whereas Christov (2009) and the current study

does take these into account. Consideration of HCl Pitzer parameters is important in calculations that involve high concentrations of HCl in the electrolyte phase such as those assessed by Christov (2009) for the solubility of Hydrogen-Carnallite ($HCl \bullet MgCl_2 \bullet 7H_2O$) and bischofite. It should be noted that Christov (2009) focused on evaluating both $MgCl_2 + H_2O$ and $HCl + MgCl_2 + H_2O$ system. Therefore, the thermodynamic analysis in that study centers on vapor-liquid-solid equilibria under extremely acidic conditions.

In the current study, the computed pH is consistent with the Pitzer parameters in the thermodynamic database, therefore referred as the internal scale and this is discussed by Wolery and Jarek (2003). The pH trend shows a continuous decrease from pH~4.2 at 25°C up to pH~3.1 at the transition temperature of ~112°C. Above this temperature, the pH increases up to pH~4.8 at 200°C. The pH range between 3 and 4 is in good agreement with the reported pH of brines sampled exposed to temperatures of ~90°C in field experiments from the Materials Interface Interactions Test at WIPP (Krumhansl, 1989). It should be noted that pH measurements in this test were made in cool samples and and corrections were needed for extrapolations at elevated temperatures. Moreover, Krumhansl (1989) describes the complications encountered in the interpretations of these pH measurements which the author attributed to brine evaporation. In this case, the suggested mechanism for the general acidic character of these brines is ascribed to solution evaporation that generates HCl gas. This mechanism can be conducive to generation of low pH but as shown in Figure 8, equilibria in the $MgCl_2$-H_2O can produce very concentrated brines with high levels of chloride that could also induce generation of HCl(g) gas pressures. The mineral bischofite can be stable under extreme low pH conditions where its solubility decreases with increasing HCl concentration as described by Christov (2009). The current study explored reaction path calculations of bischofite solubility as a function of HCl concentration at 25°C producing results that are in good agreement with those presented by Christov (2009). The extremely acidic conditions discussed in that study may be too extreme to be expected from the brine chemistries in a salt repository. Still, the anticipated behavior with increasing temperature in the progressive evaporation of brine is that of increasing chloride concentrations therefore resulting in decreasing pH. However, the minimum pH attained under such conditions will depend on the brine chemistry and salt mineral assemblage in equilibrium with these solutions. This is a topic that deserves further investigation.

Another important aspect of these solubility calculations is the assessment of deliquescence relative humidity (DRH) which is related to the computation of water activity of the salt-liquid-vapor phase equilibria. The a_{H2O} in this case can be defined as the DRH/100. The resulting computations of water activity (a_{H2O}) or DRH/100 are shown in the right y-axis of Figure 9 and are compared to the values given by the model of Christov (2009). The computed a_{H2O} from the current model are in good agreement with the values of Christov (2009) up to a temperature of 100°C. Again, the minor discrepancies are due to differences in thermodynamic and Pitzer parameter data. Still, such close correspondence in a_{H2O} as a function of temperature is an excellent validation test between two different models. The importance of a_{H2O} is related to the local DRH conditions needed for the stability of the salt solid in equilibrium with brine and the

vapor phase. The a_{H2O} values are on the order of 0.3 and below. Such low a_{H2O} values suggest that brine can stabilize in equilibrium with the bischofite solid under fairly dry conditions.

The results of this work demonstrate that current geochemical code capabilities and input database parameters can be used to evaluate salt mineral solubility relationships in multicomponent multiphase systems as a function of temperature. However, there are gaps in solubility and/or thermodynamic data parameters needed to better constrain brine-salt interactions at elevated temperatures.

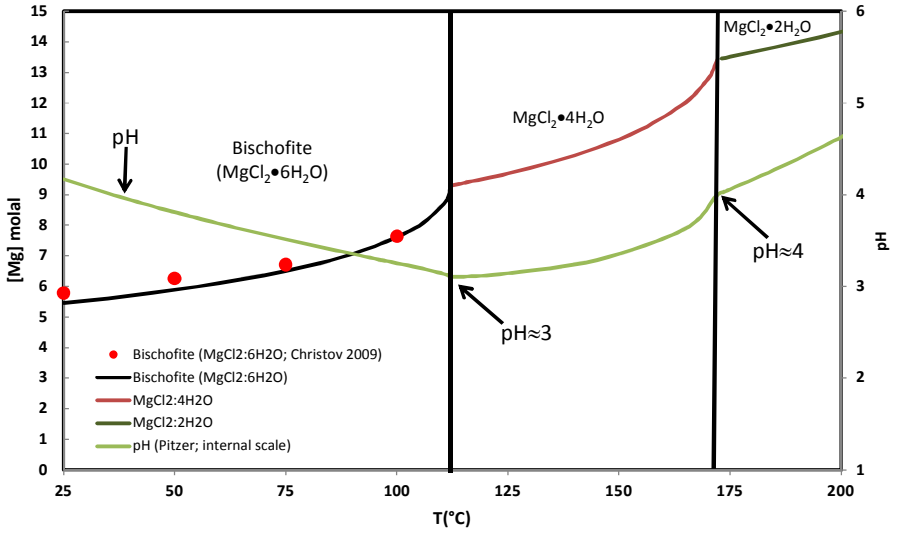

Figure 8. Predicted saturation molalities expressed in Mg concentration of $MgCl_2$ hydrated salts (left y-axis) and equilibrium pH (right y-axis) as a function of temperature. Note the good agreement with the calculated values of Christov (2009) up to 100°C.

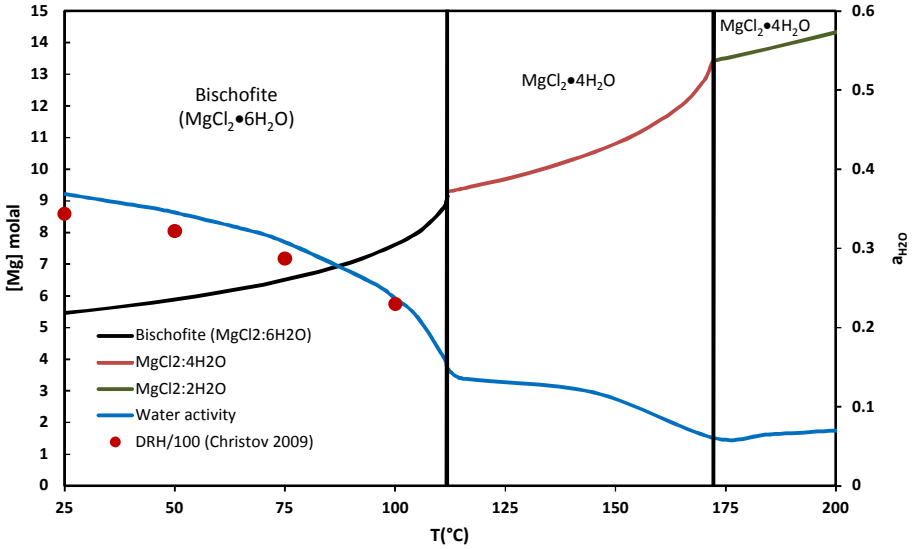

Figure 9. Predicted saturation molalities expressed in Mg concentration of $MgCl_2$ hydrated salts (left y-axis) and equilibrium activity of water (right y-axis) as a function of temperature. Note the good agreement with the calculated values of Christov (2009) up to 100°C. This author expresses a_{H2O} equal to DRH/100.

2. References

Ayora, C., Garcia-Veigas, J., and Pueyo, J. J., 1994, The Chemical and Hydrological Evolution of an Ancient Potash-Forming Evaporite Basin as Constrained by Mineral Sequence, Fluid Inclusion Composition, and Numerical-Simulation: Geochimica Et Cosmochimica Acta, v. 58, no. 16, p. 3379-3394.

Balarew, C., Tepavitcharova, S., Rabadjieva, D., and Voigt, W., 2001, Solubility and crystallization in the system $MgCl_2$-$MgSO_4$-H_2O at 50 and 75°C: Journal of Solution Chemistry, v. 30, p. 815–823.

Bein, A., Hovorka, S. D., Fisher, R. S., and Roedder, E., 1991, Fluid Inclusions in Bedded Permian Halite, Palo Duro Basin, Texas - Evidence for Modification of Seawater in Evaporite Brine-Pools and Subsequent Early Diagenesis: Journal of Sedimentary Petrology, v. 61, no. 1, p. 1-14.

Bodaleva, N. V., and Lepeshkov, I. N., 1956, A Study of Solubility in the System K_2SO_4-$MgSO_4$-$CaSO_4$-H_2O at 55-Degrees C: Journal of Inorganic Chemistry-USSR, v. 1, no. 5, p. 123-136.

Braitsch, O., 1971, Salt deposits; their origin and composition, Berlin, New York, Springer-Verlag, Minerals, rocks and inorganic materials, v. 4, xiv, 297 p.:

Cendon, D. I., Ayora, C., Pueyo, J. J., Taberner, C., and Blanc-Valleron, M. M., 2008, The chemical and hydrological evolution of the Mulhouse potash basin (France): Are "marine" ancient evaporites always representative of synchronous seawater chemistry?: Chemical Geology, v. 252, no. 3-4, p. 109-124.

Cendon, D. I., Pueyo, J. J., Ayora, C., Taberner, C., and Peryt, T., 2006, Sulfate starved subbasins: Implications for Permian seawater composition: Geochimica Et Cosmochimica Acta, v. 70, no. 18, p. A91-A91.

Christov, C., 2005, Thermodynamics of formation of double salts and mixed crystals from aqueous solutions: Journal of Chemical Thermodynamics, v. 37, p. 1036–1060.

-, 2009, Chemical Equilibrium Model of Solution Behavior and Bishofite ($MgCl_2$•$6H_2O$(cr)) and Hydrogen-Carnallite (HCl•$MgCl_2$•$7H_2O$(cr)) Solubility in the $MgCl_2$ + H_2O and HCl-$MgCl_2$ + H_2O Systems to High Acid Concentration at (0 to 100) °C: Journal of Chemical & Engineering Data, v. 54, p. 2599–2608.

Conley, J. E., Gabriel, A., and Partridge, E. P., 1938, Equilibria in the system potassium sulfate-magnesium sulfate-calcium sulfate-water at 100°C: Journal of Physical Chemistry, v. 42, no. 5, p. 587-616.

D'Ans, J., 1933, Die Lösungsgleichgewichte der Systeme der Salze ozeanischer Salzablagerungen, Berlin, Verlagsgesellschaft für Ackerbau m.b.H.

Demicco, R. V., Lowenstein, T. K., Hardie, L. A., and Spencer, R. J., 2005, Model of seawater composition for the Phanerozoic: Geology, v. 33, no. 11, p. 877-880.

Eugster, H. P., Harvie, C. E., and Weare, J. H., 1980, Mineral Equilibria in a 6-Component Seawater System, Na-K-Mg-Ca-So4-Cl-H2o, at 25-Degrees-C: Geochimica Et Cosmochimica Acta, v. 44, no. 9, p. 1335-1347.

Fischer, S., Voigt, W., and Kohnke, K., 1996, The thermal decomposition of polyhalite K_2SO_4•$MgSO_4$•$2CaSO_4$•$2H_2O$: Crystal Research and Technology, v. 31, no. 1, p. 87-92.

Garcia-Veigas, J., Cendon, D. I., Pueyo, J. J., and Peryt, T. M., 2011, Zechstein saline brines in Poland, evidence of overturned anoxic ocean during the Late Permian mass extinction event: Chemical Geology, v. 290, no. 3-4, p. 189-201.

Garcia-Veigas, J., Pueyo, J. J., and Ayora, C., 1992, Fluid Inclusion Analysis and Evaporite Modeling: Water-Rock Interaction, Vols 1 and 2, p. 649-653.

Gens, A., Guimaraes, L. D., Olivella, S., and Sanchez, M., 2010, Modelling thermo-hydro-mechano-chemical interactions for nuclear waste disposal: Journal of Rock Mechanics and Geotechnical Engineering, v. 2, no. 2, p. 97–102.

Gens, A., Sanchez, M., Guimaraes, L. D., Alonso, E. E., Lloret, A., Olivella, S., Villar, M. V., and Huertas, F., 2009, A full-scale in situ heating test for high-level nuclear waste disposal: observations, analysis and interpretation: Geotechnique, v. 59, no. 4, p. 377-399.

Greenberg, J. P., and Moller, N., 1989, The prediction of mineral solubilities in natural waters: A chemical equilibrium model for the Na-K-Ca-Cl-SO_4-H_2O system to high concentration from 0 to 250°C: Geochimica et Cosmochimica Acta, v. 53, p. 2503–2518.

Guimaraes, L. D., Gens, A., and Olivella, S., 2007, Coupled thermo-hydro-mechanical and chemical analysis of expansive clay subjected to heating and hydration: Transport in Porous Media, v. 66, no. 3, p. 341-372.

Guimaraes, L. D., Gens, A., Sanchez, M., and Olivella, S., 2006, THM and reactive transport analysis of expansive clay barrier in radioactive waste isolation: Communications in Numerical Methods in Engineering, v. 22, no. 8, p. 849-859.

-, 2010, Coupled THMC modeling of unsaturated swelling clays: Constitutive formulation and boundary value problems: Unsaturated Soils: Theoretical and Numerical Advances in Unsaturated Soil Mechanics, p. 515-529.

Hardie, L. A., 1968, Origin of Recent Non-Marine Evaporite Deposit of Saline Valley Inyo County California: Geochimica et Cosmochimica Acta, v. 32, no. 12, p. 1279-&.

-, 1982, Reconstruction of Brine Compositions of Ancient Evaporites from Their Mineralogy - Application to Chemistry of Ancient Sea-Water: Aapg Bulletin, v. 66, no. 5, p. 577-577.

-, 1984, Evaporites - Marine or Non-Marine: American Journal of Science, v. 284, no. 3, p. 193-240.

-, 1991, On the Significance of Evaporites: Annual Review of Earth and Planetary Sciences, v. 19, p. 131-168.

-, 1996, Secular variation in seawater chemistry: An explanation for the coupled secular variation in the mineralogies of marine limestones and potash evaporites over the past 600 my: Geology, v. 24, no. 3, p. 279-283.

-, 1998, On the secular variations in the composition of Phanerozoic marine potash evaporites: Comment: Geology, v. 26, no. 1, p. 91-92.

Hardie, L. A., and Lowenstein, T. K., 2004, Did the Mediterranean sea dry out during the Miocene? A reassessment of the evaporite evidence from DSDP legs 13 and 42A cores: Journal of Sedimentary Research, v. 74, no. 4, p. 453-461.

Harvie, C. E., Moller, N., and Weare, J. H., 1984, The Prediction of Mineral Solubilities in Natural Waters: The Na-K-Mg-Ca-H-Cl-SO_4-OH-HCO_3-CO_3-CO_2-H_2O System to High Ionic Strengths at 25°C: Geochimica et Cosmochimica Acta, v. 48, no. 4, p. 723-751.

Helgeson, H. C., 1968, Evaluation of Irreversible Reactions in Geochemical Processes Involving Minerals and Aqueous Solutions .I. Thermodynamic Relations: Geochimica et Cosmochimica Acta, v. 32, no. 8, p. 853-877.

-, 1970, A chemical and thermodynamic model of ore deposition in hydrothermal systems, Mineralogical Society of America Special Paper 3: Washington, D.C., Mineralogical Society of America, p. 155–186.

Holmes, H. F., Busey, R. H., Simonson, J. M., Mesmer, R. E., Archer, D. G., and Wood, R. H., 1987, The Enthalpy of Dilution of HCl(aq) to 648 K and 40 Mpa - Thermodynamic Properties: Journal of Chemical Thermodynamics, v. 19, no. 8, p. 863-890.

Horita, J., Zimmermann, H., and Holland, H. D., 2002, Chemical evolution of seawater during the Phanerozoic: Implications from the record of marine evaporites: Geochimica Et Cosmochimica Acta, v. 66, no. 21, p. 3733-3756.

Hsü, K. J., 1972, Origin of Saline Giants - Critical Review after Discovery of Mediterranean Evaporite: Earth-Science Reviews, v. 8, no. 4, p. 371-396.

Jové Colón, C. F., 2005, Pitzer Database Expansion to Include Actinides and Transition Metal Species (data0.ypf.R1) (ANL-WIS-GS-000001 REV 00): U.S. Department of Energy, Office of Civilian Radioactive Waste Management, Office of Repository Development, Las Vegas, Nevada, USA, Bechtel SAIC Company, p. 140.

Kovalevich, V. M., Peryt, T. M., and Petrichenko, O. I., 1998, Secular variation in seawater chemistry during the phanerozoic as indicated by brine inclusions in halite: Journal of Geology, v. 106, no. 6, p. 695-712.

Kovalevych, V. M., Peryt, T. M., Carmona, V., Sydor, D. V., Vovnyuk, S. V., and Halas, S., 2002, Evolution of Permian seawater: evidence from fluid inclusions in halite: Neues Jahrbuch Fur Mineralogie-Abhandlungen, v. 178, no. 1, p. 27-62.

Kropp, E., Beate, R., Grosch, C., Kranz, M., and Holldorf, H., 1988, Untersuchungen zu den Isothermen des hexären Systems Na^+, K^+, Mg^{2+}, Ca^{2+},/Cl^-, SO_4^{2-}//H_2O bei 35°C, 55°C, 75°C, 95°C und 110°C im Bereich der Sättigung von NaCl, KCl ($KCl•MgCl_2•6H_2O$) und einem Ca^{2+}-haltigen Bodenkörper: Freiberger Forschungshefte, v. A-764, p. 42–66.

Kropp, E., and Holldorf, H., 1988, Entwurf einer Polytherme für das hexäre System Na^+, K^+, Mg^{2+}, Ca^{2+}/C^{l-}, SO_4^{2-}//H_2O im Temperaturbereich zwischen 35°C und 110°C und bei Sättigung an NaCl, KCl ($KClxMgCl_2x6H_2O$) und einem Ca^{2+}-haltigem Bodenkörper: Freiberger Forschungshefte, v. A-764, p. 67-82.

Krumhansl, J. L., 1989, Waste Isolation Pilot Plant Brine Field pH Measurements:Technique and Interpretation (SAND88-335), *in* Laboratories, S. N., ed.: Albuquerque, New Mexico, p. 1-57.

Krupp, R. E., 2005, Formation and chemical evolution of magnesium chloride brines by evaporite dissolution processes - Implications for evaporite geochemistry: Geochimica Et Cosmochimica Acta, v. 69, no. 17, p. 4283-4299.

Lambert, S. J., 1992, Geochemistry of the Waste Isolation Pilot-Plant (WIPP) Site, Southeastern New-Mexico, USA: Applied Geochemistry, v. 7, no. 6, p. 513-531.

Lepeshkov, I. N., and Novikova, L. V., 1958, Fiziko-Khimicheskoe Izuchenie Sistemy K_2SO_4-$MgSO_4$-$CaSO_4$-H_2O Pri 35-Gradusakh: Zhurnal Neorganicheskoi Khimii, v. 3, no. 10, p. 2395-2407.

Lotze, F., 1957, Steinsalz und Kalisalze, Berlin-Nikolassee, Gebr. Borntraeger.

Lowenstein, T. K., and Hardie, L. A., 1985, Criteria for the Recognition of Salt-Pan Evaporites: Sedimentology, v. 32, no. 5, p. 627-644.

Lowenstein, T. K., Hardie, L. A., Timofeeff, M. N., and Demicco, R. V., 2003, Secular variation in seawater chemistry and the origin of calcium chloride basinal brines: Geology, v. 31, no. 10, p. 857-860.

Lowenstein, T. K., and Timofeeff, M. N., 2008, Secular variations in seawater chemistry as a control on the chemistry of basinal brines: test of the hypothesis: Geofluids, v. 8, no. 2, p. 77-92.

Lowenstein, T. K., Timofeeff, M. N., Brennan, S. T., Hardie, L. A., and Demicco, R. V., 2001, Oscillations in Phanerozoic seawater chemistry: Evidence from fluid inclusions: Science, v. 294, no. 5544, p. 1086-1088.

Lowenstein, T. K., Timofeeff, M. N., Kovalevych, V. M., and Horita, J., 2005, The major-ion composition of Permian seawater: Geochimica Et Cosmochimica Acta, v. 69, no. 7, p. 1701-1719.

Mariner, P. E., 2007, In-Drift Precipitates/Salts Model: Sandia National Laboratories.

McCaffrey, M. A., Lazar, B., and Holland, H. D., 1987, The Evaporation Path of Seawater and the Coprecipitation of Br- and K+ with Halite: Journal of Sedimentary Petrology, v. 57, no. 5, p. 928-937.

Molecke, M. A., 1983, A Comparison of Brines Relevant to Nuclear Waste Experimentation: Sandia National Laboratories, SAND83-0516, Albuquerque, NM, p. 64.

-, 1986, Measurement of Hydrochloric Acid Vapors in WIPP From In Situ Experiments -- SAFETY ASPECTS.

Nordstrom, D. K., 1979, A comparison of computerized chemical models for equilibrium calculations in aqueous systems, *in* Jenne, E. A., ed., Chemical Modeling in Aqueous Systems, Volume 93: Washington, D.C., American Chemical Society, p. 857-892.

Nutt, M., Voegele, M., Jove-Colon, C., Wang, Y., Howard, R., Blink, J., Liu, H.-H., Hardin, E., and Jenni, K., 2011, Used Fuel Disposition Campaign Disposal Research and Development Roadmap (Fuel Cycle Research and Development), Prepared for U.S. Department of Energy Used Fuel Disposition Campaign FCR&D-USED-2011-000065

Olivella, S., Castagna, S., Alonso, E. E., and Lloret, A., 2011, Porosity Variations in Saline Media Induced by Temperature Gradients: Experimental Evidences and Modelling: Transport in Porous Media, v. 90, no. 3, p. 763-777.

Pabalan, R. T., and Pitzer, K. S., 1987, Thermodynamics of Concentrated Electrolyte Mixtures and the Prediction of Mineral Solubilities to High-Temperatures for Mixtures in the System Na-K-Mg-Cl-SO_4-OH-H2O: Geochimica Et Cosmochimica Acta, v. 51, no. 9, p. 2429-2443.

Perova, A. P., 1970, Volume of Polyhalite Crystallization in K,Mg, Ca-Cl,SO_4-H_2O Quinary System at 25 and 55 Degrees C: Zhurnal Neorganicheskoi Khimii, v. 15, no. 6, p. 1648.

Risacher, F., and Fritz, B., 1984, Estimation des variations en fonction de la température des produits de solubilité des principaux sels des milieux évaporitiques: Sciences Géologiques, Bulletin, v. 37, no. 3, p. 229-237.

Roedder, E., Dangelo, W. M., Dorrzapf, A. F., and Aruscavage, P. J., 1987, Composition of Fluid Inclusions in Permian Salt Beds, Palo-Duro Basin, Texas, USA: Chemical Geology, v. 61, no. 1-4, p. 79-90.

Rutqvist, J., Backstrom, A., Chijimatsu, M., Feng, X. T., Pan, P. Z., Hudson, J., Jing, L., Kobayashi, A., Koyama, T., Lee, H. S., Huang, X. H., Rinne, M., and Shen, B. T., 2009a, A multiple-code simulation study of the long-term EDZ evolution of geological nuclear waste repositories: Environmental Geology, v. 57, no. 6, p. 1313-1324.

Rutqvist, J., Barr, D., Birkholzer, J. T., Chijimatsu, M., Kolditz, O., Liu, Q. S., Oda, Y., Wang, W. Q., and Zhang, C. Y., 2008, Results from an international simulation study on coupled thermal, hydrological, and mechanical processes near geological nuclear waste repositories: Nuclear Technology, v. 163, no. 1, p. 101-109.

Rutqvist, J., Barr, D., Birkholzer, J. T., Fujisaki, K., Kolditz, O., Liu, Q. S., Fujita, T., Wang, W. Q., and Zhang, C. Y., 2009b, A comparative simulation study of coupled THM processes and their effect on fractured rock permeability around nuclear waste repositories: Environmental Geology, v. 57, no. 6, p. 1347-1360.

Rutqvist, J., Ijiri, Y., and Yamamoto, H., 2011, Implementation of the Barcelona Basic Model into TOUGH-FLAC for simulations of the geomechanical behavior of unsaturated soils: Computers & Geosciences, v. 37, no. 6, p. 751-762.

Rutqvist, J., Stephansson, O., Noorishad, J., and Tsang, C. F., 1991, Modeling of Hydro-Thermo-Mechanical Effects in a Fracture Intersecting a Nuclear Waste Deposition Hole: High Level Radioactive Waste Management, Vols 1 and 2, p. 547-554.

Stein, C. L., and Krumhansl, J. L., 1988, A Model for the Evolution of Brines in Salt from the Lower Salado Formation, Southeastern New-Mexico: Geochimica Et Cosmochimica Acta, v. 52, no. 5, p. 1037-1046.

Timofeeff, M. N., Lowenstein, T. K., Brennan, S. T., Demicco, R. V., Zimmermann, H., Horita, J., and von Borstel, L. E., 2001, Evaluating seawater chemistry from fluid inclusions in halite: Examples from modern marine and nonmarine environments: Geochimica Et Cosmochimica Acta, v. 65, no. 14, p. 2293-2300.

Timofeeff, M. N., Lowenstein, T. K., da Silva, M. A., and Harris, N. B., 2006, Secular variation in the major-ion chemistry of seawater: Evidence from fluid inclusions in Cretaceous halites: Geochimica Et Cosmochimica Acta, v. 70, no. 8, p. 1977-1994.

Voigt, W., 2001, Solubility equilibria in multicomponent oceanic salt systems from t=0 to 200 degrees C. Model parameterization and databases: Pure and Applied Chemistry, v. 73, no. 5, p. 831-844.

Wolery, T. J., and Jarek, R. L., 2003, EQ3/6, Version 8.0: Software User's Manual: Sandia National Laboratories.

Wollmann, G., 2010, Crystallization Fields of Polyhalite and its Heavy Metal Analogues, Ph.D. Thesis, Der Fakultät für Chemie und Physik, Technischen Universität Bergakademie Freiberg, p. 209.

Wollmann, G., Freyer, D., and Voigt, W., 2008, Polyhalite and its analogous triple salts: Monatshefte Fur Chemie, v. 139, no. 7, p. 739-745.

Zharkov, M. A., and I□A□nshin, A. L., 1981, History of Paleozoic salt accumulation, Berlin; New York, Springer-Verlag.

First Principles Modeling of Complex Salts: Assessment of Thermal Properties

(Part II)

1. First Principles Modeling of Complex Salts

1.1 Background

The proposed and expected waste package emplacement scenarios for a salt repository include high capacity "hot" canisters with a surface temperature limit of 200°C. Therefore, the thermal decomposition of complex salts such as bischofite ($MgCl_2 \bullet 6H_2O$) or carnallite ($KMgCl_3 \bullet 6H_2O$), commonly found in halite salts, can provide a significant amount of water molecules needed to sustain the corrosion reactions after waste package emplacement. Other hydrous minerals such as polyhalite ($K_2MgCa_2(SO_4)_4 \bullet 2H_2O$) could also be a source of water for corrosion upon thermal decomposition, however this would require temperatures above 235°C.

For example, bischofite which is stable at 25°C will thermally decompose according to the successive reactions (Sugimoto, Dinnebier, and Hanson, 2007):

$$MgCl_2 \bullet 6H_2O \rightarrow MgCl_2 \bullet 4H_2O + 2H_2O \qquad (1)$$

$$MgCl_2 \bullet 4H_2O \rightarrow MgCl_2 \bullet 2H_2O + 2H_2O \qquad (2)$$

$$MgCl_2 \bullet 2H_2O \rightarrow MgCl_2 \bullet H_2O + H_2O \qquad (3)$$

$$MgCl_2 \bullet H_2O + H_2O \rightarrow Mg(OH)Cl \cdot nH_2O + HCl + (1\text{-}n)\ H_2O\ (0 \leq n \leq 0.3) \quad \text{at } 193\ °C \qquad (4)$$

As can be seen from reaction (4), temperatures above ca. 193°C or above will lead to the production of hydrochloric acid gas which will be highly detrimental to the integrity of the waste package. As a matter of fact, several cases of heater failures in Mg-containing salts were reported during the WIPP materials interface interaction tests and attributed to corrosion by hydrochloric acid vapors at high temperature (Molecke, 1986a; Molecke, 1986b). Although small amounts of HCl vapor were believed to be generated, it was suggested that the apparently high concentration of acid found in the brine migration-condensate liquid was caused by the significant concentrating effect of condensing the water and HCl vapors to a liquid (Molecke, 1986b).

In a similar way to bischofite, carnallite is expected to progressively dehydrate and decompose between 166 and 186 °C under quasi-isothermal and quasi-isobaric conditions (Emons, et al., 1989). Small amounts of anhydrite ($CaSO_4$) and other hydrated magnesium carbonates might also form due to the presence of trace amounts of sulfate and carbonate in solution.

Gaining understanding of the structural and electronic properties underlying the thermally-driven behavior (e.g., phases transformation, decomposition,…) of individual, defect-free complex salts is a crucial first step to decipher and predict the properties of other salt systems with increasing complexity. In this study, we report density functional theory (DFT) calculations of the structures and electronic properties of bischofite ($MgCl_2 \bullet 6H_2O$), dehydrated bischofite ($MgCl_2 \bullet 4H_2O$, $MgCl_2 \bullet 2H_2O$ and $MgCl_2 \bullet H_2O$), anhydrite ($CaSO_4$), polyhalite

($K_2Ca_2Mg(SO_4)_4 \bullet 2(H_2O)$) and carnallite ($KMgCl_3 \bullet 6(H_2O)$) performed within the generalized gradient approximation (GGA). The total and partial densities of states (DOS) were calculated and analyzed in order to assess the electronic properties and relative stability of these complex salts. Finally, using the structures optimized using DFT, thermal properties at constant volume and at constant pressure have been computed for $MgCl_2 \bullet 6H_2O$, $MgCl_2 \bullet 4H_2O$, $MgCl_2 \bullet 2H_2O$, $MgCl_2 \bullet H_2O$, $CaSO_4$, and $K_2Ca_2Mg(SO_4)_4 \bullet 2(H_2O)$ using density functional perturbation theory (DFPT).

1.2 First Principles Evaluation of Structures and Electronic Properties of Bischofite, Anhydrite, Polyhalite and Carnallite

We report density functional theory (DFT) calculations of the structures and electronic properties of bischofite ($MgCl_2 \bullet 6H_2O$), dehydrated bischofite ($MgCl_2 \bullet 4H_2O$, $MgCl_2 \bullet 2H_2O$ and $MgCl_2 \bullet H_2O$), anhydrite ($CaSO_4$), polyhalite ($K_2Ca_2Mg(SO_4)_4 \bullet 2(H_2O)$) and carnallite ($KMgCl_3 \bullet 6(H_2O)$) performed within the generalized gradient approximation (GGA). The total and partial densities of states (DOS) and energy band gaps separating the top of the valence band from the bottom of the conduction band were calculated and analyzed in order to assess the electronic properties and relative stability of these complex salts. Details of our computational approach are given in the next section, followed by a complete analysis and discussion of our results. This approach is an attempt to exploit first principles approaches to assess the thermal properties

1.2.1 Computational Methods

First-principles total energy calculations were performed using the spin-polarized density functional theory (DFT), as implemented in the Vienna *ab initio* simulation package (VASP) (Kresse and Furthmüller, 1996). The exchange-correlation energy was calculated using the generalized gradient approximation (GGA) (Perdew, et al., 1992), with the parameterization of Perdew, Burke, and Ernzerhof (PBE) (Perdew, Burke, and Ernzerhof, 1996).

The interaction between valence electrons and ionic cores was described by the projector augmented wave (PAW) method (Blöchl, 1994; Kresse and Joubert, 1999). The Ca($3p^6$,$4s^2$), Cl($3s^2$,$3p^5$), K($3p^6$,$4s^1$), Mg($2p^6$,$3s^2$), O($2s^2$,$2p^4$) and S($3s^2$,$3p^4$) electrons were treated explicitly as valence electrons in the Kohn-Sham (KS) equations and the remaining core electrons together with the nuclei were represented by PAW pseudopotentials. The KS equation was solved using the blocked Davidson (Davidson, 1983) iterative matrix diagonalization scheme. The plane-wave cutoff energy for the electronic wavefunctions was set to 500 eV, ensuring the total energy of the system to be converged to within 1 meV/atom.

All structures were optimized with periodic boundary conditions applied. Ionic relaxation was carried out using the quasi-Newton method and the Hellmann-Feynman forces acting on atoms were calculated with a convergence tolerance set to 0.01 eV/Å. Structural optimizations and properties calculations were carried out using the Monkhorst-Pack special *k*-point scheme (Monkhorst and Pack, 1976). The following *k*-point meshes were used for integrations in the Brillouin zone (BZ) of bulk systems: 3×3×3 for $MgCl_2 \bullet 6H_2O$, $MgCl_2 \bullet 4H_2O$ and

$K_2Ca_2Mg(SO_4)_4•2(H_2O)$, 3×3×5 for $MgCl_2·2H_2O$, 3×5×3 for $MgCl_2•H_2O$, 3×5×3 for $CaSO_4$ and 2×2×3 for $KMgCl_3•6(H_2O)$. The tetrahedron method with Blöchl corrections (Blöchl, Jepsen, and Andersen, 1994) was used for BZ integrations. Ionic and cell relaxations of the bulk structures were performed simultaneously, without symmetry constraints.

Periodic unit cells were used in the calculations, with 42 atoms for $MgCl_2•6H_2O$ (Z = 2), 60 atoms for $MgCl_2•4H_2O$ (Z = 4), 18 atoms for $MgCl_2•2H_2O$ (Z = 2), 24 atoms for $MgCl_2•H_2O$ (Z = 4), 24 atoms for $CaSO_4$ (Z = 4), 30 atoms for $K_2Ca_2Mg(SO_4)_4•2(H_2O)$ (Z = 1) and 276 atoms $KMgCl_3•6(H_2O)$ (Z = 12).

1.2.2 Results and Discussion

Structure and Electronic Properties of Bischofite, $MgCl_2•6H_2O$

Figure 1 shows the crystal unit cell of magnesium dichloride hexahydrate ($MgCl_26•H_2O$, bischofite) optimized at the GGA/PBE level of theory. $MgCl_2•6H_2O$ crystallizes in the monoclinic space group C 2/m (IT #12), with two formula units (Z = 2) per unit cell, and the computed lattice parameters are: a = 9.91 Å, b = 7.16 Å, c = 6.12 Å; $\alpha = \gamma = 90°$, β = 94.25° (V = 433.18 Å^3; b/a = 0.72, c/a = 0.62). Each Mg^{2+} ion is octahedrally coordinated by six water molecules, with two neighboring Cl^- ions per formula unit to compensate the charge of Mg^{2+}. The computed Mg—OH_2 bond distances are in the range 2.07 and 2.09 Å and the H···Cl hydrogen bonds vary between 2.18 and 2.51 Å. The Mg atoms are positioned on 2a Wyckoff sites (2/m symmetry), the Cl atoms occupy 4i sites (m symmetry), and the O and H atoms are on both 4i sites (m symmetry) and 8j sites (1 symmetry).

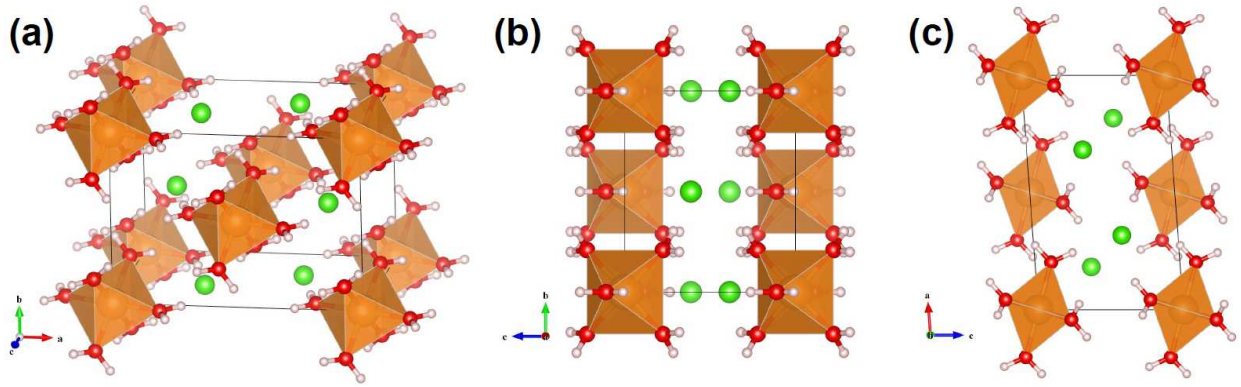

Figure 1. Crystal structure of $MgCl_2·6H_2O$ (space group C 2/m; Z = 2) optimized at the DFT/PBE level of theory. (a) 3D view; (b) view along the [100] direction; (c) view along the [010] direction. Color legend: Mg, orange; O, red; Cl, green; H, white.

The optimized structure slightly overestimates the lattice parameters of the structure characterized by Agron and Busing (Agron and Busing, 1985) using neutron diffraction: a = 9.8607 Å, b = 7.1071 Å, c = 6.0737 Å; $\alpha = \gamma = 90°$, β = 93.758° (V = 424.736 Å^3; b/a = 0.7207, c/a = 0.6159), although the computed b/a and c/a ratios are in excellent agreement with experiment. The computed equilibrium volume is 2.0% larger than the experimental estimate,

due to the fact that GGA calculations tend to overestimate the bond distances (Grinberg, Ramer, and Rappe, 2001) and that standard DFT cannot account accurately for long-range intermolecular forces (Kohn, Meir, and Makarov, 1998). The Mg—OH_2 bond distances determined experimentally are 2.057 and 2.062 Å and the experimental H···Cl hydrogen bonds vary between 2.206 and 2.499 Å.

The total and partial densities of states (DOS) of bischofite computed at the DFT/PBE level of theory are displayed in Figure 2. The DOS exhibit characteristic features of molecular solids, with very localized peaks contrasting with the wide bands often seen in other solids with a larger degree of electron hybridization. The energy band gap between the top of the valence band and the bottom of the conduction band is 5.10 eV, indicative of an insulator. The main contributions to the total DOS near the Fermi level (i.e. E_F = 0 eV) originate from the Cl(3p), O(2p) and H(1s) orbitals. The Cl(p) electrons contribute predominantly in the range -1.3 to +0.1 eV, the O(p) electrons in the ranges -1.8 to +0.1 eV, -4.2 to -3.1 eV and -7.3 to -6.4 eV, and the H(s) electrons in the range -7.3 to -6.4 eV.

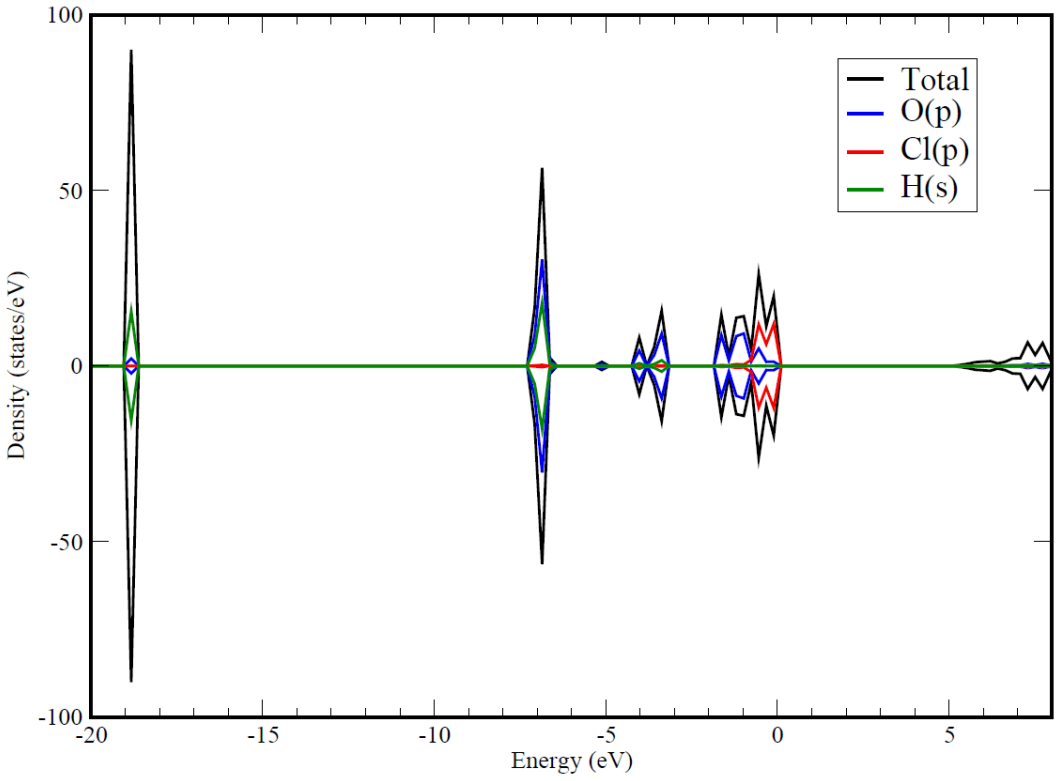

Figure 2. Total and partial densities of states (DOS) of $MgCl_2$•$6H_2O$, per unit cell, computed at the DFT/PBE level of theory.

Structure and Electronic Properties of $MgCl_2$•$4H_2O$

Figure 3 shows the crystal unit cell of magnesium dichloride tetrahydrate ($MgCl_2$•$4H_2O$) optimized at the GGA/PBE level of theory. $MgCl_2$•$4H_2O$ crystallizes in the orthorhombic space

group *Pbcn* (IT #60), with four formula units (Z = 4) per unit cell, and the computed lattice parameters are: a = 7.38 Å, b = 8.42 Å, c = 11.00 Å; $\alpha = \beta = \gamma = 90°$ (V = 683.63 Å^3; b/a = 1.14, c/a = 1.49). Each Mg^{2+} ion is coordinated by 4 water molecules in a square-planar arrangement, with two neighboring Cl^- ions *trans*-positioned 2.59 Å away from the Mg^{2+} ion with a mirror symmetry relative to this plane. The computed Mg—OH_2 bond distances are in the range 2.07-2.08 Å and the H···Cl hydrogen bonds vary between 2.19 and 2.22 Å. The Mg atoms are positioned on 4*c* Wyckoff sites (.2. symmetry), the Cl atoms occupy 8*d* sites (1 symmetry), the O atoms are on both 4*c* sites (2 symmetry) and 8*d* sites (1 symmetry), and all the H atoms occupy 8*d* sites (1 symmetry).

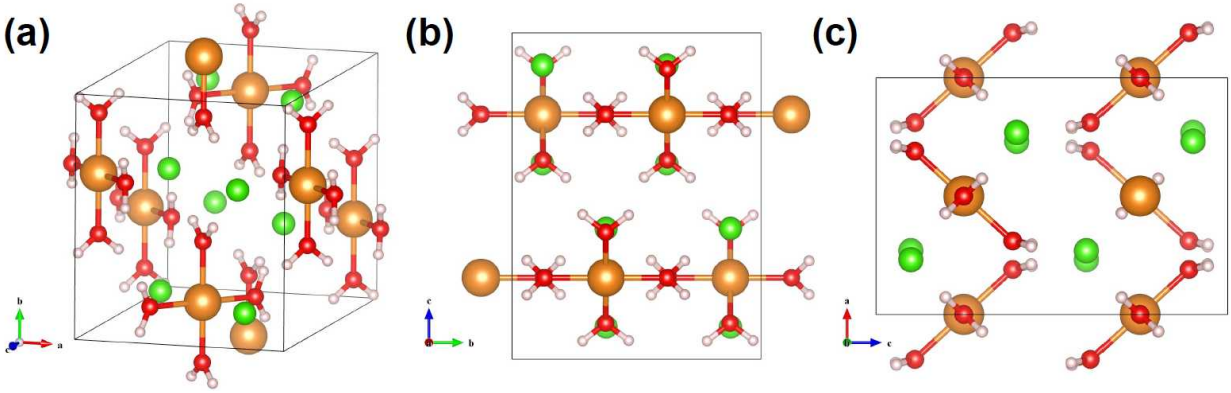

Figure 3. Crystal structure of $MgCl_2{\cdot}4H_2O$ (space group *Pbcn*; Z = 4) optimized at the DFT/PBE level of theory. (a) 3D view; (b) view along the [100] direction; (c) view along the [010] direction. Color legend: Mg, orange; O, red; Cl, green; H, white.

The optimized structure slightly overestimates the lattice parameters of the structure recently characterized by Schmidt et al. (Schmidt, Hennings, and Voigt, 2012) using X-ray diffraction (XRD): a = 7.2557(3) Å, b = 8.4285(4) Å, c =11.0412(6) Å; $\alpha = \beta = \gamma = 90°$ (V = 675.22(6) Å^3; b/a = 1.1616, c/a = 1.5217) and the computed b/a and c/a ratios are in good agreement with experiment. The computed equilibrium volume is about 1.2% larger than the experimental estimate. The Mg—OH_2 bond distances determined experimentally are 2.052 and 2.058 Å, the Mg—Cl distance is 2.551 and the experimental H···Cl hydrogen bonds vary between 2.345 and 2.431 Å.

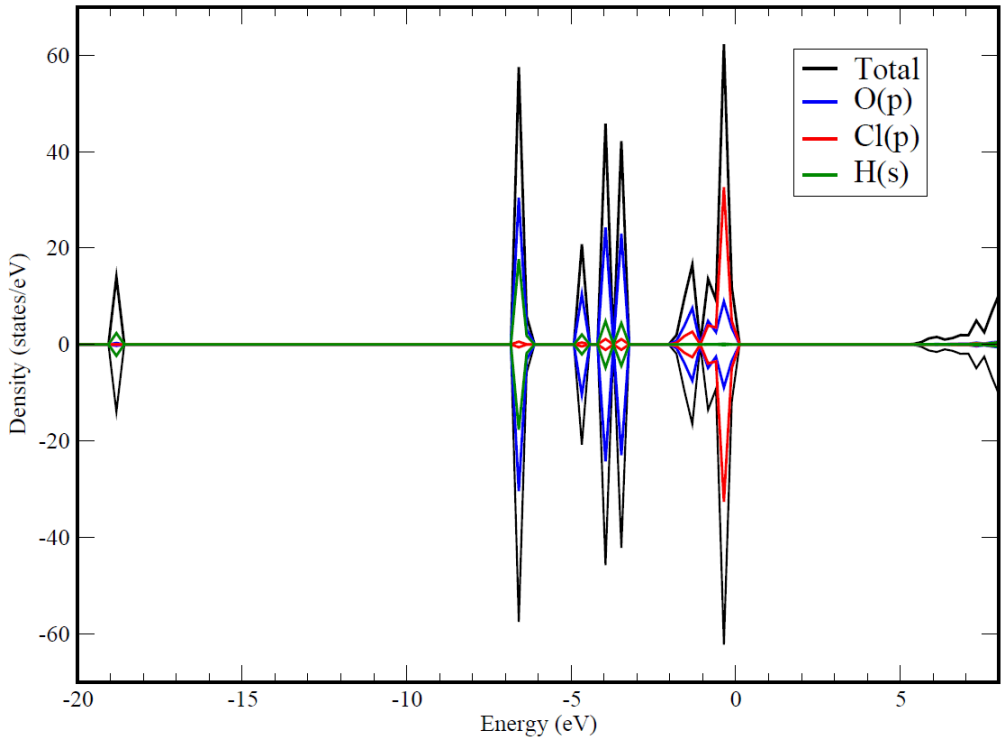

Figure 4. Total and partial density of states (DOS) of $MgCl_2 \bullet 4H_2O$, per unit cell, computed at the DFT/PBE level of theory.

The total and partial densities of states (DOS) of $MgCl_2 \bullet 4H_2O$ computed at the DFT/PBE level of theory are displayed in Figure 4. The energy band gap between the top of the valence band and the bottom of the conduction band is 5.17 eV, indicative of an insulator. Similar to $MgCl_2 \cdot 6H_2O$, the main contributions to the total DOS near the Fermi level originate from the Cl(3p), O(2p) and H(1s) orbitals. A strong hybridization between the Cl(3p) and O(2p) electrons is seen between -2.0 and +0.1 eV, while O(2p)-H(1s) hybridization occurs for lower-lying bands, below -3.2 eV and above -6.8 eV.

Structure and Electronic Properties of $MgCl_2 \bullet 2H_2O$

Figure 5 depicts the crystal unit cell of magnesium dichloride dihydrate ($MgCl_2 \cdot 2H_2O$) optimized at the GGA/PBE level of theory. $MgCl_2 \cdot 2H_2O$ crystallizes in the monoclinic space group *C*2/*m* (IT #12), with two formula units ($Z = 2$) per unit cell, and the computed lattice parameters are: $a = 7.90$ Å, $b = 8.50$ Å, $c = 3.70$ Å; $\alpha = \gamma = 90°$, $\beta = 104.0°$ ($V = 241.06$ Å^3; $b/a = 1.07$, $c/a = 0.47$). Each Mg^{2+} ion is coordinated by 2 water molecules along the *b* axis, with two neighboring Cl^- ions bridging adjacent Mg^{2+} ions and forming polymeric chains propagating along the *c* axis, with Mg—Cl bond distances of 2.52 and 2.58 Å. The computed Mg—OH_2 bond distance is 2.05 Å and the H···Cl hydrogen bond distance between adjacent chains is 2.20 Å. The Mg atoms are positioned on 2*a* Wyckoff sites (2/*m* symmetry), the Cl atoms occupy 4*i* sites (*m* symmetry), the O atoms are on 4g sites (2 symmetry) and the H atoms occupy 8*j* sites (1 symmetry).

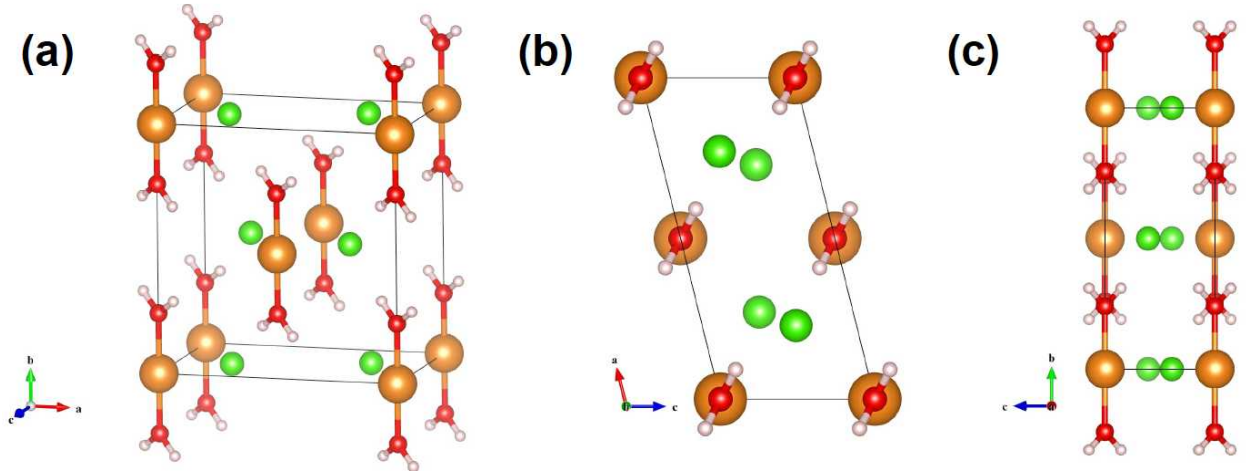

Figure 5. Crystal structure of $MgCl_2 \cdot 2H_2O$ (space group *C2/m*; *Z* = 2) optimized at the DFT/PBE level of theory. (a) 3D view; (b) view along the [100] direction; (c) view along the [010] direction. Color legend: Mg, orange; O, red; Cl, green; H, white.

The optimized structure overestimates the lattice parameters of the structure characterized by Sugimoto et al. (Sugimoto, Dinnebier, and Hanson, 2007) using XRD: a = 7.4279(4) Å, b = 8.5736(4) Å, c = 3.65065(16) Å; $\alpha = \gamma = 90°$, β = 98.580(2)° (V = 229.886 Å^3; b/a = 1.1542, c/a = 0.4915. The computed equilibrium volume is 4.6% larger than the experimental estimate. The Mg—OH_2 bond distance determined experimentally is 2.008 Å, with Mg—Cl bond distances of 2.489 and 2.559 Å, and the experimental H···Cl hydrogen bonds vary between 2.447 and 3.072 Å. A major difference observed between observed and computed structures is the orientation of water molecules, explaining in part the much larger predicted unit-cell volume compared with experiment.

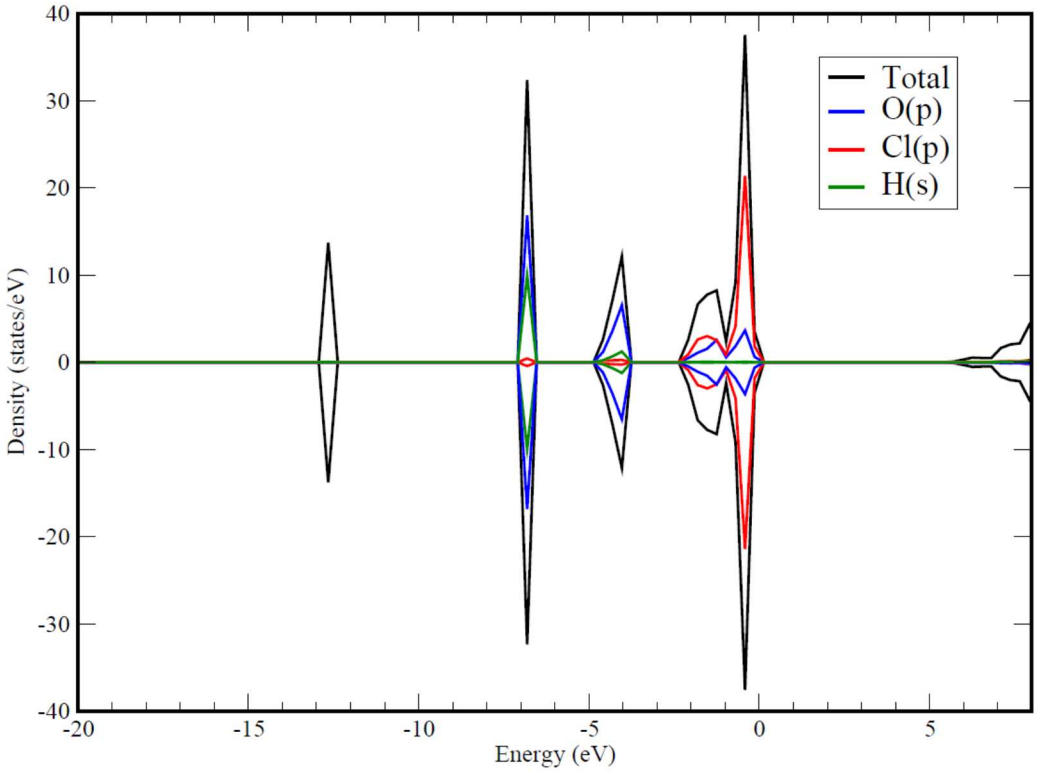

Figure 6. Total and partial density of states (DOS) of $MgCl_2$•$2H_2O$, per unit cell, computed at the DFT/PBE level of theory.

The total and partial densities of states (DOS) of $MgCl_2$•$2H_2O$ computed at the DFT/PBE level of theory are displayed in Figure 6. Calculations show that this compound is also an insulator with an energy band gap of 5.39 eV between the top of the valence band and the bottom of the conduction band. As in the previous cases, the Cl(3p), O(2p) and H(1s) orbitals dominate the top of the valence band. The computed DOS is reminiscent of $MgCl_2 \cdot nH_2O$ (n = 4, 6), with the Cl(p) electrons featuring importantly between -2.3 to +0.2 eV, with some O(2p) hybridization in this range, while O(2p) are predominant in the narrower ranges -4.8 to -3.7 eV and -7.0 to -6.4. Strong O(p)-H(s) hybridization is predicted in the latter range.

Structure and Electronic Properties of $MgCl_2 \bullet H_2O$

Figure 7 shows the crystal unit cell of magnesium dichloride monohydrate ($MgCl_2 \bullet H_2O$) optimized at the GGA/PBE level of theory. $MgCl_2 \bullet H_2O$ crystallizes in the orthorhombic space group *Pnma* (IT #62), with four formula units ($Z = 4$) per unit cell, and the computed lattice parameters are: $a = 8.98$ Å, $b = 3.69$ Å, $c = 11.58$ Å; $\alpha = \beta = \gamma = 90°$ ($V = 383.65$ Å^3; $b/a = 1.07$, $c/a = 0.47$). Each Mg^{2+} ion is octahedrally coordinated by one water molecule at 2.02 Å and Cl^- ions with Mg—Cl bond distances of 2.52, 2.53 and 2.58 Å; the structure consists of polymeric chains propagating along the *b* axis. The computed H···Cl hydrogen bond distance between adjacent chains is 2.29 Å. All the atoms in the structure are positioned on 4*c* Wyckoff sites (*.m.* symmetry).

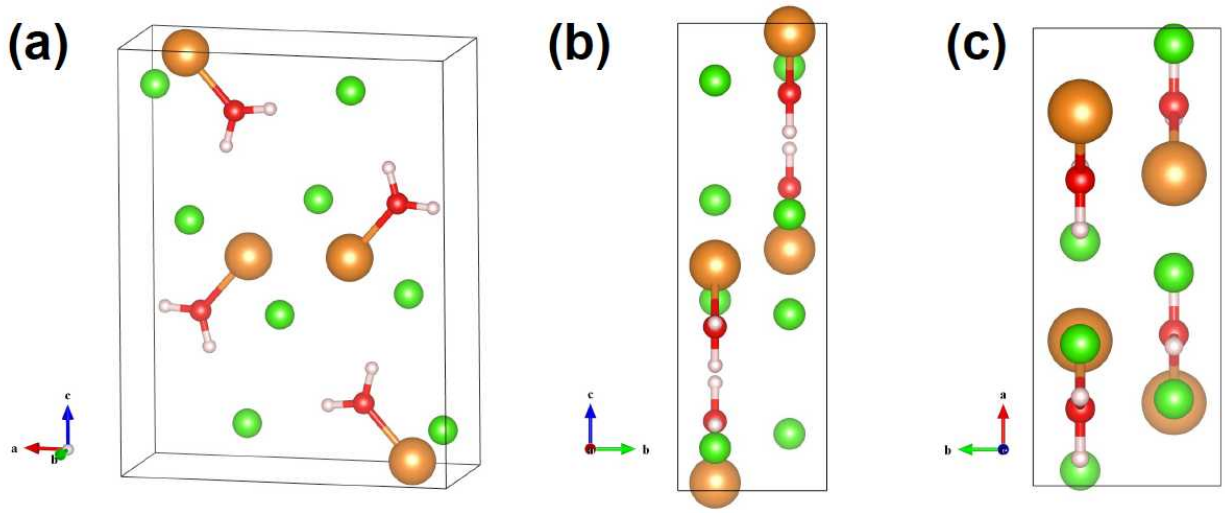

Figure 7. Crystal structure of $MgCl_2 \cdot H_2O$ (space group *Pnma*; $Z = 4$) optimized at the DFT/PBE level of theory. (a) 3D view; (b) view along the [100] direction; (c) view along the [010] direction. Color legend: Mg, orange; O, red; Cl, green; H, white.

The optimized structure overestimates the lattice parameters of the structure characterized by Sugimoto et al. (Sugimoto, Dinnebier, and Hanson, 2007) using XRD: $a = 8.9171(6)$, Å, $b = 3.63421(18)$ Å, $c = 11.4775(7)$ Å; $\alpha = \beta = \gamma = 90°$ ($V = 371.95(4)$ Å^3; $b/a = 0.4075$, $c/a = 1.2871$). The computed equilibrium volume is 3.1% larger than the experimental estimate. The Mg—OH_2 bond distance determined experimentally is 1.918 Å, with Mg—Cl bond distances of 2.466, 2.551 and 2.560 Å, and the experimental H···Cl hydrogen bond between adjacent chains is measured to be 2.374 Å, i.e. appreciably longer than in the relaxed structure.

The total and partial densities of states (DOS) of $MgCl_2 \cdot H_2O$ computed at the DFT/PBE level of theory are displayed in Figure 8. In this insulating compound, the predicted energy band gap separating the top of the valence band from the bottom of the conduction band is 5.76 eV. Similar to the compounds discussed above, the Cl(p), O(2p) and H(1s) orbitals are predominant near the top of the valence band. The Cl(p) electrons contribute predominantly in the range -2.6 to +0.0 eV, with some degree of hybridization with O(p) electrons, while the ranges -4.6 to -3.9

eV and -7.2 to -6.7 eV are characterized essentially by O(p) electrons, with some mixing with H(s) electrons in the latter range.

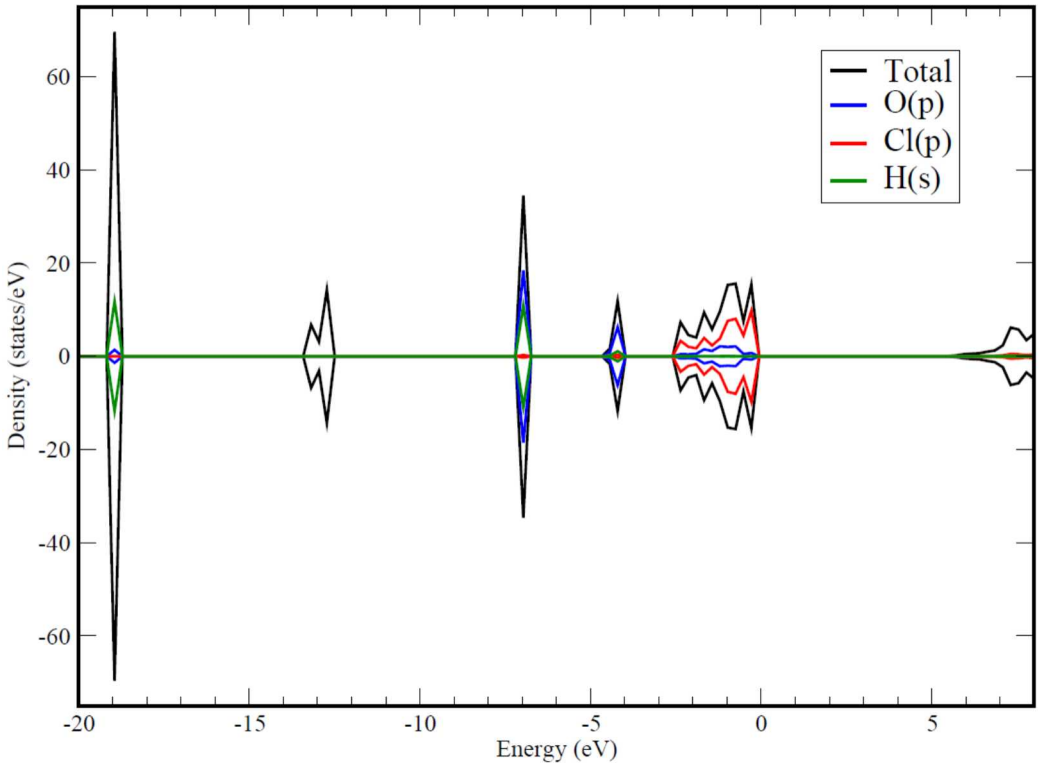

Figure 8. Total and partial density of states (DOS) of $MgCl_2 \cdot H_2O$, per unit cell, computed at the DFT/PBE level of theory.

Structure and Electronic Properties of Anhydrite, $CaSO_4$

The crystal unit cell of anhydrite ($CaSO_4$) optimized at the GGA/PBE level of theory is shown in Figure 9. Anhydrite crystallizes in the orthorhombic space group *Amma* (IT #63), with four formula units ($Z = 4$) per unit cell, and the computed lattice parameters are: $a = 7.08$ Å, $b = 7.09$ Å, $c = 6.28$ Å; $\alpha = \beta = \gamma = 90°$ ($V = 315.64$ Å^3; $b/a = 1.00$, $c/a = 0.89$). The Ca dodecahedra and the S tetrahedral composing the anhydrite structure form alternating edge-sharing chains propagating along the *c* axis. These link along the *a* axis by edge-sharing of the dodecahedra and alternating edge-sharing chains link along the *b* axis by corner-sharing between polyhedra. The computed Ca—O bond distances in the dodecahedra vary between 2.37 and 2.58 Å and the S—O bond distance is 1.49 Å in the tetrahedra. The Ca and S atoms are positioned on 4*c* Wyckoff sites (*m*2*m* symmetry), and the O atoms occupy 8*g* sites (..*m* symmetry) and 8*f* sites (*m*.. symmetry).

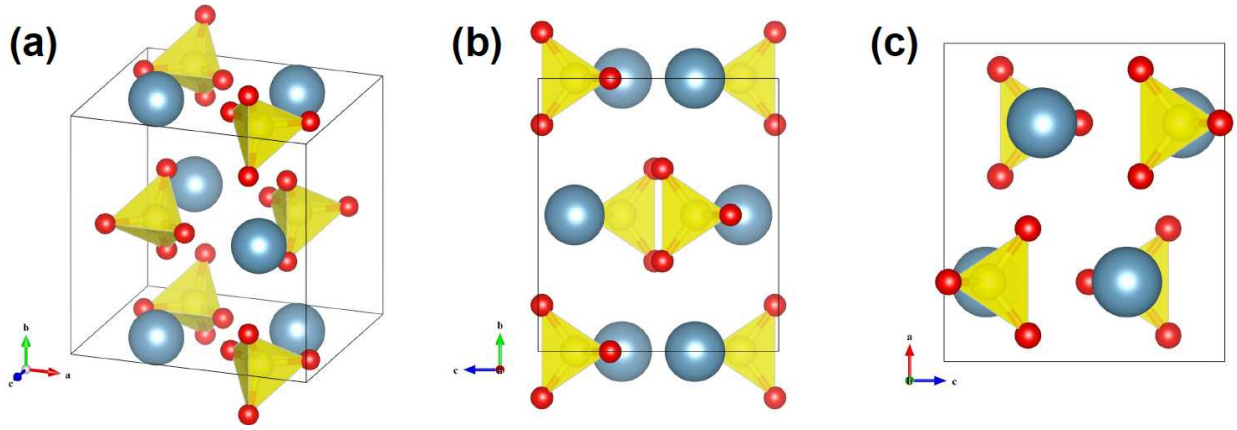

Figure 9. Crystal structure of anhydrite, $CaSO_4$ (space group *Amma*; Z = 4), optimized at the DFT/PBE level of theory. (a) 3D view; (b) view along the [100] direction; (c) view along the [010] direction. Color legend: Ca, blue; O, red; S, yellow.

The optimized structure slightly overestimates the lattice parameters of the structure characterized by Hawthorne and Ferguson (Hawthorne and Ferguson, 1975) using X-ray diffraction (XRD): a = 6.993 Å, b = 6.995 Å, c = 6.245 Å; $\alpha = \beta = \gamma = 90°$ (V = 305.481 Å^3; b/a = 1.000, c/a = 0.893) and the computed b/a and c/a ratios are in perfect agreement with experiment. The computed equilibrium volume is about 3.3% larger than the experimental estimate. The measured Ca—O bond distances in the dodecahedra vary between 2.342 and 2.564 Å and the experimental S—O bond distances are 1.472 and 1.473 Å.

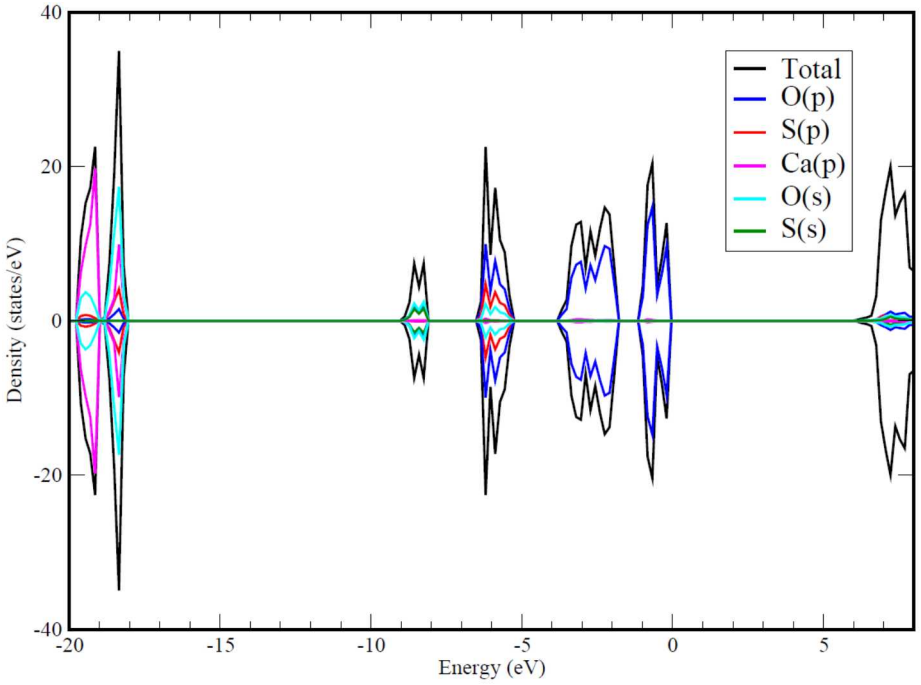

Figure 10. Total and partial density of states (DOS) of anhydrite, $CaSO_4$, per unit cell, computed at the DFT/PBE level of theory.

The total and partial densities of states (DOS) of anhydrite computed at the DFT/PBE level of theory are displayed in Figure 10. Anhydrite exhibits some insulating character, with a computed energy band gap of 6.12 eV between the top of the valence band and the bottom of the conduction band. The top of the valence band is predominantly occupied by O(2p) electrons in the ranges -1.1 to 0.0 eV, -3.8 to -1.7 eV, -6.5 and -5.2 eV and -9.0 and -8.1 eV. Strong O(2p)-S(3p) hybridization is predicted in the -6.5 and -5.2 eV range to form the SO_4 tetrahedra. Additionally, O(2s,2p)-S(3s) hybridization is seen in the range -9.0 and -8.1 eV. Ca(3p) contribute to the DOS for lower-lying bands in the range -19.8 to -18.0 and mix with O(2s) electrons.

Structure and Electronic Properties of Polyhalite, $K_2Ca_2Mg(SO_4)_4 \bullet 2(H_2O)$

Figure 11 shows the crystal unit cell of polyhalite ($K_2Ca_2Mg(SO_4)_4 \bullet 2(H_2O)$, dipotassium dicalcium magnesium tetrakis[sulfate(VI)] dihydrate) optimized at the GGA/PBE level of theory. Polyhalite crystallizes in the triclinic space group *P*-1 (IT #2), with one formula unit ($Z = 1$) per unit cell, and the computed lattice parameters are: a = 7.09 Å, b = 7.10 Å, c = 8.96 Å; α = 103.8°, β = 100.6°, γ = 114.6° (V = 377.14 Å^3; b/a = 1.00, c/a = 1.26). The structure consists of K and Ca polyhedra and $[MgO_4(H_2O)_2]$ octahedra sharing edges and faces and SO_4 tetrahedra sharing edges with the polyhedra. The computed K—O and Ca—O bond distances in the polyhedra vary in the ranges 2.78-3.36 Å and 2.41-2.65 Å, respectively, the Mg—O bond distances range between 2.04 and 2.19 Å and the S—O bond distances in the tetrahedra are in the range 1.48-1.51 Å. With the exception of Mg atoms which occupy 1*a* sites (-1 symmetry), all the other atoms are positioned on 2*i* Wyckoff sites (1 symmetry).

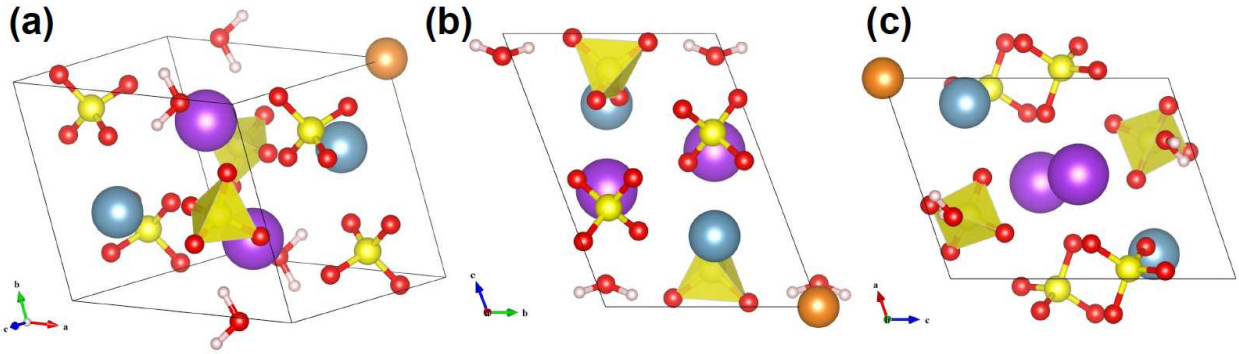

Figure 11. Crystal structure of polyhalite, $K_2Ca_2Mg(SO_4)_4 \bullet 2(H_2O)$ (space group *P*-1; Z = 1), optimized at the DFT/PBE level of theory. (a) 3D view; (b) along the [100] direction; (c) along the [010] direction. Color legend: K, purple; Ca, blue; Mg, orange; O, red; S, yellow; H, white.

The optimized structure slightly overestimates the lattice parameters of the structure recently characterized by Bindi (Bindi, 2005) using XRD: a = 6.975(3) Å, b = 6.984(3) Å, c = 8.899(3) Å; α = 104.01(3)°, β = 101.19(3)°, γ = 114.10(6)° (V = 362.337 Å^3; b/a = 1.001, c/a = 1.276) and the computed b/a and c/a ratios essentially reproduce experimental ratios. The computed equilibrium volume is about 4.1% larger than the experimental estimate. The measured K—O

and Ca—O bond distances vary in the ranges 2.768-3.196 Å and 2.400-2.686 Å, respectively, the experimental Mg—O bond distances range between 2.017 and 2.163 Å and the observed S—O bond distances are in the range 1.461-1.504 Å.

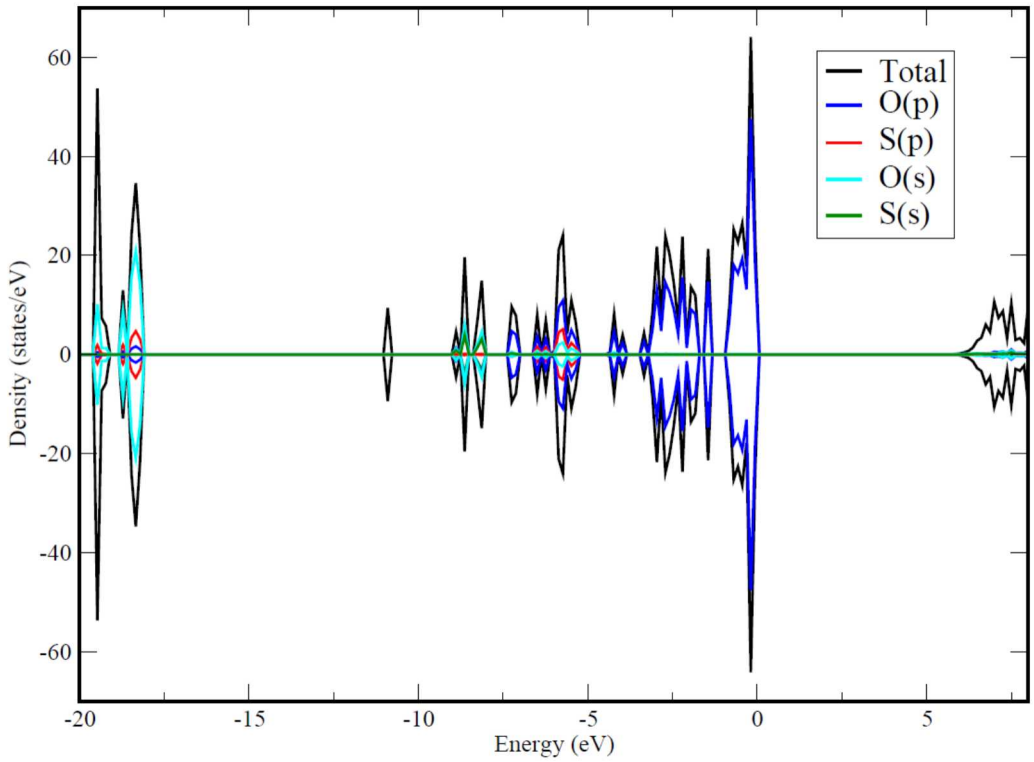

Figure 12. Total and partial density of states (DOS) of polyhalite, $K_2Ca_2Mg(SO_4)_4 \bullet 2(H_2O)$, per unit cell, computed at the DFT/PBE level of theory.

The total and partial densities of states (DOS) of polyhalite computed at the DFT/PBE level of theory are displayed in Figure 12. The calculated energy band gap separating the top of the valence band and the bottom of the conduction band is 5.87 eV. Similar to anhydrite, O(2s,2p) and S(3s,3p) electrons are the main contributors to the valence bands in the vicinity of the Fermi level. The O(2p) electrons are dominant in the range -7.3 to +0.1 eV, with some strong O(2s,2p)-S(3p) and O(2s)-S(3s) hybridization in the bands lying in the energy ranges -6.6 to -5.2 eV and -9.0 to -8,0 eV, respectively.

Structure and Electronic Properties of Carnallite, $KMgCl_3 \bullet 6(H_2O)$

The crystal unit cell of carnallite ($KMgCl_3 \bullet 6(H_2O)$) optimized at the GGA/PBE level of theory is displayed in Figure 13. Carnallite crystallizes in the orthorhombic space group *Pnna* (IT #52), with 12 formula units ($Z = 12$) per unit cell, and the computed lattice parameters are: $a = 16.28$ Å, $b = 22.83$ Å, $c = 9.59$ Å; $\alpha = \beta = \gamma = 90°$ ($V = 3564.13$ Å^3; $b/a = 1.40$, $c/a = 0.59$). The crystal structure of carnallite consists of a network of face-sharing KCl_6 octahedra and of isolated $Mg(H_2O)_6$ octahedra occupying the openings in the KCl network, with the water molecules

acting as charge transmitters between Mg^{2+} and Cl^{-} ions. The computed interatomic distances are 2.06-2.09 Å for Mg—OH_2 and 3.18-3.36 Å for K—Cl forming octahedra and the H···Cl hydrogen bonds are predicted to be in the range 2.14-2.19 Å. The K atoms occupy 4*c* Wyckoff sites (..2 symmetry) and 8*e* Wyckoff sites (1 symmetry), the Mg atoms are positioned on 4*d* sites (2.. symmetry) and 8*e* sites (1 symmetry), Cl and O atoms are on 4*d* sites (2.. symmetry) and 8*e* sites (1 symmetry) and H occupy 8*e* sites (1 symmetry).

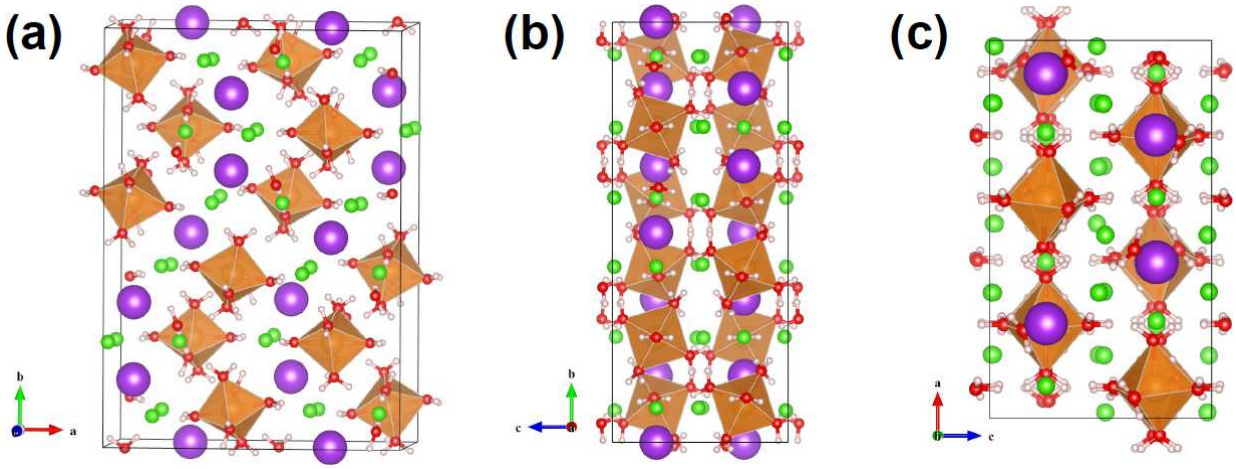

Figure 13. Crystal structure of carnallite, $KMgCl_3 \cdot 6(H_2O)$ (space group *Pnna*; Z = 12), optimized at the DFT/PBE level of theory. (a) 3D view; (b) along the [100] direction; (c) along the [010] direction. Color legend: K, purple; Mg, orange; O, red; Cl, green; H, white.

The optimized structure slightly overestimates the lattice parameters of the structure characterized by Schlemper et al. (Schlemper, Sen Gupta, and Zoltai, 1985) using X-ray diffraction (XRD): a = 16.119(3) Å, b = 22.472(4) Å, c = 9.551(2) Å; $\alpha = \beta = \gamma = 90°$ (V = 3459.622 $Å^3$; b/a = 1.394, c/a = 0.592) and the computed b/a and c/a ratios are in good agreement with experiment. The computed equilibrium volume is about 3.0% larger than the experimental estimate. The measured interatomic distances in the octahedra are 2.027-2.053 Å for Mg—OH_2 and 3.154-3.321 Å for K—Cl and the experimental H···Cl hydrogen bonds are in the range 2.255-2.429 Å.

The total density of states (DOS) of carnallite computed at the DFT/PBE level of theory are displayed in Figure 14. Carnallite is also an insulator, with a predicted energy band gap between the top of the valence band and the bottom of the conduction band of 5.05 eV. Due to the large size of the system the partial DOS was not calculated for carnallite, however, based on the previous results, it can be inferred that the predominant contributions at the top of the valence band will come from O(2p), Cl(3p) and H(1s) electrons.

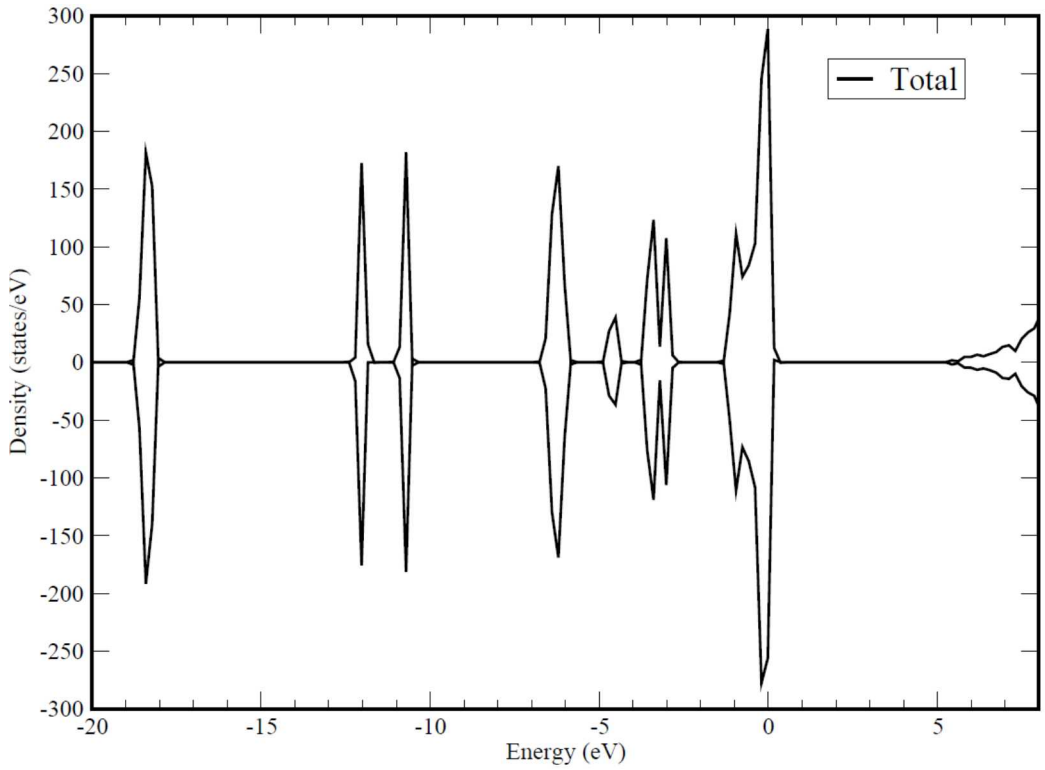

Figure 14. Total density of states (DOS) of carnallite, $KMgCl_3 \bullet 6(H_2O)$, per unit cell, computed at the DFT/PBE level of theory.

1.2.3 First Principles Evaluation of Thermal Properties of Bischofite, Dehydrated Bischofite, Anhydrite, and Polyhalite

In this section, the thermal properties of bischofite ($MgCl_2 \bullet 6H_2O$), dehydrated bischofite ($MgCl_2 \bullet 4H_2O$, $MgCl_2 \bullet 2H_2O$ and $MgCl_2 \bullet H_2O$), anhydrite ($CaSO_4$) and polyhalite ($K_2Ca_2Mg(SO_4)_4 \bullet 2(H_2O)$) were calculated using density functional perturbation theory (DFPT) at the GGA/PBE level of theory. Specifically, the internal energy, the phonon (Helmholtz) free energy, the entropy and isochoric heat capacity were calculated at constant equilibrium volume. Thermal properties at constant pressure such as the Gibbs free energy and the isobaric heat capacity were also computed. Details of our computational approach are given in the next section, followed by a complete report of our results.

1.2.3.1 Computational Methods

The equilibrium structures of $MgCl_2 \bullet 6H_2O$, $MgCl_2 \bullet 4H_2O$, $MgCl_2 \bullet 2H_2O$, $MgCl_2 \bullet H_2O$, $CaSO_4$ and $K_2Ca_2Mg(SO_4)_4 \bullet 2(H_2O)$ previously optimized using the VASP software package were used to build a set of supercells. The forces exerted on atoms of the set of supercells were calculated using density functional perturbation theory (DFPT) with VASP at the GGA/PBE level of theory and phonon frequencies were computed. Phonon analysis was performed at constant equilibrium volume in order to derive isochoric thermal properties (e.g., the phonon (Helmholtz) free energy, the entropy and the isochoric heat capacity). The Helmholtz free energy was calculated using the following formula:

$$F = \frac{1}{2}\sum \hbar\omega + k_B T \sum \ln\left[1 - e^{-\hbar\omega/k_B T}\right].$$

The entropy was computed using the expression:

$$S = -k_B \sum \ln\left[1 - e^{-\hbar\omega/k_B T}\right] - \frac{1}{\mathrm{T}}\sum \frac{\hbar\omega}{e^{\hbar\omega/k_B T} - 1}.$$

The heat capacity at constant volume was calculate using the formula:

$$C_V = \sum k_B \left[\frac{\hbar\omega}{k_B T}\right]^2 \frac{e^{\hbar\omega/k_B T}}{[e^{\hbar\omega/k_B T} - 1]^2}.$$

Further analysis from a set of phonon calculations in the vicinity of each computed equilibrium crystal structure was carried out to obtain thermal properties at constant pressure (e.g., the Gibbs free energy and the isobaric heat capacity) within a quasi-harmonic approximation (QHA). The QHA mentioned here introduces volume dependence of phonon frequencies as a part of anharmonic effect. A part of temperature effect can be included into the total energy of electronic structure through the phonon (Helmholtz) free energy at constant volume, but thermal properties at constant pressure are the desired quantities. Therefore, some transformation from a function of volume V to a function of pressure p is needed. The Gibbs free energy is defined at a constant pressure by the transformation:

$$G(T, p) = \min_V \left[U(V) + F_{phonon}(T; V) + pV\right],$$

where $\min_V[\text{ function of } V]$ means to find unique minimum value in the brackets by changing volume. Since volume dependencies of energies in electronic and phonon structures are different, volume giving the minimum value of the energy function in the square brackets shifts from the value calculated only from electronic structure even at T = 0 K. By increasing temperature, the volume dependence of phonon free energy changes, then the equilibrium volume at temperatures changes.

The heat capacity at constant pressure versus temperature was also derived as the second derivative of the Gibbs free energy with respect to T, i.e.:

$$C_P = -T\frac{\partial^2 G}{\partial T^2}.$$

1.2.4 Results

The results for the thermal properties at constant, equilibrium volume (i.e., the total energy U, the phonon (Helmholtz) free energy F, the entropy S, and the isochoric heat capacity C_V) and at constant pressure (i.e., the Gibbs free energy G and the isobaric heat capacity C_P) are reported below for $MgCl_2 \bullet 6H_2O$, $MgCl_2 \bullet 4H_2O$, $MgCl_2 \bullet 2H_2O$, $MgCl_2 \bullet H_2O$, $CaSO_4$, and $K_2Ca_2Mg(SO_4)_4 \bullet 2(H_2O)$.

Thermal Properties of Bischofite, $MgCl_2 \bullet 6H_2O$

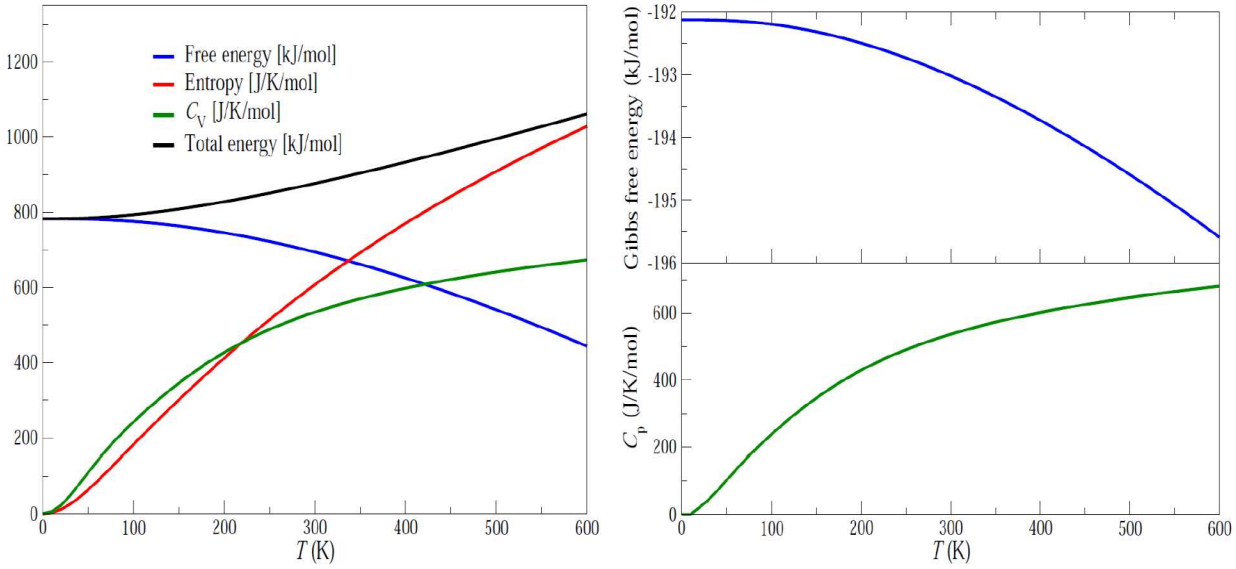

Figure 15. Thermal properties of $MgCl_2 \bullet 6H_2O$ calculated at the DFT/PBE level of theory. *Left*: thermal properties at constant equilibrium volume. *Right*: Thermal properties at constant pressure.

Thermal Properties of Dehydrated Bischofite, $MgCl_2 \bullet 4H_2O$

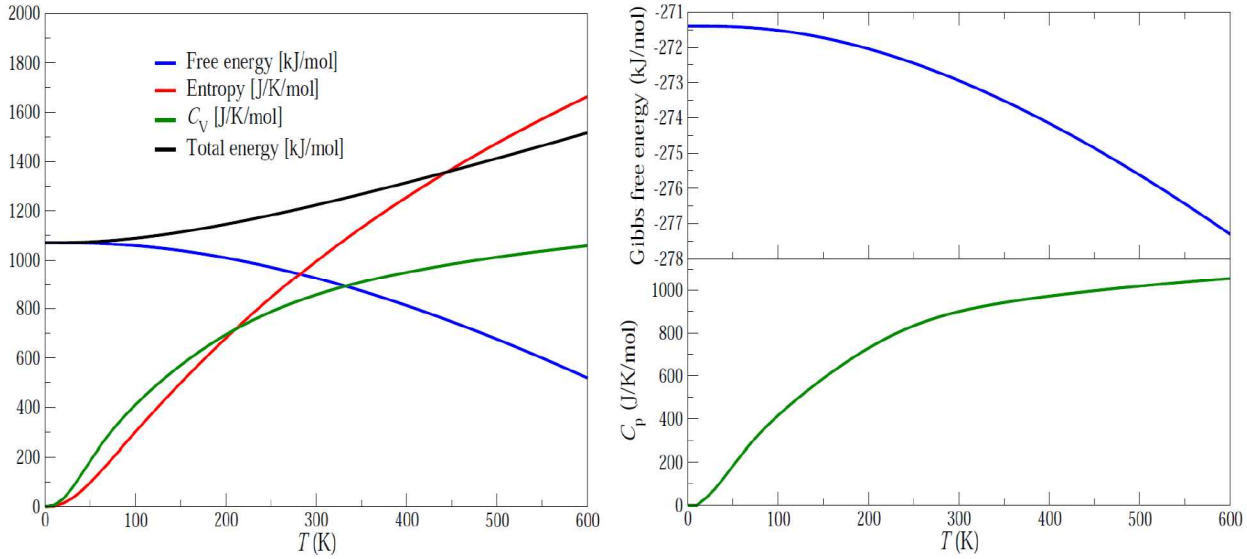

Figure 16. Thermal properties of $MgCl_2 \bullet 4H_2O$ calculated at the DFT/PBE level of theory. *Left*: thermal properties at constant equilibrium volume. *Right*: Thermal properties at constant pressure.

Thermal Properties of Dehydrated Bischofite, $MgCl_2 \bullet 2H_2O$

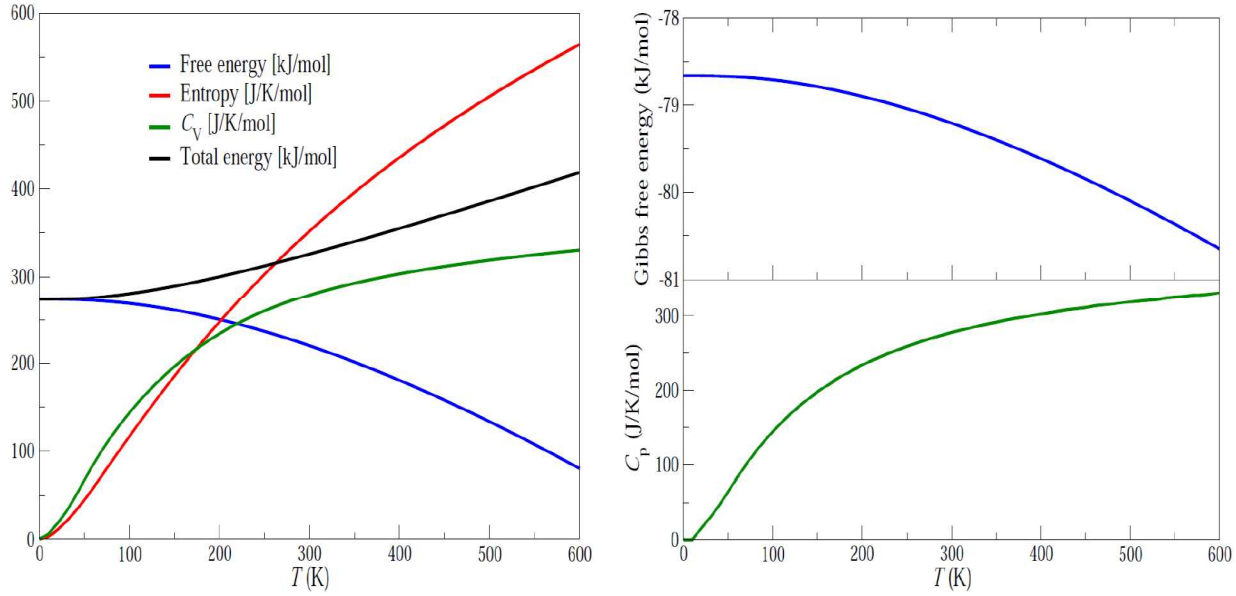

Figure 17. Thermal properties of $MgCl_2 \bullet 2H_2O$ calculated at the DFT/PBE level of theory. *Left*: thermal properties at constant equilibrium volume. *Right*: Thermal properties at constant pressure.

Thermal Properties of Dehydrated Bischofite, $MgCl_2 \bullet H_2O$

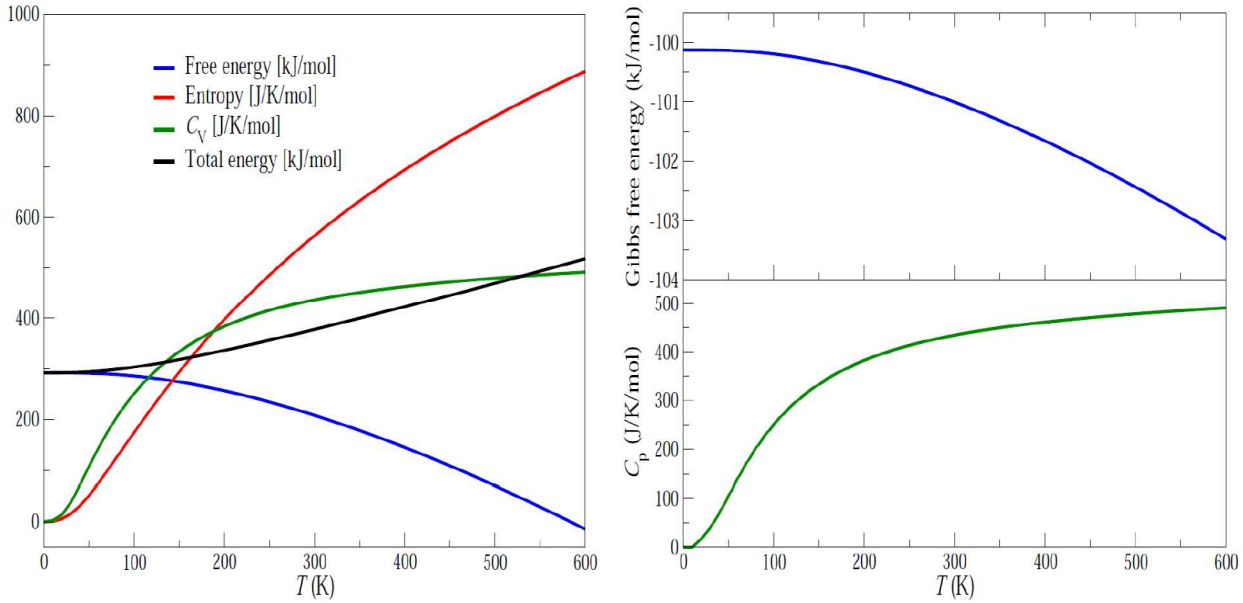

Figure 18. Thermal properties of $MgCl_2 \bullet H_2O$ calculated at the DFT/PBE level of theory. *Left*: thermal properties at constant equilibrium volume. *Right*: Thermal properties at constant pressure.

Thermal Properties of Anhydrite, $CaSO_4$

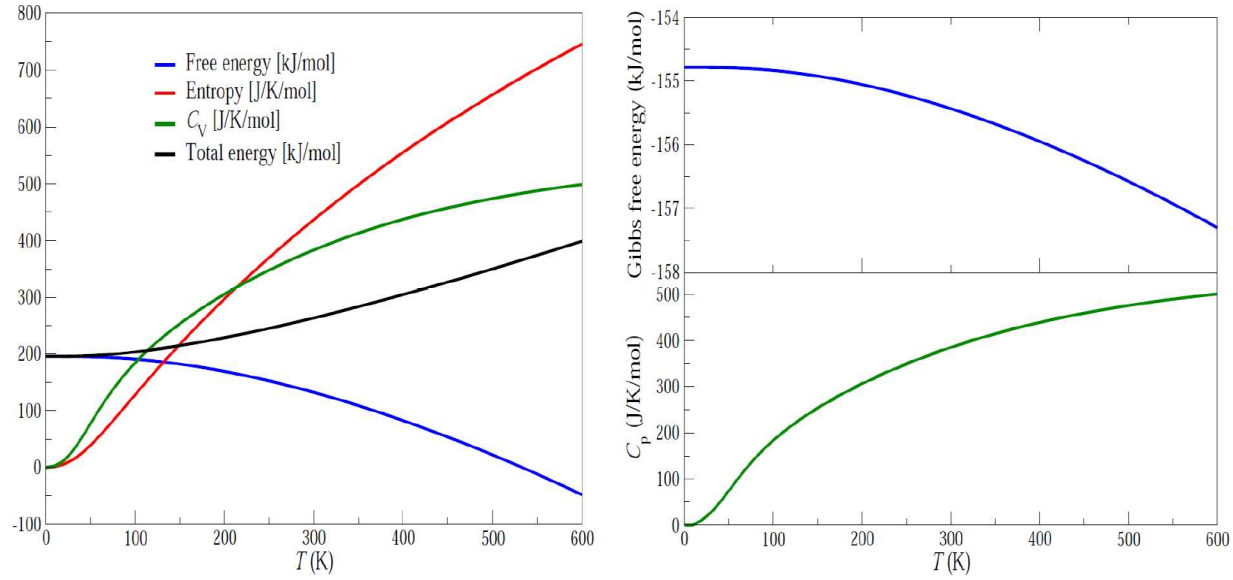

Figure 19. Thermal properties of $CaSO_4$ calculated at the DFT/PBE level of theory. *Left*: thermal properties at constant equilibrium volume. *Right*: Thermal properties at constant pressure.

Thermal Properties of Polyhalite, $K_2Ca_2Mg(SO_4)_4 \bullet 2(H_2O)$

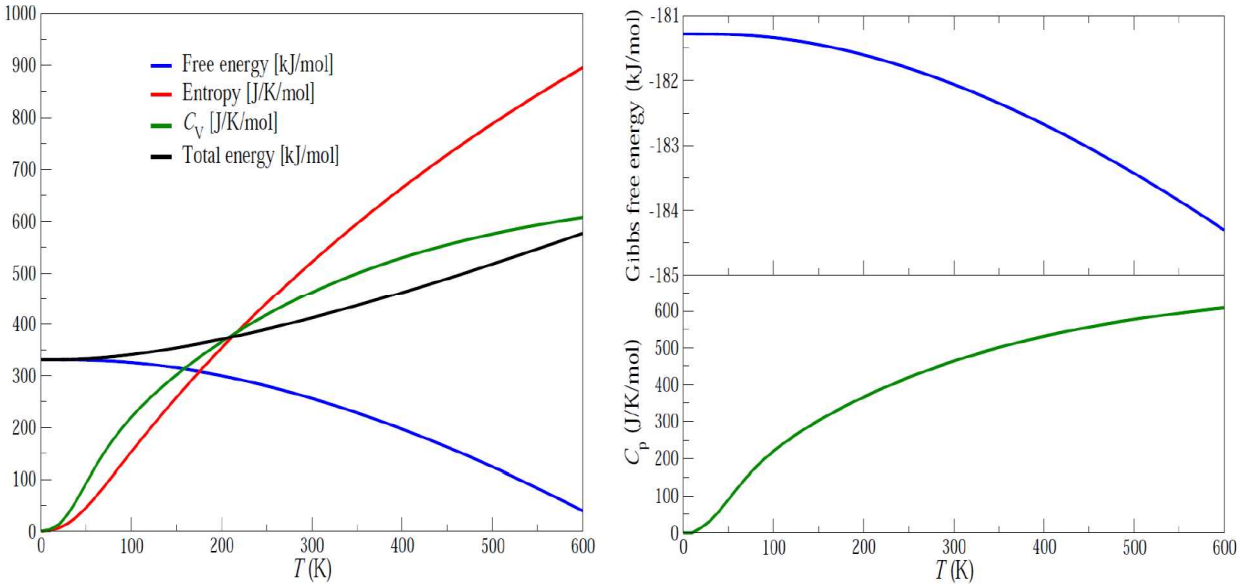

Figure 20. Thermal properties of $K_2Ca_2Mg(SO_4)_4 \bullet 2(H_2O)$ calculated at the DFT/PBE level of theory. *Left*: thermal properties at constant equilibrium volume. *Right*: Thermal properties at constant pressure.

1.3 Conclusions

Density functional theory calculations of the structures and electronic properties of bischofite ($MgCl_2 \bullet 6H_2O$), dehydrated bischofite ($MgCl_2 \bullet 4H_2O$, $MgCl_2 \bullet 2H_2O$ and $MgCl_2 \bullet H_2O$), anhydrite ($CaSO_4$), polyhalite ($K_2Ca_2Mg(SO_4)_4 \bullet 2(H_2O)$) and carnallite ($KMgCl_3 \bullet 6(H_2O)$) were performed within the generalized gradient approximation (GGA). The relaxed structures are found to be in overall good agreement with experimental XRD data, with some slight overestimation, by a few percent, of the computed equilibrium volume compared to experimental estimates. The total and partial densities of states (DOS) and energy band gaps separating the top of the valence band from the bottom of the conduction band were also calculated and analyzed in order to assess the electronic properties and relative stability of these complex salts. All the salts are found to be insulators with calculated band gaps in the ca. 5-6 eV range. Thermal properties at constant, equilibrium volume (i.e., the total energy U, the phonon (Helmholtz) free energy F, the entropy S, and the isochoric heat capacity C_v) and at constant pressure (i.e., the Gibbs free energy G and the isobaric heat capacity C_P) were also reported for $MgCl_2 \bullet 6H_2O$, $MgCl_2 \bullet 4H_2O$, $MgCl_2 \bullet 2H_2O$, $MgCl_2 \bullet H_2O$, $CaSO_4$, and $K_2Ca_2Mg(SO_4)_4 \bullet 2(H_2O)$ based on density functional perturbation theory calculations.

2. References

Agron, P. A., and Busing, W. R. (1985). Magnesium Dichloride Hexahydrate, $MgCl_2.6H_2O$, by Neutron Diffraction. *Acta Crystallographica Section C-Crystal Structure Communications, 41*, 8-10.

Bindi, L. (2005). Reinvestigation of the crystal structure of polyhalite, K2Ca2Mg(SO4)4 2H2O. *Acta Crystallographica, Section E, 61*, i135-i136.

Blöchl, P. (1994). Projector Augmented-Wave Method. *Physical Review B, 50*(24), 17953-17979.

Blöchl, P., Jepsen, O., and Andersen, O. (1994). Improved Tetrahedron Method for Brillouin-Zone Integrations. *Physical Review B, 49*(23), 16223-16233.

Davidson, E. R. (1983). In G. Diercksen, and S. Wilson (Eds.), *Methods in Computational Molecular Physics* (Vol. 113, p. 95). New York, NY: NATO Advanced Study Institute, Series C, Plenum.

Emons, H., and Fanghaenel, T. (1989). Thermal Decomposition of Carnallite (KCl.MgCl2.6H2O) - Comparisom of Experimental Results and Phase Equilibria. *Journal of Thermal Analysis, 35*, 2161-2167.

Grinberg, I., Ramer, N., and Rappe, A. (2001). Quantitative criteria for transferable pseudopotentials in density functional theory. *Physical Review B, 63*(20), 201102.

Hawthorne, F. C., and Ferguson, R. B. (1975). Anhydrous Sulphates. II. Refinement of the Crystal Structure of Anhydrite. Canadian Mineralogist, 13, 289-292.

Kohn, W., Meir, Y., and Makarov, D. E. (1998). van der Waals Energies in Density Functional Theory. *Physical Review Letters, 80*(19), 4153-4156.

Kresse, G., and Furthmüller, J. (1996). Efficient iterative schemes for ab initio total-energy calculations using a plane-wave basis set. *Physical Review B, 54*(16), 11169-11186.

Kresse, G., and Joubert, D. (1999). From ultrasoft pseudopotentials to the projector augmented-wave method. *Physical Review B, 59*(3), 1758-1775.

Molecke, M. (1986a). *Memo of Record: Early Failure of Heaters in WIPP MIIT Brine Equilibration Hole.* Document WP02276, Albuquerque: Sandia National Laboratories.

Molecke, M. (1986b). *Memo of Record: Measurement of Hydrochloric Acid Vapors in WIPP from In Situ Experiments-Safety Aspects.* Document WP03146, Albuquerque: Sandia National Laboratories.

Monkhorst, H., and Pack, J. (1976). Special Points for Brillouin-Zone Integrations. *Physical Review B, 13*(12), 5188-5192.

Perdew, J., Chevary, J., Vosko, S., Jackson, K., Pederson, M., Singh, D., et al. (1992). Atoms, Molecules, Solids, and Surfaces - Applications of the Generalized Gradient Approximation for Exchange and Correlation. *Physical Review B, 46*(11), 6671-6687.

Perdew, J. P., Burke, K., and Ernzerhof, M. (1996). Generalized gradient approximation made simple. *Physical Review Letters, 77*, 3865-3868.

Schlemper, E. O., Sen Gupta, P. K., and Zoltai, T. (1985). Refinement of the structure of carnallite, $Mg(H_2O)_6KCl_3$. *American Mineralogist, 70*, 1309-1313.

Schmidt, H., Hennings, E., and Voigt, W. (2012). Magnesium chloride tetrahydrate, $MgCl_2$ $4H_2O$. *Acta Crystallographica Section C Crystal Structure Communications, C68*, i4-i6.

Sugimoto, K., Dinnebier, R. E., and Hanson, J. C. (2007). Structures of three dehydration products of bischofite from in situ synchrotron powder diffraction data ($MgCl_2$ nH_2O; n = 1, 2, 4). *Acta Crystallographica Section B Structural Science, B63*, 235-242.

Coupled Thermal-Mechanical Modeling of Salt (Part III)

1. Coupled Thermal-Mechanical Modeling

The numerical model used in this work is essentially identical to the one described in Part VI of Jové-Colón et al. (2012). The results presented in this section extend the earlier work to higher heat loads which correspond to varying times of interim surface storage of the heat-generating waste. Thermal-mechanical analyses described in this chapter were carried out using Sandia National Laboratories developed modeling codes. Sierra/Arpeggio, an interface controller, effectively couples the thermal code Sierra/Aria (Notz et al, 2007) and the mechanics code Sierra/Adagio (Spencer et al., 2011) by controlling the transfer of data between the codes and the solution time stepping in the TM simulation. Sierra/Aria is a Galerkin finite element based code capable of treating coupled thermal-hydraulic single and two-phase flow in porous media. Sierra/Adagio is a Galerkin based finite element mechanical code which solves the equations of linear momentum for quasi-static conditions. Sierra/Adagio interfaces with the LAME library of constitutive models (Scherzinger and Hammerand, 2007) which includes a constitutive model suitable for modeling crushed and intact salt behavior.

Sierra/Arpeggio handles the transfer of the temperature field computed in Sierra/Aria to the Sierra/Adagio code. Following the Sierra/Adagio solution the mesh displacements are passed to back to Sierra/Aria for updating the computational grid. The deformations computed by Sierra/Adagio can be used in Sierra/Aria to compute an updated porosity field. The thermal conductivity of the crushed salt is updated based on this porosity and used in the next time step for the thermal solution. The mass and energy conservation equations in Sierra/Aria have been formulated to account for the mesh deformations provided by the Sierra/Adagio solution. These code-to-code transfers are illustrated in Figure 1.

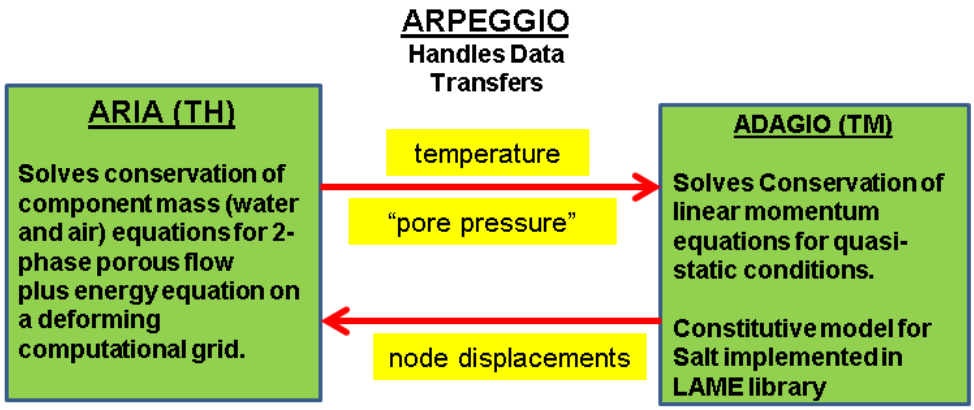

Figure 1. Sierra TM code data transfers

1.1 Geometry/Finite Element Discretization

For these TM analyses, an interior portion of a generic salt repository was modeled with a 2.7 m (9 ft) long, 0.61 m (2 ft) diameter waste canister (red circle in Figure 2) in a 6.4 m (21 ft) long,

3.35 m (11 ft) wide, 3.05 m (10 ft) tall alcove. It was assumed that the alcove connects at right angle to a 3.05 m (10 ft) tall, 3.35 m (11 ft) wide access drift (AD in Figure 2) and it is 12.2 m (40 ft) from the center of the waste canister to a neighboring waste canister. The alcove and access drift were assumed to be filled with 33% porosity run-of-mine salt and surrounded by a 2 m excavation damage zone (EDZ). The EDZ region was included for representing a region of enhanced permeability when hydrogeologic effects are included in future studies. The remainder of the modeled region consists of intact salt. Symmetry conditions for displacement and conduction were used for the four vertical sides of the model so that the modeled domain represented an alcove within the interior of the repository.

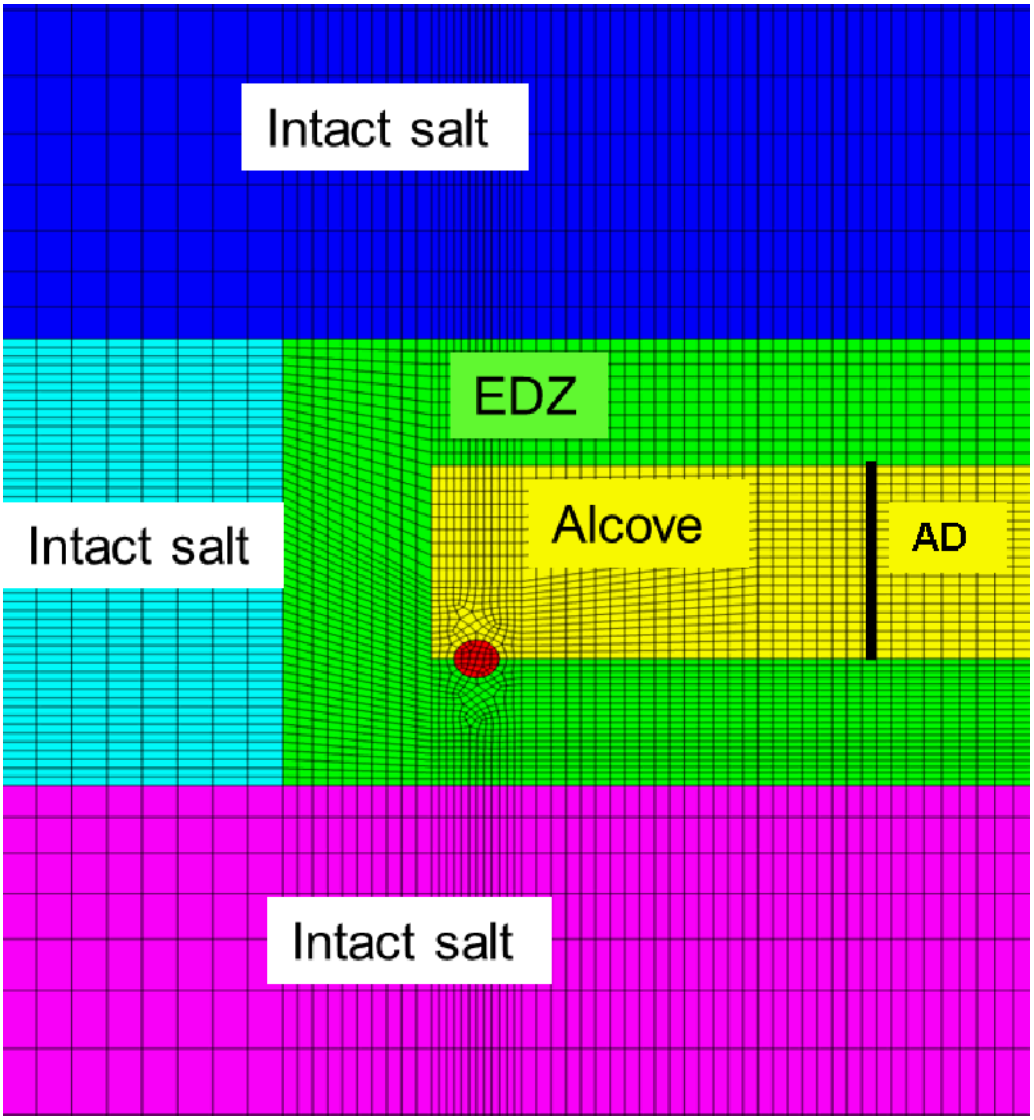

Figure 2. Generalized discretization of modeled geometry.

The finite element grid was constructed using 3-D hexagonal elements. A view of the three dimensional finite element mesh used in both the thermal and mechanical models is shown below in Figure 3. The grid was extended 30.5m (100 ft) above and below the alcove so that the alcove response would not be greatly affected by the boundary conditions during the 10 year simulation period. This time period is sufficient for the crushed salt backfill porosity to be reduced from an initial value of 33% to less than 5% except in the dry backfill case.

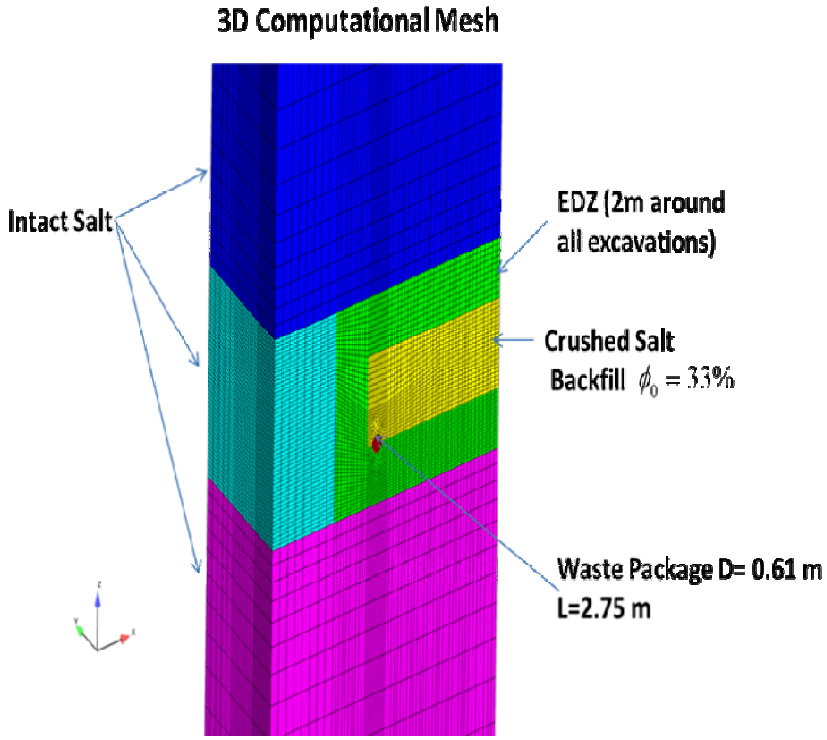

Figure 3. 3D view finite element mesh.

1.3 Thermal Model Description

For the thermal analysis, a convective boundary condition was applied to the top and bottom of the model to simulate the heat transfer into the host rock above and below the repository. To assess this choice of boundary conditions a simulation was performed with no-heat flow conditions on the top and bottom surfaces. No significant difference in the alcove closure rate was observed between these calculations for the 10 year period. All the materials are assumed to be initially at 300K.

Earlier modeling r - . (2012) concentrated on a single heat loading corresponding to approximately 57 years of storage. In this work, we consider various heat loadings corresponding from 10 to 90 years of surface storage before emplacement. Figure 4 shows the power curves for the 10 to 50 year surface storage times. The 0 year heat load curve

was obtained from Clayton and Gable (2009) for glass waste while the curves for the others we obtained by simply translating the time axis.

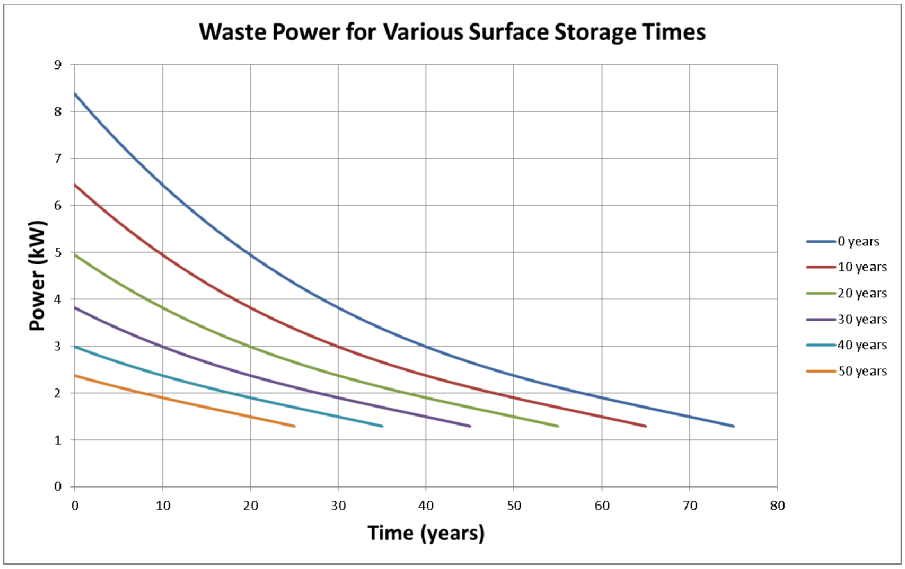

Figure 4. Decay curves used in the thermal analyses.

1.3.1 Constitutive Model for Thermal Conductivity

The temperature dependent thermal conductivity of intact salt used in the analysis is given in the following equation

$$\lambda_{salt}(T) = \lambda_{300}\left(\frac{300}{T}\right)^{\gamma} \qquad (1)$$

where:

λ_{300} = material constant, 5.4 [W/m/K]

γ = material constant, 1.14

T = temperature [K].

The thermal conductivity of the crushed salt used in the analysis is based on the results of the BAMBUS II study (Bechthold et al. 2004) where the thermal conductivity of crushed salt was determined from field experiments on drifts backfilled with crushed salt. From this study, a fourth-order polynomial was fit to the field data to describe crushed-salt thermal conductivity as a function of porosity (ϕ):

$$k_{cs}(\phi) = -270\,\phi^4 + 370\,\phi^3 - 136\,\phi^2 + 1.5\,\phi + 5 \qquad (2)$$

This representation is valid for porosities between zero and forty percent. When the porosity is zero, Equation (2) produces a thermal conductivity of 5.0 W/m/K. Therefore, Equation (2) is modified by a factor (*f*) to correspond with the salt, such that the thermal conductivity of 5.4 W/m/K is reproduced at zero porosity. Equation (2) is rewritten as:

$$k_{cs}(\phi) = \left(-270\,\phi^4 + 370\,\phi^3 - 136\,\phi^2 + 1.5\,\phi + 5\right) \cdot f \qquad (3)$$

where *f* is simply (5.4/5.0 or 1.08). For this study, the initial porosity of the crushed salt is assumed to be 33 percent. The temperature-dependent nature of the crushed-salt thermal conductivity is assumed to be the same as for intact salt. Therefore, the crushed-salt thermal conductivity is given by:

$$\lambda_{c-salt}(T) = k_{cs}(\phi)\left(\frac{300}{T}\right)^{\gamma} \qquad (4)$$

Figure 5 illustrates the dependence of thermal conductivity on temperature and porosity. This model for thermal conductivity of crushed salt has been incorporated in Sierra/Aria through a user module.

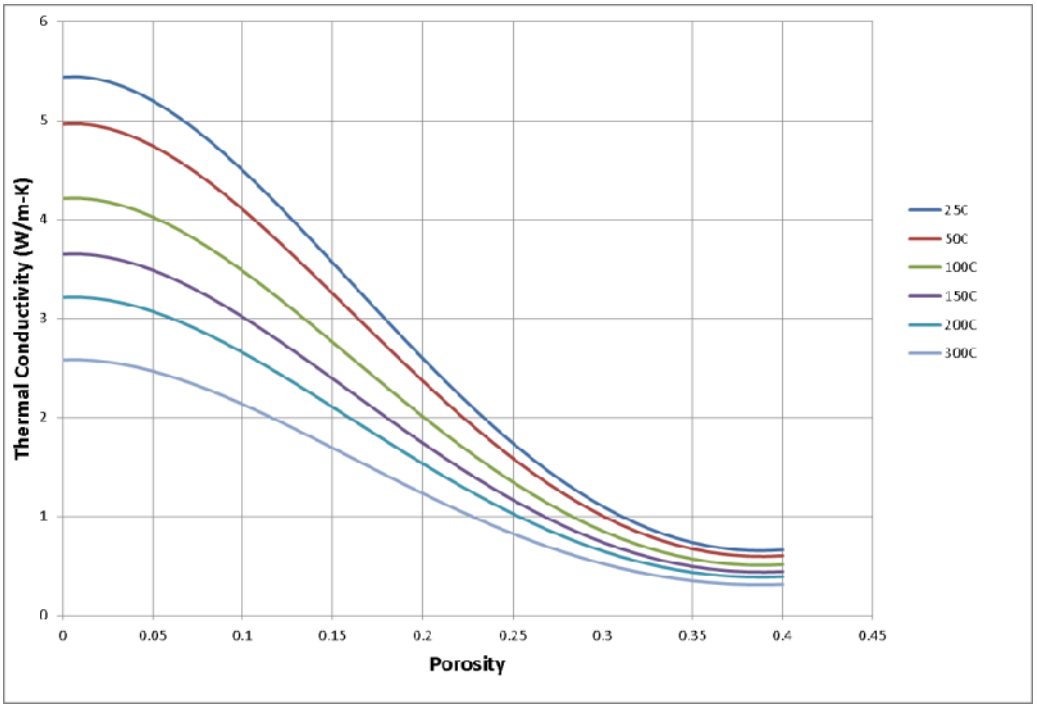

Figure 5. Salt thermal conductivity relationship used in analysis.

The density of the crushed salt was calculated as a linear function of porosity. A summary of the thermal material properties assumed for the waste, intact and EDZ salt and crushed salt are shown in Table 1.

Table 1. Thermal properties for the waste and salt

Material	Thermal Conductivity (W/m-K)	Specific Heat (J/kg-K)	Density (kg/m^3)
Waste (glass)	1.0	840	2,220
Intact and EDZ Salt	Equation **DisplayText can**	931	2,160 ($=\rho_0$)
Crushed Salt	Equation **DisplayText can**	931	$\rho_0(1-\phi)$

1.3.2 Mechanical Model Description

For the mechanical analysis, the boundary conditions were set so that lateral displacements were specified to be zero along the vertical boundaries. No vertical displacement boundary conditions were specified on the bottom surface. The applied mechanical loads acting on the model consisted of an overburden pressure applied to the top of the model to reflect an alcove depth of approximately 600 m. The intact and EDZ salt regions were initialized with lithostatic stresses corresponding to depth, while the waste canister and crushed salt began with no stress. The lithostatic stresses at the level of the alcove were approximately 14.8 MPa. All salt regions were modeled using the crushed salt constitutive model (Callahan 1999) described below. By setting the initial density equal to the intact density the crushed salt model replicates the Multimechanism Deformation model of Munson et al. (1989) for intact salt. The linear thermal expansion coefficient for crushed and host salt material was taken to be $4.5 \times 10^{-5}\ \mathrm{K}^{-1}$.

1.3.2.1 Constitutive Model for Salt

The constitutive model outlined in this section was developed by Callahan (1999) for examining the performance of crushed salt as a component in the shaft and panel seals at the Waste Isolation Pilot Plant (WIPP) near Carlsbad NM. The model has been implemented in the LAME constitutive model library (Scherzinger and Hammerand, 2007) used by the Sierra/Mechanics codes at Sandia National Laboratories.

It is assumed herein that tensile stresses and strain rates are positive. All stress variables in this section should be interpreted as effective stresses. In the crushed salt constitutive model, the total strain rate is additively decomposed into elastic strain rate ($\dot{\varepsilon}_{ij}^{e}$) and inelastic (creep) strain rate ($\dot{\varepsilon}_{ij}^{c}$) contributions

$$\dot{\varepsilon}_{ij} = \dot{\varepsilon}_{ij}^{e} + \dot{\varepsilon}_{ij}^{c} \qquad (5)$$

The elastic strain rate may be decomposed into deviatoric ($\dot{e}_{ij}^{e}$) and volumetric ($\dot{\varepsilon}_{kk}^{e}$) contributions

$$\dot{\varepsilon}_{ij}^{e} = \dot{e}_{ij}^{e} + \frac{1}{3}\dot{\varepsilon}_{kk}^{e}\delta_{ij} \qquad (6)$$

In this model the Cauchy stress rate ($\dot{\sigma}_{ij}$) is related to the elastic strain rate by the isotropic hypo-elastic relation by

$$\dot{\sigma}_{ij} = 2G\dot{e}_{ij}^{e} + K\dot{\varepsilon}_{kk}^{e}\delta_{ij} = 2G\left(\dot{e}_{ij} - \dot{e}_{ij}^{c}\right) + K\left(\dot{\varepsilon}_{kk} - \dot{\varepsilon}_{kk}^{c}\right)\delta_{ij} \qquad (7)$$

where G and K are the shear and bulk moduli respectively. Following the work of Sjaardema and Krieg (1987) these moduli are assumed to be non-linear functions of the material density (ρ). No temperature dependency is included in the functional form of the elastic moduli. The functional forms for these elastic moduli are

$$\begin{aligned} G &= G_0 e^{G_1\rho} \\ K &= K_0 e^{K_1\rho} \end{aligned} \qquad (8)$$

where G_0, G_1, K_0, and K_1 are constants determined from laboratory testing.

The total creep strain rate ($\dot{\varepsilon}_{ij}^{c}$) contains contributions from two time-dependent inelastic mechanisms – dislocation creep ($\dot{\varepsilon}_{ij}^{d}$) and grain boundary diffusional pressure solution ($\dot{\varepsilon}_{ij}^{w}$).

$$\dot{\varepsilon}_{ij}^{c} = \dot{\varepsilon}_{ij}^{d} + \dot{\varepsilon}_{ij}^{w} \qquad (9)$$

$$\dot{\varepsilon}_{ij}^{d} = \left[\dot{\varepsilon}_{eq}^{d}\left(\sigma_{eq}^{f}\right)\right]\frac{\partial\sigma_{eq}}{\partial\sigma_{ij}} \qquad (10)$$

$$\dot{\varepsilon}_{ij}^{w} = \left[\dot{\varepsilon}_{eq}^{w}\left(\sigma_{eq}^{f}\right)\right]\frac{\partial\sigma_{eq}}{\partial\sigma_{ij}} \qquad (11)$$

When a deviatoric stress is applied to a crystalline material (e.g. salt) it causes dislocations in the lattice to move resulting in inelastic macroscopic deformations. The second creep mechanism, grain boundary diffusional pressure solution, results from the migration of salt through the liquid phase and is developed from grain to grain contacts resulting in dissolution at the contact and precipitation in adjacent pores. The driving force for pressure solution is the gradient of the chemical potential induced by differences in contact stresses.

The terms in brackets in Equations (10) and (11) are the kinetic equations for dislocation creep ($\dot{\varepsilon}_{eq}^{d}$) and grain boundary diffusional pressure solution ($\dot{\varepsilon}_{eq}^{w}$). The notation used in Equations (10) and (11)indicates these equivalent creep strain rates are scalar functions of the equivalent stress measure (σ_{eq}^{f}), defined below in Equation (12). The creep flow potential used in the model is defined using a different equivalent stress measure (σ_{eq}). This non-associative formulation was introduced to control dilatancy which occurs as a result of including the mean stress term in the model. The partial derivatives $\frac{\partial\sigma_{eq}}{\partial\sigma_{ij}}$ appearing in Equations (10) and (11) are the components of the gradient of the creep flow potential.

The two equivalent stress measures are given by

$$\sigma_{eq}^{f} = \left[\eta_0 \Omega_f^{\eta_1} \sigma_m^2 + \left(\frac{2-D}{D} \right)^{\frac{2n_f}{n_f+1}} \left(\sigma_1 - \sigma_3 \right)^2 \right]^{1/2} \qquad (12)$$

$$\sigma_{eq} = \left[\kappa_0 \Omega^{\kappa_1} \sigma_m^2 + \left(\frac{2-D}{D} \right)^{\frac{2n}{n+1}} \left(\sigma_1 - \sigma_3 \right)^2 \right]^{1/2} \qquad (13)$$

where

$$\Omega_f = \left[\frac{\left(1-D\right) n_f}{\left[1 - \left(1-D\right)^{1/n_f} \right]^{n_f}} \right]^{\frac{2}{n_f+1}} \qquad (14)$$

$$\Omega = \left[\frac{\left(1-D_v\right) n}{\left[1 - \left(1-D_v\right)^{1/n} \right]^{n}} \right]^{\frac{2}{n+1}} \qquad (15)$$

and

$$D_v = \begin{cases} D_t & D \le D_t \\ D & D > D_t \end{cases} \qquad (16)$$

where:

D= fractional density = $\dfrac{\rho}{\rho_{\text{int}}}$

ρ = current density

ρ_{int} = intact salt density

σ_{m} = mean stress = $\dfrac{1}{3}\sigma_{kk}$

σ_1 = maximum principal stress

σ_3 = minimum principal stress

$\eta_0, \eta_1, \kappa_0, \kappa_1, n_f, n, D_t$ = material parameters.

As the crushed salt approaches full consolidation ($D \rightarrow 1$) Ω_f and Ω both approach zero and the mean stress influence on the creep strain rate is eliminated. This is consistent with observed deformation

isochoric (constant volume) deformation characteristics of intact salt. When the salt is fully consolidated, $D = 1$, Equations (12) and (13) reduce to

$$\sigma_{eq}^{f} = \sigma_{eq} = \sigma_1 - \sigma_3 \qquad (17)$$

The quantity $\sigma_1 - \sigma_3$ is equal to the Tresca equivalent stress (σ_{eq}^{T})

$$\sigma_1 - \sigma_3 = \sigma_{eq}^{T} = 2\cos\psi\sqrt{J_2} \qquad (18)$$

where ψ is the Lode angle and J_2 is the second invariant of the deviatoric stress tensor defined by Equations (19) and (20), respectively. The Lode angle is dependent on both the second (J_2) and third invariant (J_3) of the deviatoric stress tensor.

$$\psi = \frac{1}{3}\sin^{-1}\left[\frac{-3\sqrt{3}J_3}{2J_2^{3/2}}\right] \qquad -\frac{\pi}{6} \le \psi \le \frac{\pi}{6} \qquad (19)$$

$$J_2 = \frac{1}{2}s_{ij}s_{ji} \qquad (20)$$

$$J_3 = \frac{1}{3}s_{ij}s_{jk}s_{ki} \qquad (21)$$

The gradient of the flow potential may be written

$$\frac{\partial\sigma_{eq}}{\partial\sigma_{ij}} = \frac{\partial\sigma_{eq}}{\partial\sigma_m}\frac{\partial\sigma_m}{\partial\sigma_{ij}} + \frac{\partial\sigma_{eq}}{\partial J_2}\frac{\partial J_2}{\partial\sigma_{ij}} + \frac{\partial\sigma_{eq}}{\partial J_3}\frac{\partial J_3}{\partial\sigma_{ij}} \qquad (22)$$

The partial derivatives of the three stress invariants ($\sigma_m, J_2,$ and J_3) with respect to the Cauchy stresses are given by

$$\frac{\partial\sigma_m}{\partial\sigma_{ij}} = \frac{\delta_{ij}}{3} \qquad (23)$$

$$\frac{\partial J_2}{\partial\sigma_{ij}} = s_{ij} \qquad (24)$$

$$\frac{\partial J_3}{\partial \sigma_{ij}} = t_{ij} = s_{ik}s_{kj} - \frac{2}{3}J_2\delta_{ij} \qquad (25)$$

The partial derivatives of the equivalent stress with respect to the stress invariants are given by

$$\frac{\partial \sigma_{eq}}{\partial \sigma_m} = \frac{\kappa_0 \Omega^{\kappa_1}\sigma_m}{\sigma_{eq}} \qquad (26)$$

$$\frac{\partial \sigma_{eq}}{\partial J_2} = \frac{2}{\sigma_{eq}}\left(\frac{2-D}{D}\right)^{\frac{2n}{n+1}} \frac{\cos\psi \cos 2\psi}{\cos 3\psi} \qquad (27)$$

$$\frac{\partial \sigma_{eq}}{\partial J_3} = \frac{\partial \sigma_{eq}}{\partial \psi}\frac{\partial \psi}{\partial J_3} \qquad (28)$$

where

$$\frac{\partial \sigma_{eq}}{\partial \psi} = -\frac{4}{\sigma_{eq}}\left(\frac{2-D}{D}\right)^{\frac{2n}{n+1}} \cos\psi \sin\psi J_2 \qquad (29)$$

$$\frac{\partial \psi}{\partial J_3} = -\frac{\sqrt{3}}{2J_2^{3/2}\cos 3\psi} \qquad (30)$$

Making these substitutions in Equation (10) gives the following result

$$\dot{\varepsilon}_{ij}^{c} = \frac{\dot{\varepsilon}_{eq}^{d} + \dot{\varepsilon}_{eq}^{w}}{\sigma_{eq}}\left\{\frac{\kappa_0 \Omega^{k_1}\sigma_m}{3}\delta_{ij} + \left(\frac{2-D}{D}\right)^{\frac{2n}{n+1}} 2\sqrt{J_2}\cos\psi\left(\left[\frac{\cos 2\psi}{\cos 3\psi}\right]\frac{s_{ij}}{\sqrt{J_2}} + \left[\frac{\sqrt{3}\sin\psi}{J_2\cos 3\psi}\right]t_{ij}\right)\right\} \qquad (31)$$

At stress states where $\psi = \pm\frac{\pi}{6}$ the gradient is not uniquely defined. This is due to the presence of corners in the flow potential; therefore, special consideration must be given to the gradient computation at these locations. To complete the description of the creep strain rate, the kinetic equations (i.e. equivalent creep strain rate equations) for dislocation ($\dot{\varepsilon}_{eq}^{d}$) and grain boundary diffusional pressure solution ($\dot{\varepsilon}_{eq}^{w}$) need to be defined.

The dislocation creep model, known as the Multimechanism Deformation model (MD model) developed by Munson and Dawson (1979) and extended by Munson et al. (1989), provides the dislocation creep component of the crushed salt model. Recall that as the crushed salt approaches the density of intact salt the two stress measures are identical; therefore, the crushed salt model transitions in a logical manner to the MD model as the fractional density approaches a value of one.

The kinetic equation for dislocation creep in the MD model is given by Equation **Error! Reference source not found.**(0.32) where F is a function which accounts for transient creep effects and $\dot{\varepsilon}_s$ is the steady state dislocation creep strain rate.

$$\dot{\varepsilon}_{eq}^{d} = F\dot{\varepsilon}_s \qquad (32)$$

The transient function F has three branches: a work hardening branch ($F > 1$), an equilibrium branch ($F = 1$), and a recovery branch ($F < 1$).

$$F = \begin{cases} \exp\left[\Delta\left(1-\dfrac{\zeta}{\varepsilon_t^f}\right)^2\right] & \zeta < \varepsilon_t^f \quad \text{Transient Branch} \\ 1 & \zeta = \varepsilon_t^f \quad \text{Equilibrium Branch} \\ \exp\left[-\delta\left(1-\dfrac{\zeta}{\varepsilon_t^f}\right)^2\right] & \zeta > \varepsilon_t^f \quad \text{Recovery Branch} \end{cases} \qquad (33)$$

The choice of the particular branch depends on the transient strain limit (ε_t^f) and the internal variable (ζ). The transient strain limit is defined by Equation (34) where K_0, c, and m are material parameters, T is the absolute temperature, and μ is the shear modulus of intact salt.

$$\varepsilon_t^f = K_0 e^{cT}\left(\frac{\sigma_{eq}^f}{\mu}\right)^m \qquad (34)$$

The internal variable ζ, used in the calculation of the transient function F, is obtained by integration of the evolution equation

$$\dot{\zeta} = (F-1)\dot{\varepsilon}_s \qquad (35)$$

Δ and δ, appearing in Equation (33), are the work hardening and recovery parameters and are given by Equations (36)and (37) respectively. In these equations α, β, α_r, and β_r are material parameters. In the crushed salt model the recovery parameter δ is taken to be constant (i.e. $\delta = \alpha_r$) because of insufficient data.

$$\Delta = \alpha + \beta \log\left(\frac{\sigma_{eq}^f}{\mu}\right) \qquad (36)$$

$$\delta = \alpha_r + \beta_r \log\left(\frac{\sigma_{eq}^f}{\mu}\right) \qquad (37)$$

In the MD model, three steady state dislocation mechanisms are considered: dislocation climb ($\dot{\varepsilon}_{s_1}$), an unidentified but experimentally observed mechanism ($\dot{\varepsilon}_{s_2}$), and dislocation slip ($\dot{\varepsilon}_{s_3}$). Because these mechanisms are assumed to act in parallel, their contribution to the steady state dislocation creep strain rate is simply the sum of the three.

$$\dot{\varepsilon}_s = \sum_{i=1}^{3} \dot{\varepsilon}_{s_i} \qquad (38)$$

$$\dot{\varepsilon}_{s_1} = A_1 \left(\frac{\sigma_{eq}^f}{\mu} \right)^{n_1} \exp\left(-\frac{Q_1}{RT} \right) \qquad (39)$$

$$\dot{\varepsilon}_{s_2} = A_2 \left(\frac{\sigma_{eq}^f}{\mu} \right)^{n_2} \exp\left(-\frac{Q_2}{RT} \right) \qquad (40)$$

$$\dot{\varepsilon}_{s_3} = \left(B_1 e^{-Q_1/RT} + B_2 e^{-Q_2/RT} \right) \sinh\left[q \left(\frac{\sigma_{eq}^f - \sigma_0}{\mu} \right) \right] H\left(\sigma_{eq}^f - \sigma_0 \right) \qquad (41)$$

where:

A_1, A_2, B_1, B_2 are structure factors

Q_1, Q_2 are activation energies

R is the universal gas constant

T is the temperature (K)

q is the stress constant

σ_0 is the stress limit above which dislocation slip become active

H is the Heaviside function = 1 when $\sigma_{eq}^f - \sigma_0 > 0$ otherwise =0.

The first mechanism (dislocation climb) dominates at low equivalent stress (σ_{eq}^f) and high temperature. The second mechanism (unidentified or unnamed) dominates at low stress and temperature. The third mechanism (dislocation slip) is predominately active at high stress for all temperatures. The kinetic equation for grain boundary diffusional pressure solution, used in the WIPP crushed salt model, is a modified version of the Spiers and Brzesowsky (1993) model for wet crushed salt.

$$\dot{\varepsilon}_{eq}^w = \frac{r_1 w^a}{d^p} e^{-\bar{\varepsilon}_v} \left(\frac{e^{r_3 \bar{\varepsilon}_v}}{\left| e^{\bar{\varepsilon}_v} - 1 \right|^{r_4}} \right) \frac{e^{-\frac{Q_s}{RT}}}{T} \Gamma \sigma_{eq}^f \qquad (42)$$

where:

r_1, r_3, r_4, Q_s, a, p are material constants

T is temperature (K)

R is the universal gas constant

d stands for grain size

w is the moisture fraction by weight

$\bar{\varepsilon}_v$ corresponds to the true or natural volumetric strain

Γ is a geometry function

Note that if the crushed salt is dry ($w = 0$), the grain boundary diffusional pressure solution contribution to the total strain rate vanishes (i.e. $\dot{\varepsilon}_{eq}^{w} = 0$) and grain size has no influence in the model. In Equation (42), the term $e^{\bar{\varepsilon}_v} - 1$ appears in the denominator. An initial volumetric strain ε_{v*}, corresponding to the volumetric strain accumulated in going from a fractional density $D_0 = 0.64$ to the fractional density at the time the crushed salt is placed is included in Equation (42) to avoid division by zero when the volume strain at the start of the simulation is zero.

The geometry function Γ used in Equation (42) has two functional forms given by Equation (43); the choice of which one to use depends on the magnitude of the engineering volumetric strain e_v. For compressive volumetric strains less than 15% a constant value of one is used.

$$\Gamma = \begin{cases} 1 & \text{small strain } (e_v > -0.15) \\ \left[\dfrac{e^{\bar{\varepsilon}_v} + \phi_0 - 1}{\phi_0 e^{\bar{\varepsilon}_v}} \right]^{n_s} & \text{large strain } (e_v < -0.15) \end{cases} \qquad (43)$$

where n_5 is a material constant.

As the crushed salt density approaches the density of intact salt the value of Γ approaches zero; therefore, $\dot{\varepsilon}_{eq}^{w} = 0$ when the salt is fully consolidated. Table 2 lists the parameter values used in these simulations. The waste was assumed to respond elastically using the properties of steel shown in Table 3.

Table 3. Mechanical Properties used for salt

Symbol	Crushed Salt	Intact and EDZ Salt	Units
G_0	1.06×10^4	1.24×10^{10}	Pa
G_1	0.00653	0.0	m^3/kg
K_0	1.76×10^4	2.07×10^{10}	Pa
K_1	0.00653	0.0	m^3/kg
ρ_*	1447 for initial porosity = 33%	2160.	kg/m^3
ρ_{int}	2160.	2160.	kg/m^3
μ	1.24×10^{10}	1.24×10^{10}	Pa
A_1	8.386×10^{22}	8.386×10^{22}	1/s
Q_1/R	12580	12580	K
n_1	5.5	5.5	-
B_1	6.086×10^6	6.086×10^6	1/s
A_2	9.672×10^{12}	9.672×10^{12}	1/s
Q_2/R	5032	5032	K
n_2	5.0	5.0	-
B_2	3.034×10^{-2}	3.034×10^{-2}	1/s
σ_0	20.57×10^6	20.57×10^6	Pa
q	5335.	5335.	-
m	3.0	3.0	-
K_0	6.275×10^5	6.275×10^5	-
c	9.198×10^{-3}	9.198×10^{-3}	1/K
α	-17.37	-17.37	-
β	-7.738	-7.738	-
δ	0.58	0.58	-

Table 2. Mechanical Properties used for salt (Cont.)

Symbol	Crushed Salt	Intact and EDZ Salt	Units
κ_0	10.119	10.119	-
κ_1	1.005	1.005	-
n	1.331	1.331	-
D_t	0.896	0.896	-
η_0	0.1029	0.1029	-
η_1	3.9387	3.9387	-
n_f	3.5122	3.5122	-
a	0.3147	0.3147	-
p	1.6332	1.6332	-
n_s	0.5576	0.5576	-
Q_s/R	1077.46	1077.46	K
r_1	1.041×10^{-12}	1.041×10^{-12}	$m^p \cdot K/(Pa \cdot s)$
r_3	15.1281	15.1281	-
r_4	0.1678	0.1678	-
w	0, 1%	0.0	-
d	0.001	0.001	m

Table 4. Mechanical properties used for the waste.

Material	Young's Modulus (Pa)	Poisson's Ratio	Thermal Expansion (K^{-1})
waste canister	2.0E11	0.3	2.0E-6

1.3.2.2 Coupled Mechanical and Thermal Analysis Results

The finite element discretization shown in Figure and 3 was used in the coupled thermo-mechanical calculations. The same finite element mesh was used in the thermal and mechanical models though this is not a requirement of the Sierra codes; interpolation from different grids is allowed. The thermal-mechanical simulations performed in this study examine the closure of the backfilled regions and how the closure rate is affected by thermal loading and water content. The salt backfill is compacted due to the inward creep of the host rock. Initially the rate of compaction of the backfilled region depends on the stresses produced in the host rock by the mining of the access drifts and alcoves. Thermal effects become increasingly important as the heat from the waste package is conducted out into the backfill and host rock. The creep rate of the host salt formation is highly dependent on stress and temperature. Ultimately the salt backfill begins to provide resistance to closure as its porosity is reduced and it becomes more highly consolidated. In all cases, the water content in the backfill is assumed to be constant throughout the simulation. If moisture movement were included (e.g. THM model) regions of dry-out near the heater would be expected as well as wetter regions due to moisture transport and water vapor condensation in cooler areas of the backfilled alcove and access drifts.

1.3.3 Mechanical Modeling Results

1.3.3.1 Average Backfill Porosity

The evolution of the crushed salt backfill porosity can be used to provide information about how long it will take for the waste to be encapsulated due to the creep of the host rock. The modeling results in Jové-Colón et al. (2012, Figure 1.6 and 1.7, page 236) showed that the presence of small amounts (1% or less) of water in the crushed salt backfill allowed the intact salt to creep inward at a faster rate because the moist backfill provided less resistance to closure of the host rock compared to the dry backfill case. The end result is that moist crushed salt backfill consolidates faster than if it were dry. This experimentally observed response is reproduced in these simulations by activating the pressure-solution creep mechanism included in the constitutive model for crushed salt.

The work described in this section examines the effect of thermal loading on backfill consolidation for eight thermal loading cases varying from 10 to 90 years of interim storage. Each of these thermal loading cases was evaluated for 0% (dry, Figure 6) and 1% moisture in the backfill (Figure 7). An additional series of calculations were performed varying the thermal properties of the waste from those given in Table 1 for glass (Table 1) to ones representative of metal (e.g. steel). The values used in these supplemental calculations were: thermal conductivity =53 W/m-K, specific heat = 500 J/kg-K and mass density = 7854 kg/m^3. Figure 8 shows the temperature fields computed using the 50 year surface storage heat loading for the glass and metal waste forms. The only discernible temperature field differences are close to the canister where the temperatures greater than 100°C extend slightly further out in the glass waste case. These metal waste case calculations produced lower temperatures in the waste and near canister region due to the larger heat capacity of steel waste compared to the glass waste. While the local temperatures in the numerical model region representing the waste package and the near

canister region were affected by the choice of waste thermal properties, the average porosity histories shown in Figures 6 and 7 were unaffected (the curves overlay for the two cases). The higher temperatures in the glass waste case should convert a greater amount of liquid water to water vapor due to increased evaporation but these effects can only be simulated when the two-phase porous flow equations are included as in the TH or THM coupled simulations described in another section of this report.

Comparison of Figures 6 and 7 illustrates the effect of moisture of the consolidation rate of the backfill as well as the increased consolidation rate for the higher thermal load waste. The simulations using 1% moisture crushed salt backfill combined with surface storage of less than 50 year have essentially reached the porosity of intact salt by 10 years. All of the dry backfill cases and the longer surface storage cases with 1% moisture show that additional time will be required before the backfill is fully consolidated. To reach full consolidation for these cases, the simulations would need to be continued for longer solution periods; however, the computational domain would also need to be extended so that the boundary conditions on the top and bottom of the domain were not overly influencing the solution.

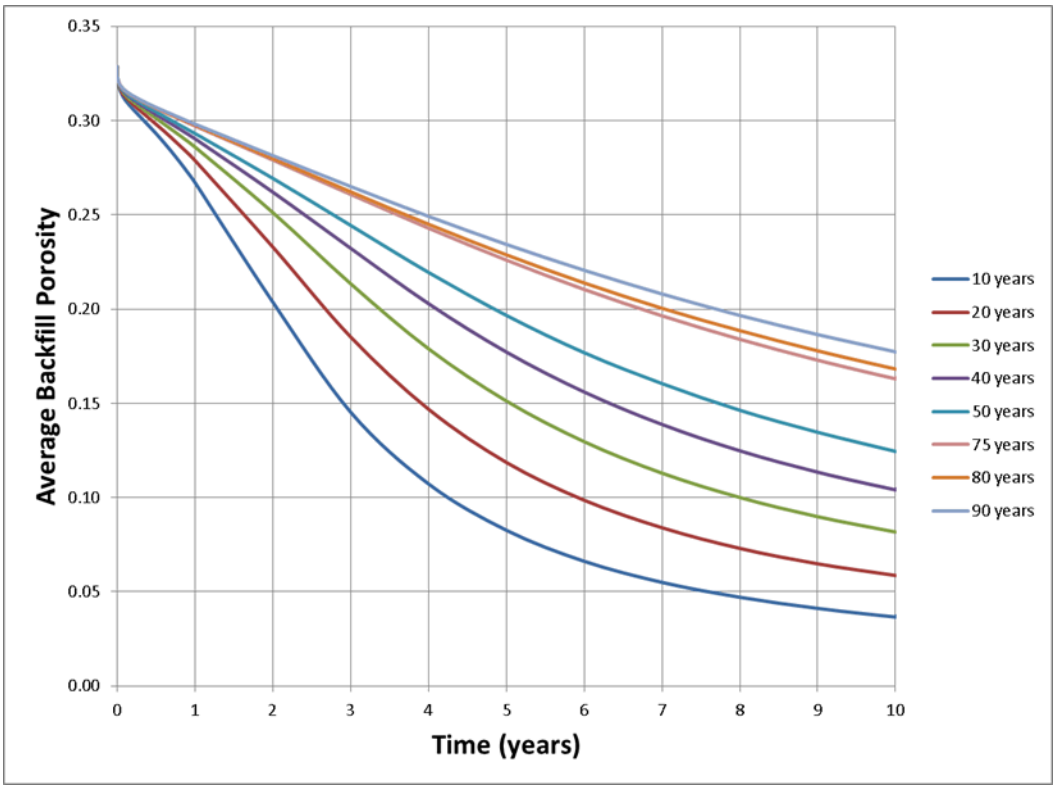

Figure 6. Influence of heat load on the average backfill porosity: dry backfill case

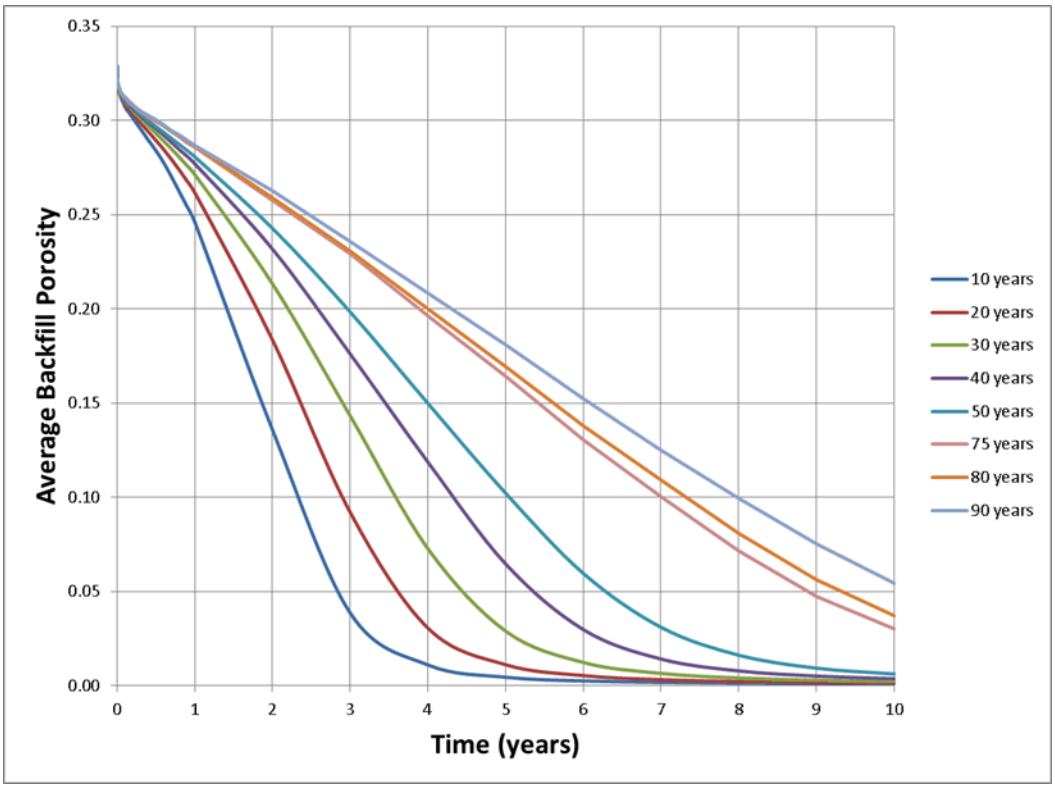

Figure 7. Influence of heat load on the average backfill porosity: 1% moisture in backfill case

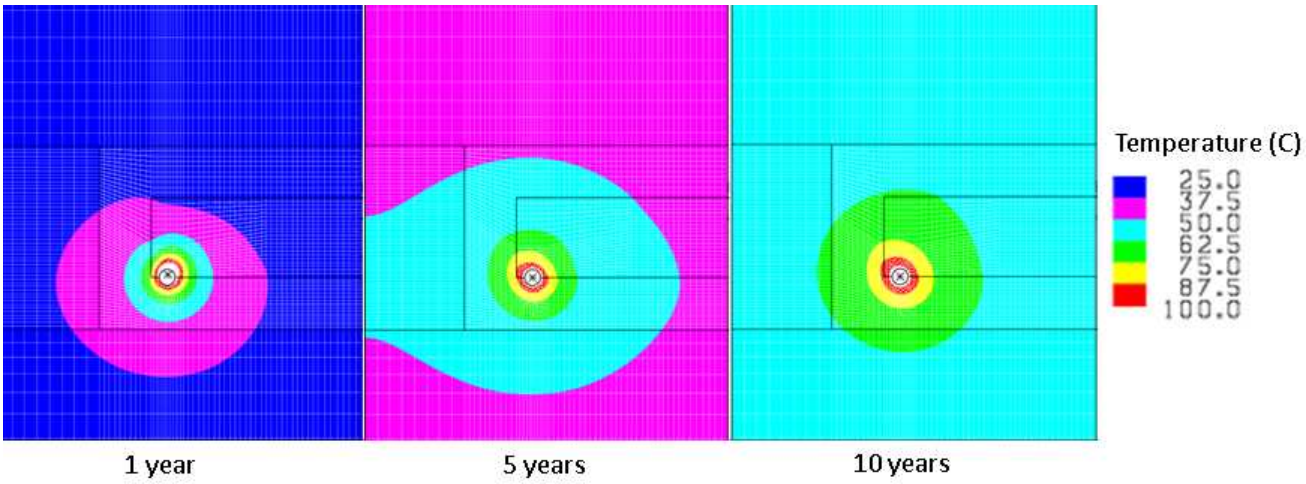

Figure 8a. Temperature field at 1, 5, and 10 years for glass waste. 50 years surface storage case andmoisture content = 1%

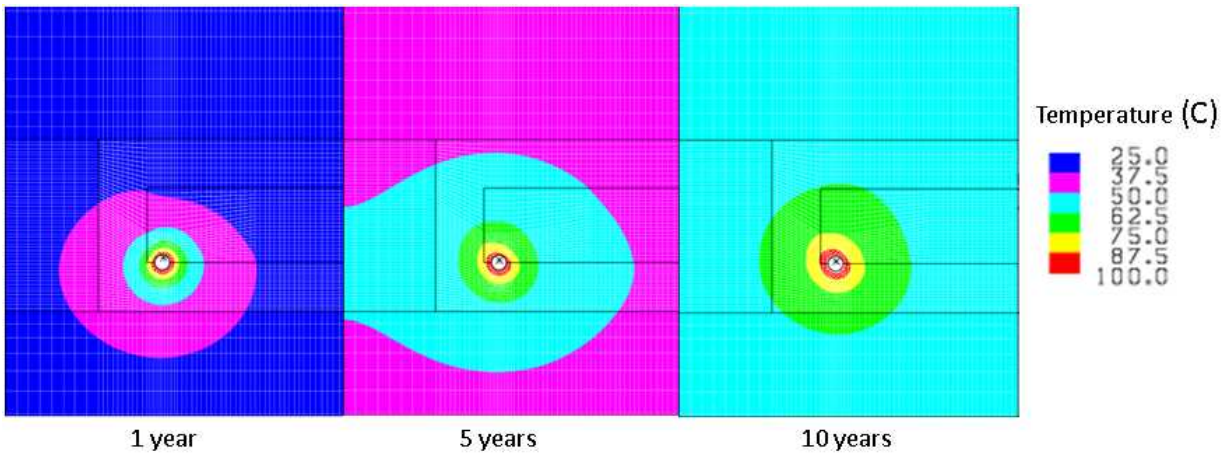

Figure 8b. Temperature field at 1, 5, and 10 years for metal waste. 50 years surface storage case and moisture content = 1%

1.4 Summary and Future Work in Salt Modeling

A series of coupled thermo-mechanical (TM) calculations of a generic salt repository have been completed using the Sandia National Laboratories Sierra codes. These results extend earlier TM modeling presented in Hardin et al. -Colon et al. (2012). Results from these TM analyses provide estimates of the time for the crushed salt backfill to compact to levels approaching intact salt density. Hopefully future calculations will take advantage of the hydrogeologic capability of Sierra/Aria to include fully coupled thermal, hydrological and/or chemical calculations. The inclusion of hydraulic models (e.g. single phase or multi-phase flow) is important because the mechanical behavior is directly influenced by the pore-fluid pressures. The low permeability of the host salt could result in significant pore-fluid pressures being generated. In a coupled THM simulation, in addition to the temperatures, the pore-fluid pressures will be transferred from Sierra/Aria to Sierra/Adagio to evaluate the effective stresses.

The influence of moisture in the crushed salt backfill has a significant impact on the amount of time needed for the salt backfill to approach intact salt density or porosity. It is likely that the water content will be variable throughout the salt backfill following placement of the waste package. Regions near the waste package will be drier and thus slower to consolidate. This effect should be considered in future modeling to understand how strongly it affects the backfill consolidation rate.

The EDZ region in the current model was added in anticipation of including its effect on hydraulic behavior in THM modeling. The constitutive model employed in the current modeling does not account for excavation induced damage on the host salt behavior. The term damage refers to the creation of microcracks in the host rock due to the mining activities. In a laboratory setting the development of microcracks during triaxial testing is observed as dilation in the sample. From a constitutive model view point damage occurs at any point in where the stress state exceeds the "dilatancy boundary". Region of damaged salt would have higher permeability than non-damaged material due to the presence of open microcracks in the salt. Eventually the inward creep of the host rock will compact the backfill and the resulting back stress from the backfill will close or heal the microcracks. Future work should consider the evolution of damage and healing in salt and its coupling with hydraulic modeling through permeability/porosity changes.

2. References

Bechthold, W., E. Smailos, S. Heusermann, W. Bollingerfehr, B. Bazargan Sabet, T. Rothfuchs, P. Kamlot, J. Grupa, S. Olivella, and F.D. Hansen, 2004. Backfilling and Sealing of Underground Repositories for Radioactive Waste in Salt (BAMBUS II Project), Final Report EUR 20621, Nuclear Science and Technology, Luxembourg.

Callahan, G.D. 1999. Crushed Salt Constitutive Model. Sandia National Laboratories, Albuquerque, NM. SAND98-2680.

Clayton, D. J., and Gable, C. W. 2009. 3-D Thermal Analyses of High Level Waste Emplaced in a Generic Salt Repository, SAND2009-0633P, Sandia National Laboratories, Albuquerque, NM.

Hardin, E., D. Clayton, C. Jové-Colón, L. Zheng, J. Rutqvist, J. Houseworth, J. Davis, R. Tinnacher, L. Li, H.H Liu, M. Sutton, A. Tayne and T. Wolery, Repository Science THMC Coupled Processes Investigations FY11, FCRD-USED-1011-000288 Rev.0, Prepared for U.S. Department of Energy Office of Used Fuel Disposition.

Jové-Colón, Carlos F. et al. (2012) Evaluation of Generic EBS Design Concepts and Process Models: Implications to EBS Design Optimization. FCRD-USED-2012-000140, Prepared for the U.S. Department of Energy Used Fuel Disposition Campaign.

Munson, D.E. and Dawson, P.R., SAND79-1853, *Constitutive Model for the Low Temperature Creep of Salt (With Application to WIPP)*, Sandia National Laboratories Albuquerque, NM, 1979.

Munson, D.E., A.F. Fossum and P.E. Senseny. 1989. Advances in Resolution of Discrepancies between Predicted and Measured WIPP In-situ Room Closures. Sandia National Laboratories, Albuquerque, NM. SAND88-2948.

Notz, P. K., S. R. Subia, M. M. Hopkins, H. K. Moffat, and D. Noble. (2007) *Aria 1.5: User Manual,* SAND2007-2734. Albuquerque, NM: Sandia National Laboratories,

Scherzinger, W. M. and D. C. Hammerand. (2007) *Constitutive Models in LAME,* SAND2007-5873. Albuquerque, NM: Sandia National Laboratories.

Spencer, B. W. et al. (2011) *Adagio 4.20 User's Guide*, SAND2011-1825. Albuquerque, NM: Sandia National Laboratories.

Spiers, C.J. and Brzesowsky, R.H., *Densification Behaviour of Wet Granular Salt: Theory vs. Experiment*, Seventh Symposium on Salt, Kyoto, Japan, April 6-9, 1992, Eds. H. Kakihana, H.R. Hardy, Jr., T. Hoshi, and K. Toyokura. Amsterdam; New York: Elsevier. Vol. 1, 83-92, 1993.

Thermal-Hydrologic (TH) and Thermal-Hydrologic-Mechanical (THM) Modeling for Heat Generating Waste Disposal in Salt

(Part VI)

1. Thermal-Hydrologic and Thermal-Hydrologic-Mechanical Modeling

As part of the Thermo-Mechanical (TM), Thermo-Hydrology (TH), and coupled THM modeling in a generic salt repository, three-dimensional simulations were carried out to further understand the thermally driven processes as a result of decaying heat from a waste package or canister. In these simulations heat transfer is by both conduction and convection. This section describes TH simulations carried out to identify the parameters that most influence thermal response in a two-phase system. The section also includes one-way coupled THM modeling with different surface storage periods. The THM modeling involved simulations of TM, followed by THM simulations. The SNL finite element code Sierra/Aria was used for the simulations described in this part of the report. The three-dimensional TH and THM simulations were executed on the SNL's high performance computing (HPC) system using multiple processors.

1.1 Input Data

The TH and THM simulations utilized various input parameters for a generic salt repository system that includes the intact salt host rock, the excavated Disturbed Zone and the crushed salt backfill material. A detailed analysis of the parameter data collected are given in Jove-Colon et al. (2012, Part VI). Table 1 contains the base case input data used for Sierra/Aria simulations. Below is also a description of a few relevant input parameters that were used in the TH and THM simulations.

Table 1: Base Case material properties and simulation inputs

Property	Intact Salt	DRZ Salt	Crushed Salt
Porosity	0.01	0.014	0.3[a], time varying[b]
Permeability (m^2)	1×10^{-21}	1×10^{-17}	2×10^{-12} [a], function of porosity
Thermal Conductivity (W/m-K)	Function of temperature[c]	Same as Intact salt	Function of temperature and porosity[a,b]
Specific heat (J/kg-K)	931	931	931
Grain density (kg/m^3)	2190	2190	2190
Ref. cap. Pressure (Pa)	5000	5000	5000
Initial temperature (°C)	25	25	25
Initial pressure (Pa)	1.2×10^7	1.2×10^7	1 Atm.
Initial liquid sat.	1.0	0.5	0.05
S_{lr}	0.05	0.05	0.01
Tortuosity	2	2	2
Exponent in diffusivity eqn.	2.334	2.334	2.334
Top Boundary Condition – Const. Pressure (Pa)	1.2×10^7		
Temp. Boundary Condition – Top and Bottom (°C)	25		

[a] For TH simulations only. Thermal conductivity was a function of temperature only.

[b] For THM simulations only. Thermal conductivity was a function of both temperature and porosity.

[c] For all simulations

1.1.1 Permeability-Porosity Function for Crushed Salt

For the THM modeling crushed salt permeability was calculated using porosity data from TM simulations. Figure 1 shows experimental data for compacted crushed salt obtained from Bechthold et al. (1999) and Cinar et al. (2006). The data from both of the references are very similar over the porosity range of 0.1 to 0.3. But the Cinar et al. (2006) permeability-porosity curve covers a wider range of porosity. Thus, a curve fit of the Cinar et al. (2006) data, given by Equation (1), was used for the THM simulations.

$k = 4.866e\text{-}09\ \phi^{4.637}$ (1)

where k = permeability (m^2)

ϕ = porosity

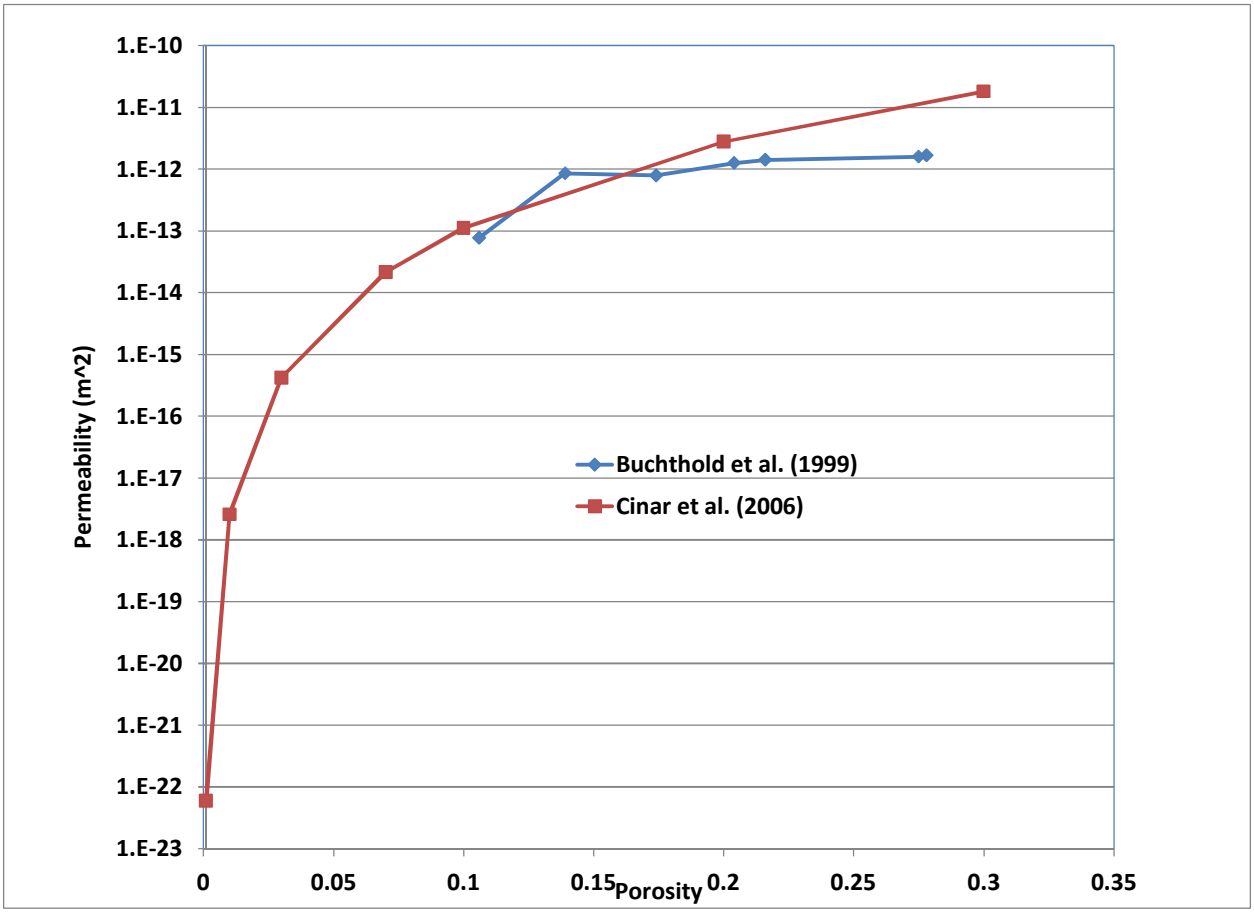

Figure 1. Experimental Permeability-porosity data for crushed salt

1.1.2 Thermal Conductivity of Intact Salt

Figure 2 shows thermal conductivity data of intact salt from different sources. A curve fit of the Pudewills and Droste (2003) data (shown in the figure) was used for TH and THM simulations.

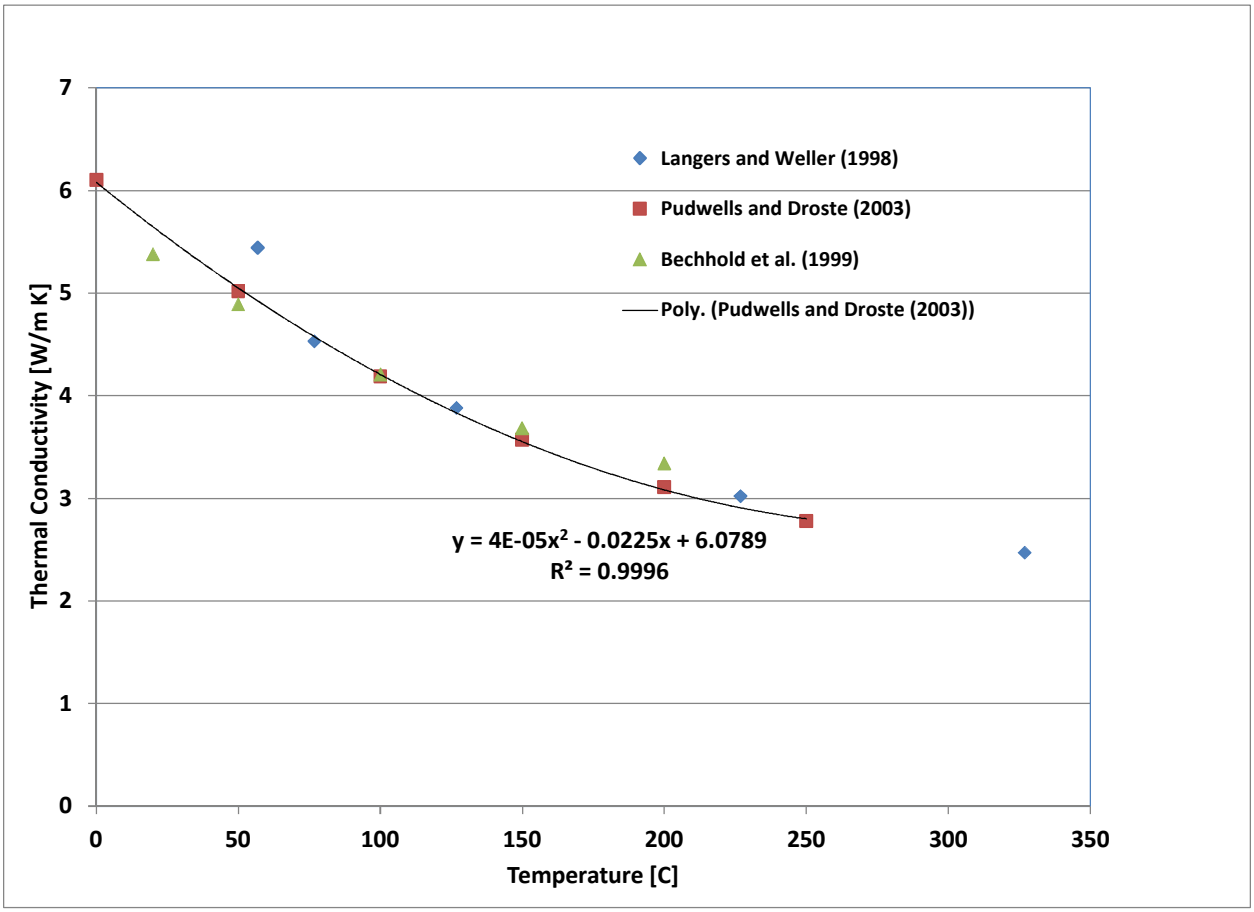

Figure 2. Experimental thermal conductivity-temperature data for Intact Salt

1.1.3 Crushed salt Thermal Conductivity

Compacted crushed salt thermal conductivity varies with temperature and porosity. For the simulations the relationship provided by Bechthold et al. (2004, Figure 2.37) has been used:

$$Kcs(\phi) = -270\phi^4+370\phi^3-136\phi^2+1.5\phi+5 \quad (2)$$

$$Kcs(\phi,T) = Kcs(\phi)[300/Tk)^{1.14} \quad (3)$$

1.2 3-D Thermal-Hydrologic Modeling

Thermal-hydrologic modeling of the generic salt repository system was conducted to identify sensitivity of thermal transport to selected parameters. The same 3-D model geometry and normalized decaying heat used in the coupled TM modeling was applied to the TH and THM simulations. The decaying heat source is a HLW canister represented as a cylinder 0.61 m in diameter and 2.7 m long. The canister has an initial heat load of 8.4 kW, with the decay response described in Clayton and Gable (2009). Half of the canister is located in the DRZ, while the other half is in the crushed salt region. The present study did not look at use of other types of heat sources and thermal loading arrangements. The Sierra/Aria code was used with input data described in Table 1.

The intact salt and the DRZ were assumed to be at an initial temperature of 25°C and a pressure of 12 MPa. The initial pressure was based on WIPP data (Helton et al., 1998). The intact salt was assumed to be at saturated conditions, while an initial liquid saturation of 0.5 was used for the DRZ. The crushed salt was assumed to be at atmospheric pressure with an initial liquid saturation of 0.05.

1.2.1 Effect of DRZ Initial Liquid Saturation

The initial liquid saturation of the DRZ could vary between saturated and dry conditions depending on exposure to ventilation and other repository processes. For the TH and THM modeling the assumed base case DRZ initial liquid saturation is 0.5 (Table 1). To understand the impact of this parameter, values of 0.5, 0.1, and 0.05 (same as the crushed salt) were used. An initial decaying heat source of 1.2 kW was applied, with other input data the same as in Table 1. Thermal conductivities of the intact salt and crushed salt were assumed to vary with temperature according to the curve fits described in Section 1.1. The temperature varying thermal conductivity of the DRZ was assumed to be the same as that of the intact salt.

Simulations results after 5 years of simulation time are shown in Figures 3a to 3c. The results at the selected time show that the temperature response was not sensitive to the DRZ initial liquid saturation values, while vapor migration showed some slight effect. The 0.5 liquid saturation assumed for the base case provides more liquid to the crushed salt area than the other cases. It thus allows more evaporation of water, and thus migration of water vapor. But the water vapor is confined to the DRZ and crushed salt area due to the low permeability of the intact salt and also the relatively low temperature rise.

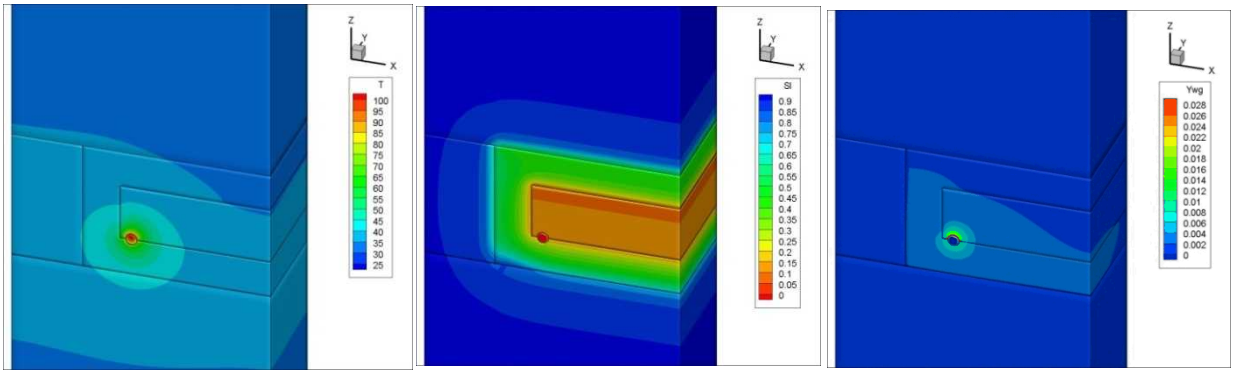

Figure 3a. Distributions of temperature, liquid saturation and mass fraction of water vapor in the gas phase after 5 years. DRZ initial saturation = 0.5, Initial power = 1.2 kW.

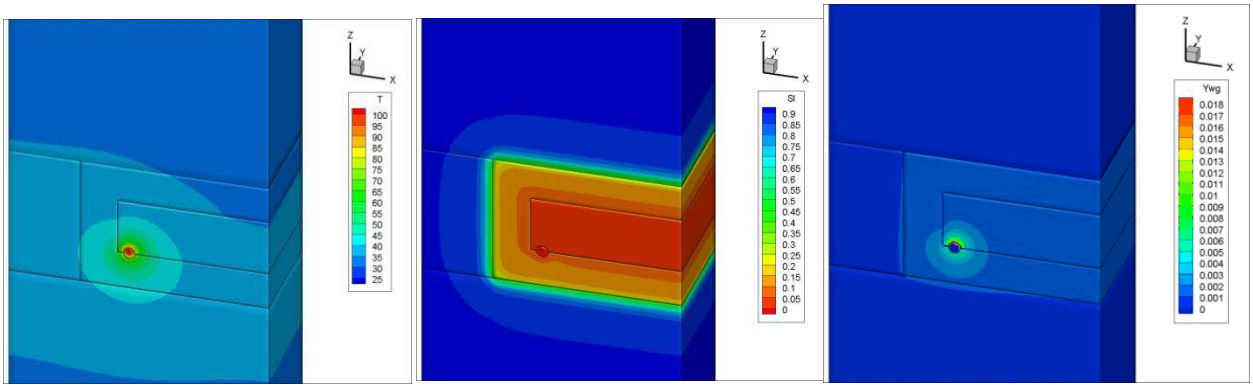

Figure 3b. Distributions of temperature, liquid saturation and mass fraction of water vapor in the gas phase after 5 years. DRZ initial saturation = 0.1, Initial power = 1.2 kW.

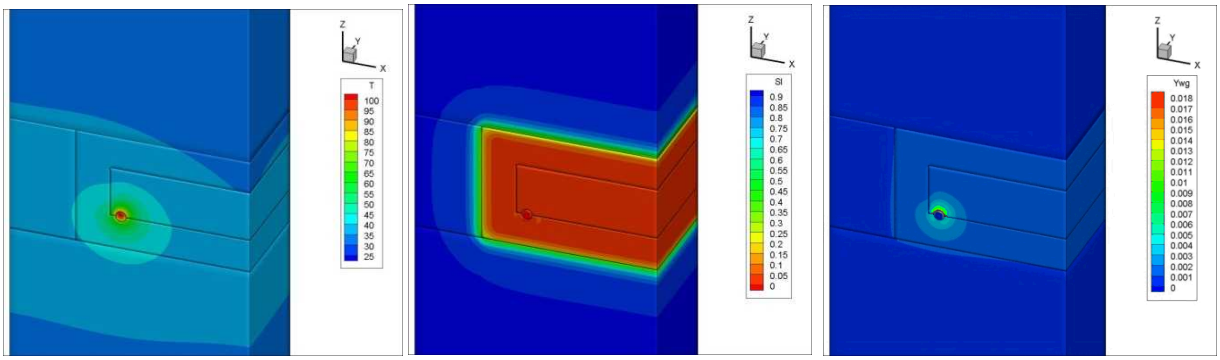

Figure 3c. Distributions of temperature, liquid saturation and mass fraction of water vapor in the gas phase after 5 years. DRZ initial saturation = 0.05, Initial power = 1.2 kW.

1.2.2 Effect of DRZ Permeability

For this case the permeability of the DRZ was varied. Values of 1×10^{-17} m^2 (base case) and 1×10^{-15} m^2 were used. An initial decaying heat source of 1.2 kW was applied, with other input the same as in Table 1. Simulations results after 5 years of simulation time are shown in Figures 3a (for base case permeability) and Figure 4 (for permeability of 1×10^{-15} m^2). The results show that DRZ permeability has minimal effect on temperature response and vapor migration at 5 years of simulation time. The DRZ permeability increase of two orders of magnitude results in increased

movement of fluid between the DRZ and the crushed salt. But it did not result in measurable increased evaporation of water, and thus migration of water vapor. Any water vapor produced is confined to the DRZ and crushed salt area due to the low permeability of the intact salt and also to the relatively low temperature rise.

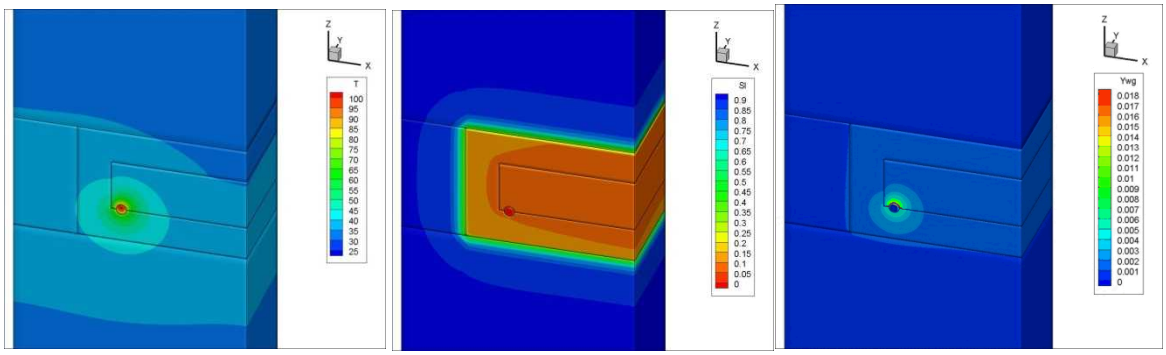

Figure 4. Distributions of temperature, liquid saturation and mass fraction of water vapor in the gas phase after 5 years. DRZ permeability=1 × 10^{-15} m^2, Initial power = 1.2 kW.

1.2.3 Effect of Crushed Salt Compaction

The crushed salt is subject to compaction or creep closure as a result of the overburden. The process of compaction and reconsolidation is represented in the TM and THM simulations (Section 1.3). In this exercise the crushed salt is assumed to have already undergone the process of compaction, and it is further assumed that it acquires properties of the DRZ. The purpose of the exercise is to compare thermal response for un-compacted conditions (base case) and post-compaction conditions for the entire duration of simulation. It is assumed that the two conditions cover the range of possible thermal responses. For the simulations an initial decaying heat source of 2.4 kW was applied, with other input being the same as in Table 1.

Modeling results after 5 years of simulation time are shown in Figures 5a and 5b. The results show that compaction of the crushed salt to properties of the DRZ have a significant effect on peak temperature response. The compaction also resulted in increased spread of the thermal front into the intact salt, for the selected observation time. The reduced peak temperature and the increased thermal spread can be attributed mainly to the change in thermal conductivity of the crushed salt. For the base case, the thermal conductivity of the crushed salt is much lower than that of the intact salt, resulting in less propagation of heat, and thus a higher peak temperature. The compacted case assumes that the crushed salt thermal conductivity is the same as that of the DRZ and intact salt. Thus, use of the higher thermal conductivity for the crushed salt results in more propagation of heat, and a lower peak temperature. Movement of fluid is a function of the thermal processes and also the hydraulic properties of the compacted crushed salt. For the base case the crushed salt is at a much lower initial liquid saturation than the DRZ, causing initial liquid movement towards the crushed salt. For the compacted case both the crushed salt and the DRZ are assumed to be at the same initial liquid saturation, removing the saturation gradient. In

addition, the reduced porosity and permeability of the crushed salt for the compacted case would result in reduced movement of fluid within the crushed salt and the DRZ. The reduced peak temperature has also affected water vapor generation, as shown in Figure 5b.This figure shows transport of trace amounts vapor reaching the intact salt, likely as a result of mass diffusion.

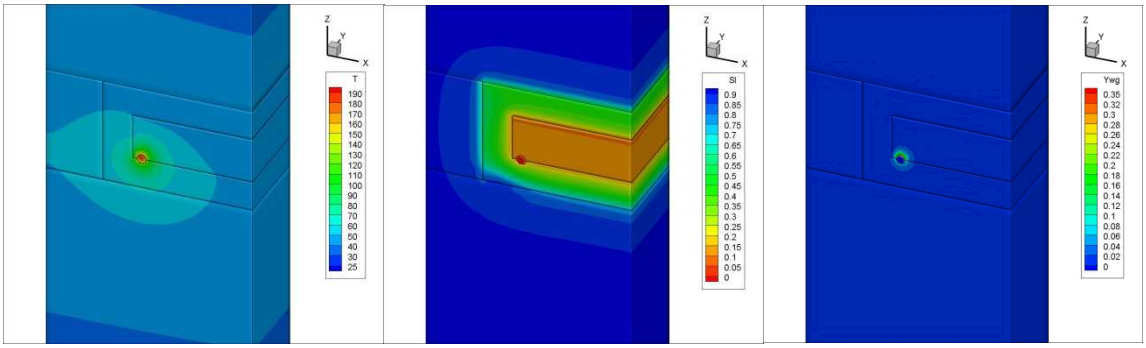

Figure 5a. Distributions of temperature, liquid saturation and mass fraction of water vapor in the gas phase after 5 years. Crushed Salt: porosity = 0.3, permeability=2 × 10^{-12} m^2, Sli = 0.05, Pi = 1 Atm. Power = 2.4 kW.

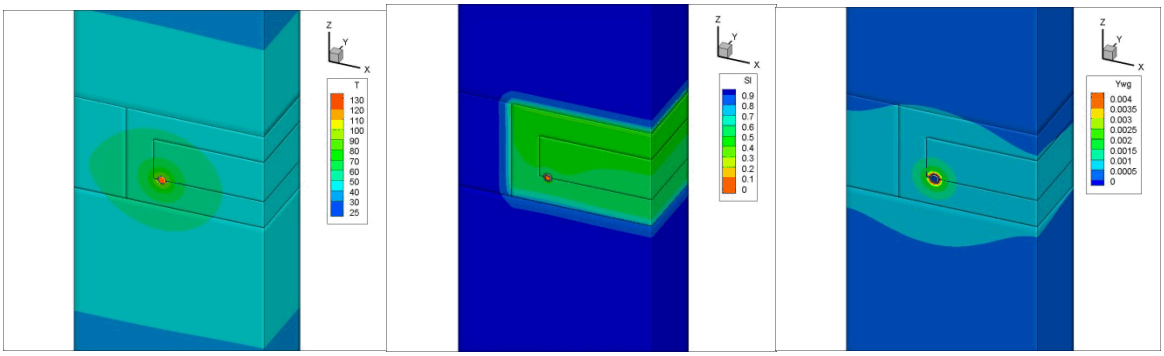

Figure 5b. Distributions of temperature, liquid saturation and mass fraction of water vapor in the gas phase after 5 years. Crushed Salt: porosity = 0.014, permeability=1 × 10^{-17} m^2, Sli = 0.5, Pi = 12 MPa (Same as DRZ). Power = 2.4 kW.

1.3 Thermal-Hydrologic-Mechanical Modeling

The process of compaction and consolidation of the crushed salt alters the physical conditions as well as thermal-hydrology of the salt repository. To capture all the physical and thermal processes a fully coupled THM modeling would be required. Fully coupled THM modeling in a salt repository will be the subject of future work. In this section a one-way THM coupling is presented. In the one-way coupling, outputs of TM simulations are used in TH simulations but the TH outputs are not fed back to the TM model. As described in Section 1.0, TM simulations were first carried out to provide data of average porosity as a function of time for the crushed salt. The TM simulations and associated assumptions are described in the TM section of this report. The average porosity-time data were then used to generate the corresponding average permeability-time data using Equation (1). Thermal conductivity of the crushed salt was

calculated as a function of temperature and porosity using Equations (2) and (3). The average porosity-time data were used in the thermal conductivity equations. The crushed salt thermal conductivity equations were implemented in a separate plug-in code initially used in Clayton (2010). Note that even with simplifications of the one-way coupling as well as averaging of crushed salt porosity the simulations adequately model thermal-hydrologic-mechanical processes in a generic salt repository.

THM simulations were conducted using the time varying porosity and permeability of crushed salt, as well as crushed salt thermal conductivity as a function of porosity and temperature. For the analysis decay heat sources with surface storage times of 50, 75, 80 and 90 years were used. The Sierra/Aria code was used with input data described in Table 1.

Initial conditions were the same as for the TH simulations. The intact salt and the DRZ were assumed to be at a temperature of 25°C and a pressure of 12 MPa. The initial pressure was based on WIPP data (Helton et al., 1998). The intact salt was assumed to be under saturated conditions, while an initial liquid saturation of 0.5 was used for the DRZ. The crushed salt was initially assumed to be at atmospheric pressure with a liquid saturation of 0.05. Simulations were then carried out to total time of 10 years.

Maximum temperature output for the selected surface storage cases are described in Figures 6 and 7. Figure 6 shows maximum canister surface temperature versus storage time. Figure 7 shows maximum canister surface temperature versus initial power. The results represented by both of these figures are in line with results of repository thermal analysis by Hardin et al. (2012). Figure 7 shows a straight line relationship between maximum temperature and initial power. This is similar to Hardin et al. (2012, Appendix D) for disposal in salt, although the slope of the line is different. Further analysis would be needed to identify the differences between the results of the analytical method of Hardin et al. (2012, Appendix D) and this work. However, the results of both methods indicate that peak temperature is linearly correlated to initial power, and that one way of regulating peak canister temperatures is by regulating the initial power or the surface storage time.

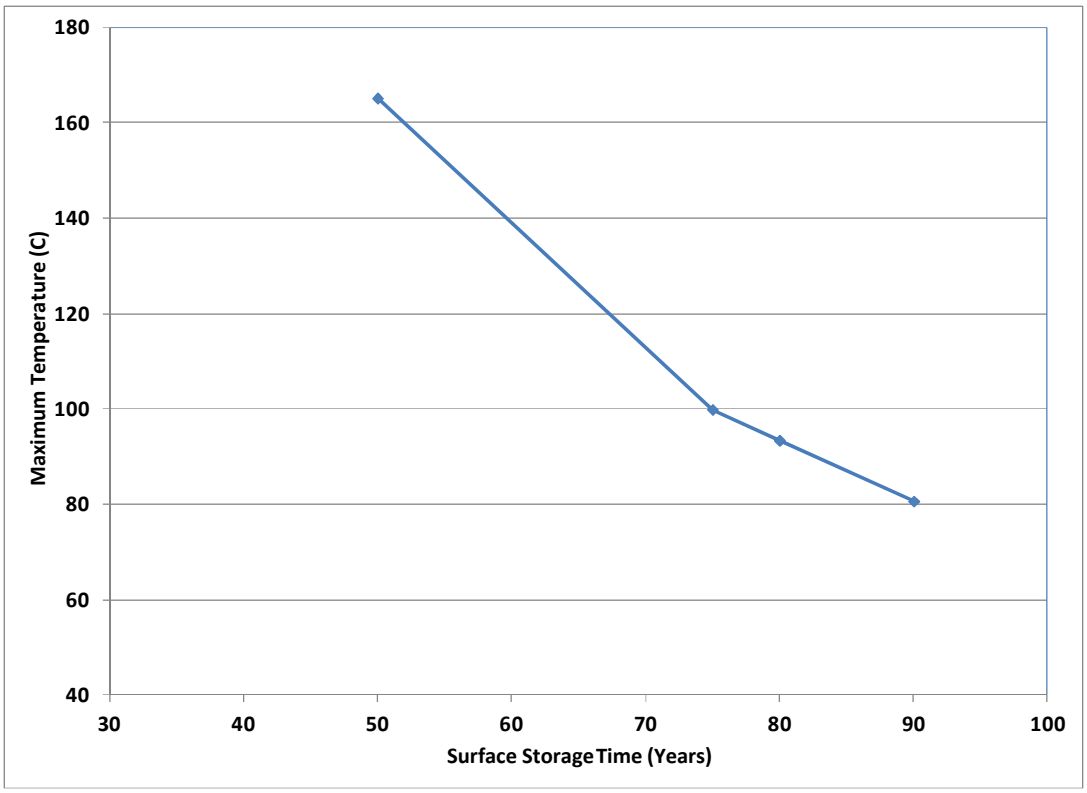

Figure 6. Maximum canister temperature vs. duration of surface storage

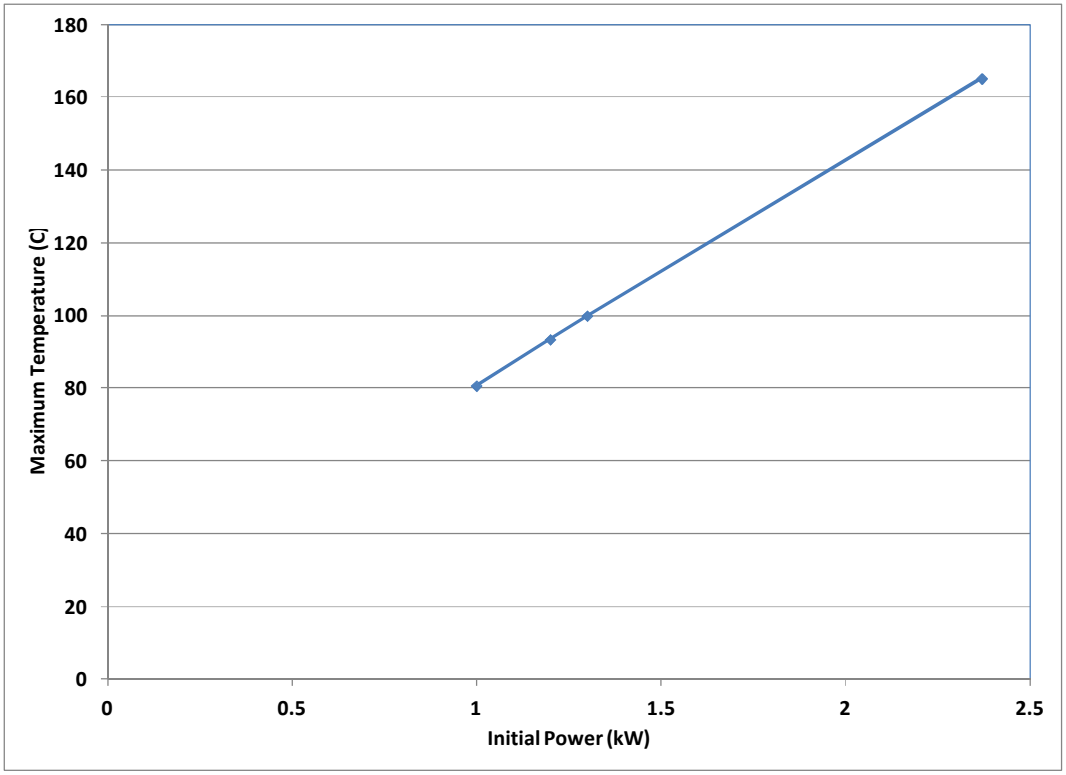

Figure 7. Maximum canister temperature vs. initial power

Figure 8 shows distributions of temperature, liquid phase saturation and mass fraction of vapor in the gas phase at 5 years simulation time, for the case with 50 years of surface storage. After 5 years the TM predicted crushed salt porosity is about 0.1, from the initial porosity of 0.33. The crushed salt thermal conductivity at the reduced porosity is significantly higher than the initial crushed salt value. This has resulted in a lower peak temperature and reduced vapor production compared to those of Figure 5a, where no compaction had occurred. The consolidation has not quite reached that of Figure 5b, where the compacted porosity is 0.014.

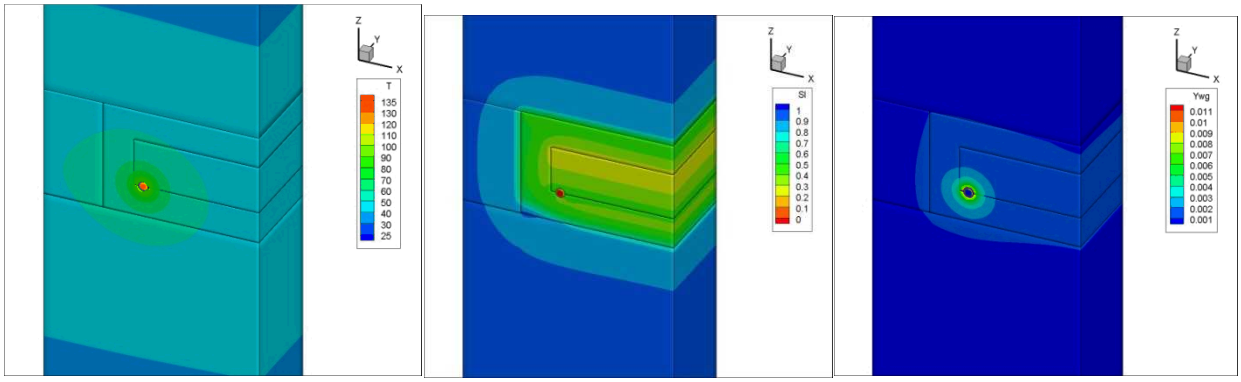

Figure 8. Distributions of temperature, liquid saturation and mass fraction of water vapor in the gas phase after 5 years - 50 years storage.

Simulation results of the 50-year surface storage modeling case were further analyzed at different locations in the crushed salt and DRZ. Figure 9 indicates locations of nodes where results were obtained. Figure 10 shows temperature versus time plot for the selected nodes. As expected, Node 735 on the surface of the canister has the highest temperatures, with peak temperatures decreasing for nodes further from the canister. Temperatures also decrease with time, as the heat decays with time. Figures 11 and 12 show the corresponding liquid saturation and mass fraction of vapor in the gas phase, respectively. Nodes inside the crushed salt start with liquid saturation of 0.05. Liquid saturations then increase with re-saturation from the DRZ. Nodes inside the DRZ start with liquid saturation of 0.5. Node 37885, just below the canister, has its liquid saturation decreasing at early time due to vaporization and fluid movement in the DRZ. The evaporated fluid is condensed in cooler regions. Figure 12 shows the nodes closest to the heat source with the highest mass fraction of vapor in the gas phase (Nodes 747 and 37885).

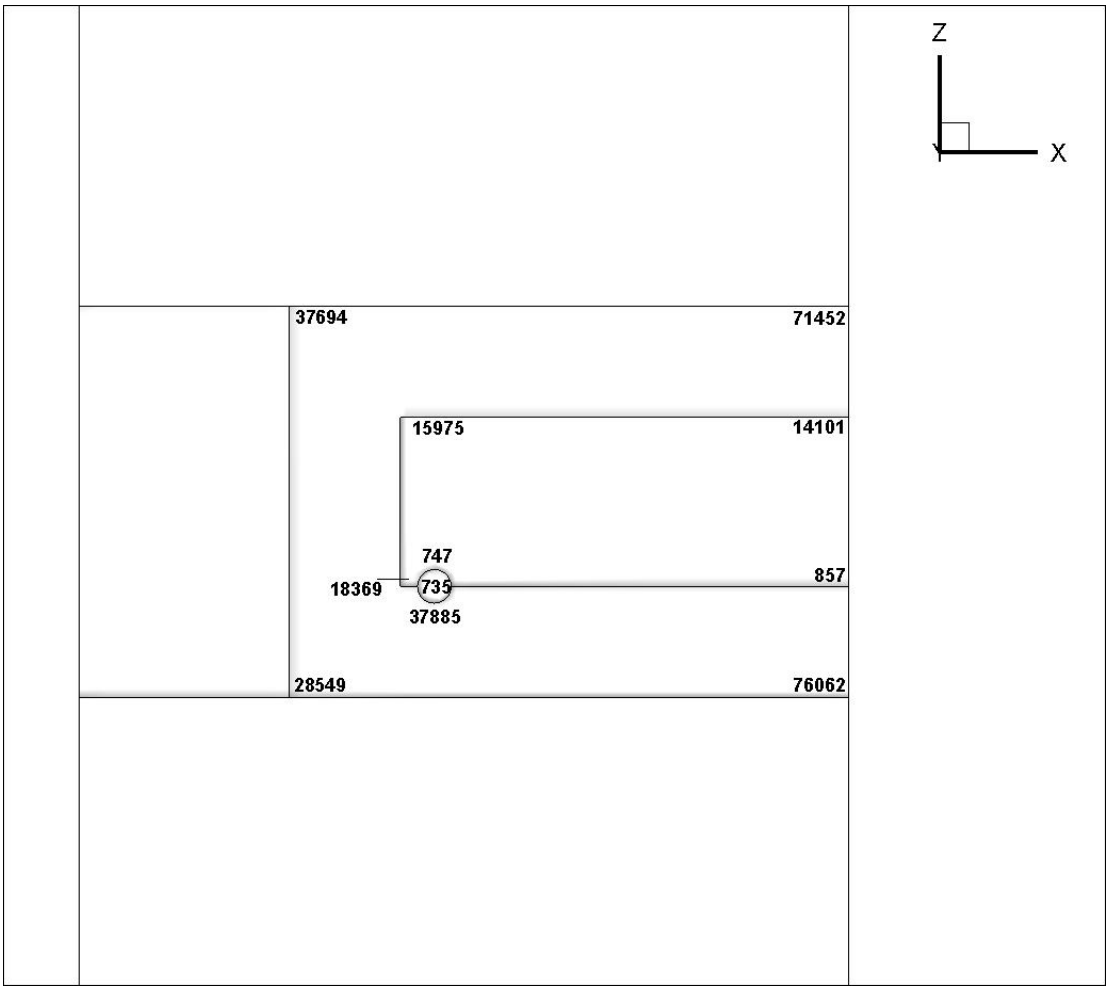

Figure 9. Locations of selected nodes.

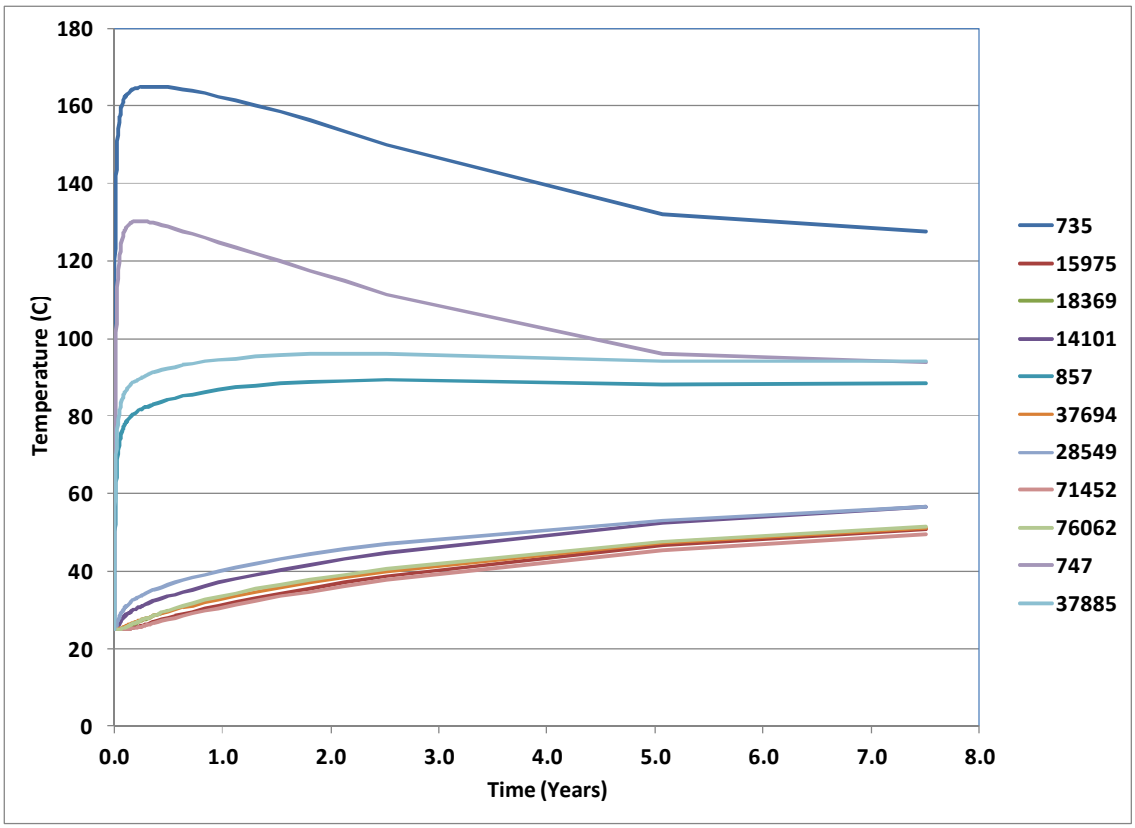

Figure 10. Temperature vs. time, at different locations - 50 years storage

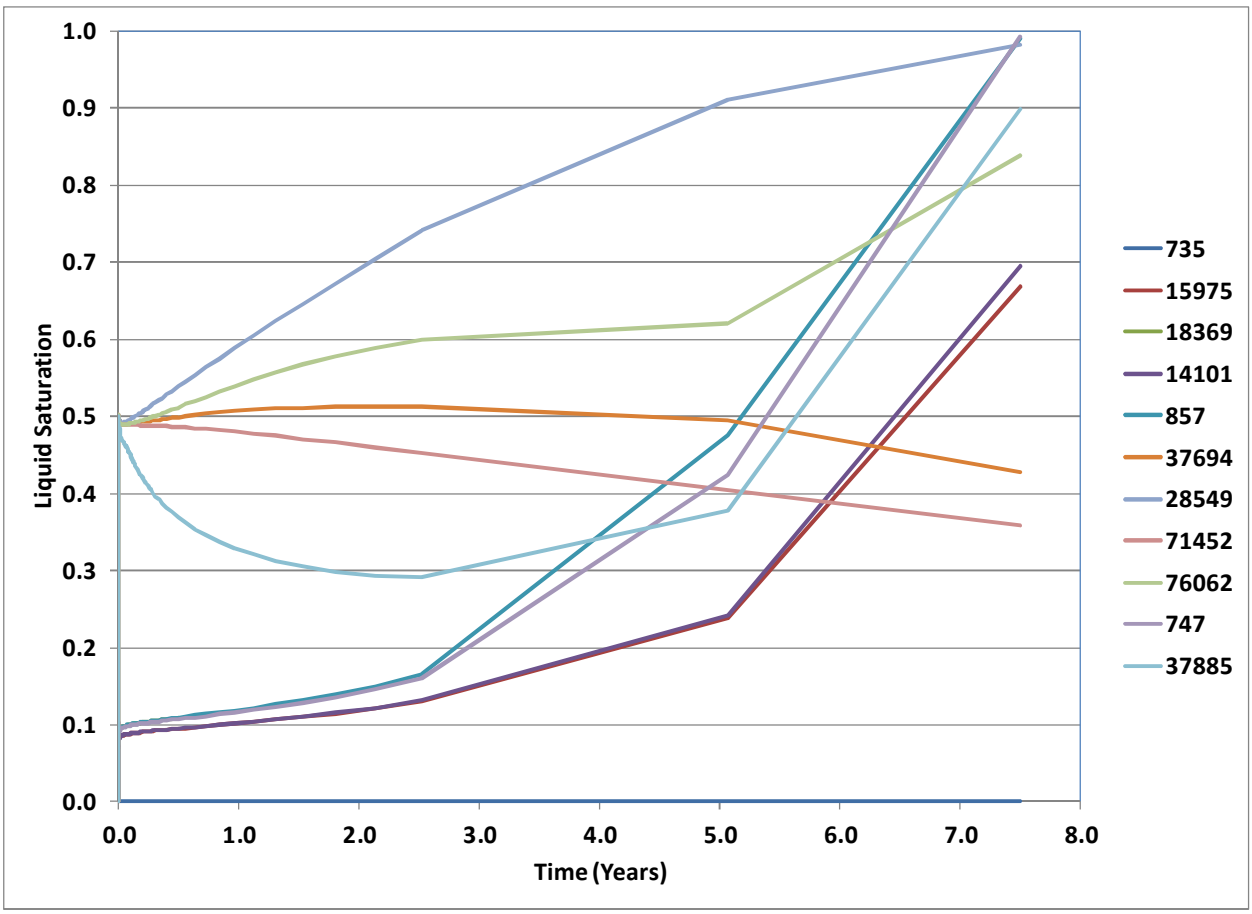

Figure 11. Saturation vs. time, at different locations, 50 years storage.

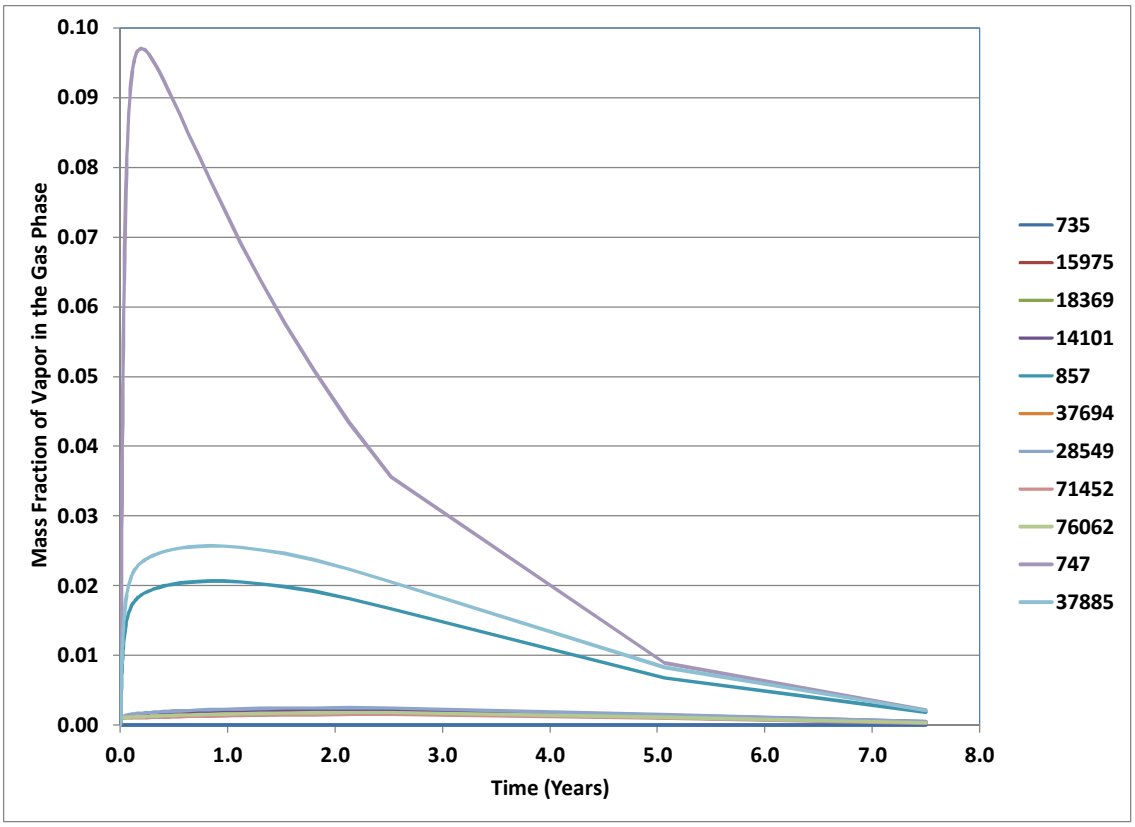

Figure 12. Mass fraction of vapor in the gas phase vs. time, at different locations, 50 years storage

Figure 13 shows temperature at the surface of the canister (Node 735) versus time, for different surface storage times. The results are generally in line with those of Hardin et al. (2012, Section 3). Figures 14 and 15 show liquid saturation versus time at nodes above and below the canister, for different surface storage times. Figure 14 shows liquid saturation at Node 747, located inside the crushed salt. The results indicate the continuous porosity decline as a result of compaction, even though evaporation occurs at the same time. Node 37885, located inside the DRZ, is not subject to the porosity changes. It also has an initial liquid saturation of 0.5, much higher than at Node 735. Figure 16 shows temperature versus time at the surface of the canister (Node 735) for the 50-year storage time modeling. The figure shows temperature for the THM case compared with the cases of no compaction of crushed salt, and compaction of crushed salt to DRZ conditions, described in Section 1.2.3. As discussed in Section 1.2.3 the un-compacted case has the highest temperatures. As shown in Figure 1.16, at later times the temperature profile for THM case follows that of the compacted case. This is the result of the drop in porosity in the THM case.

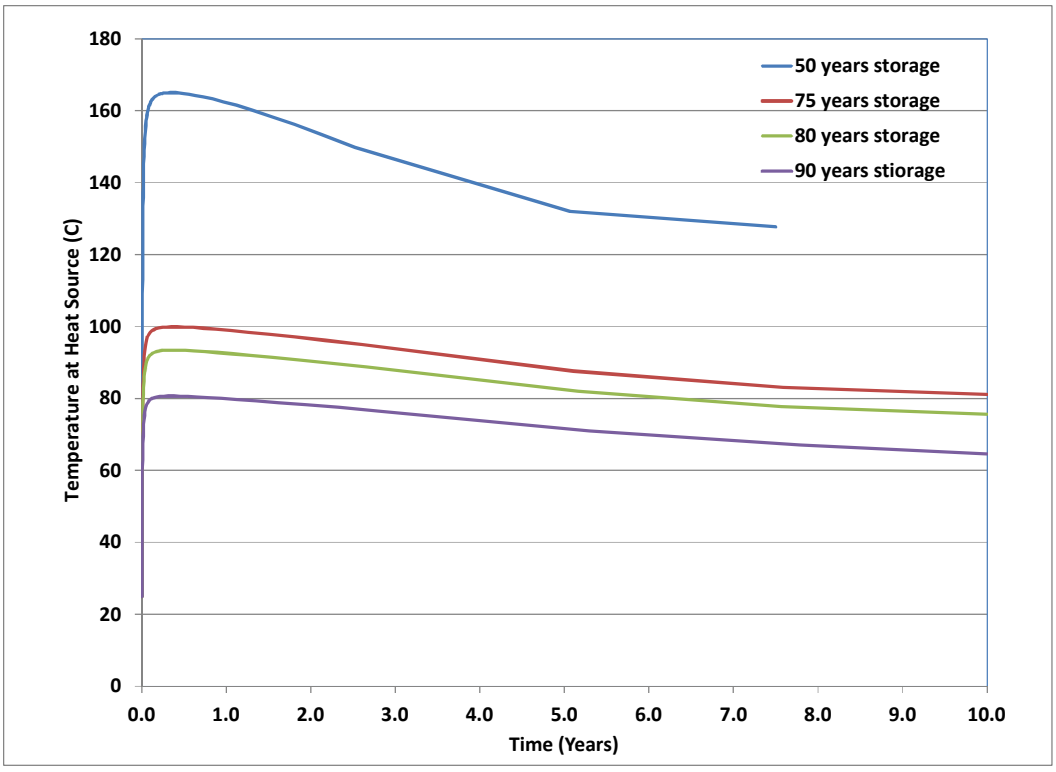

Figure 13. Temperature vs. time at heat source (Node 735) for different surface storage times

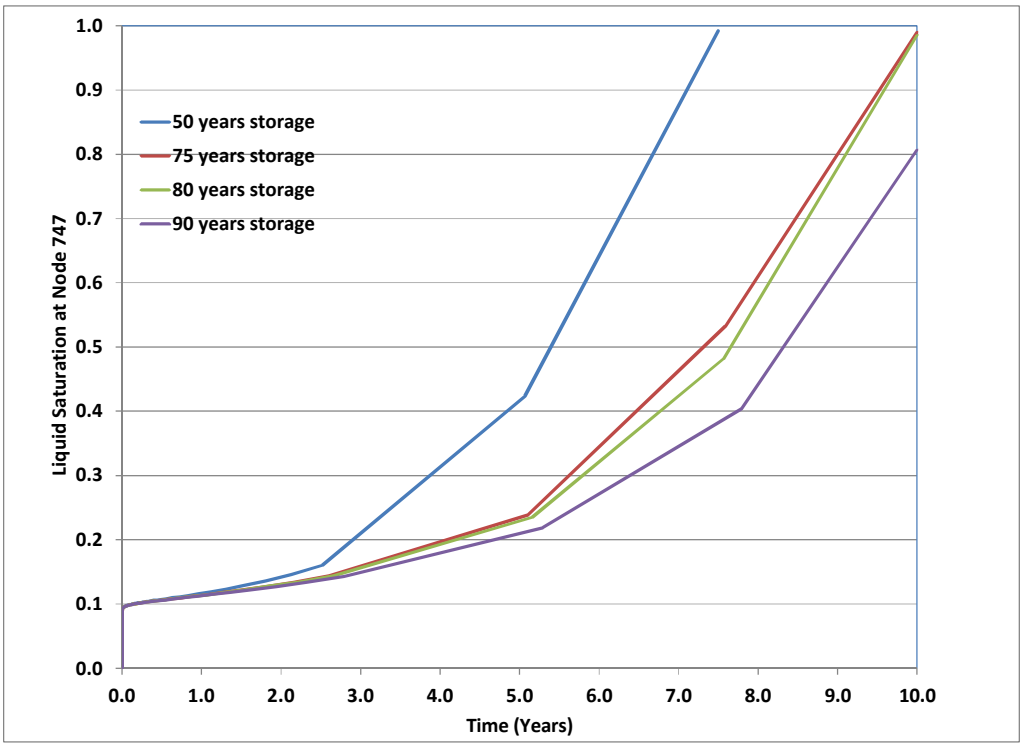

Figure 14. Liquid saturation vs. time at a location above heat source (Node 747) for different surface storage times

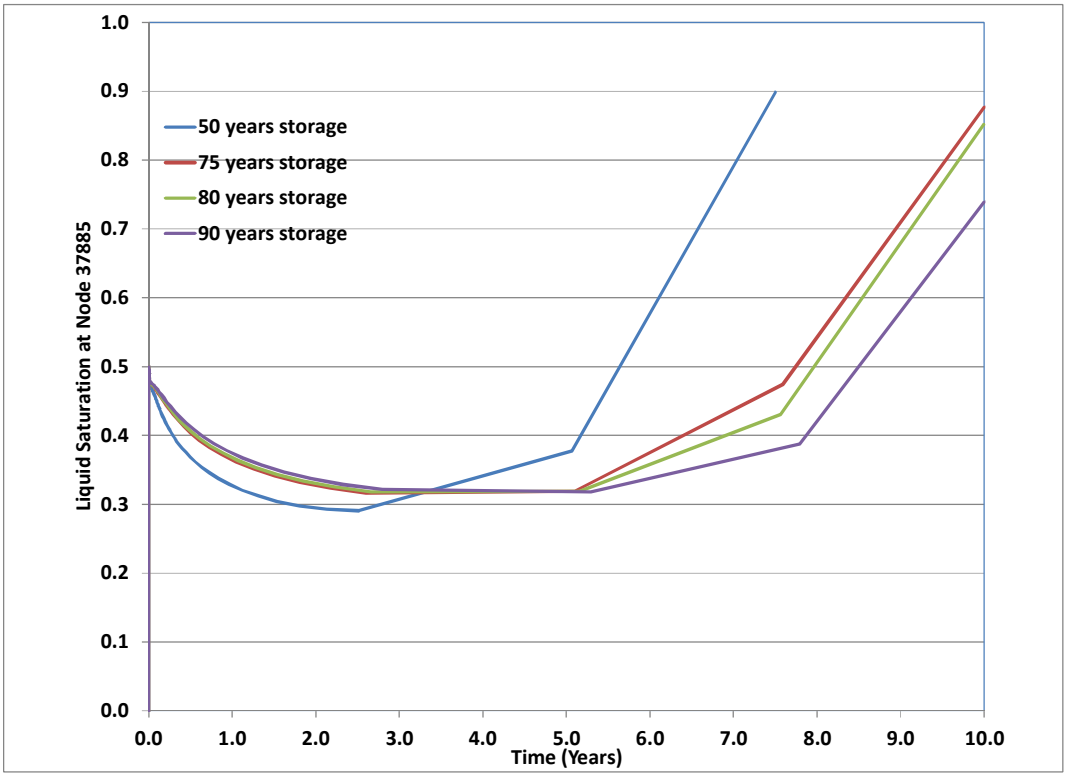

Figure 15. Liquid saturation vs. time at a location below heat source (Node 37885) for different surface storage times

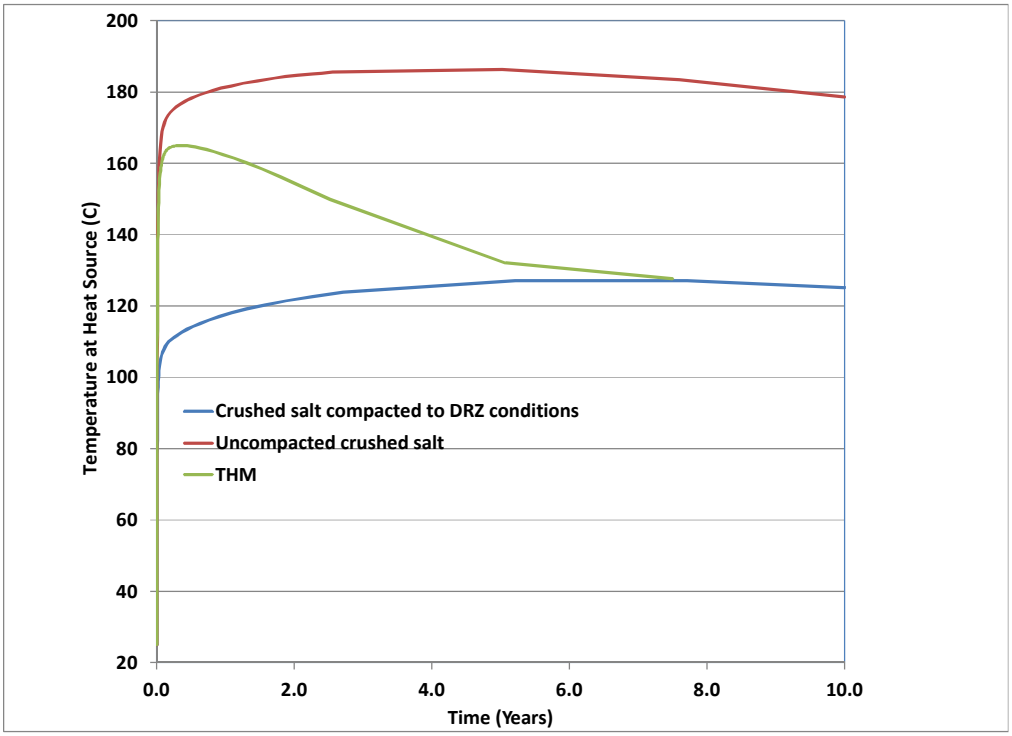

Figure 16. Temperature vs. time at heat source (Node 735) for cases of THM, no compaction of crushed salt, and compaction of crushed salt to DRZ conditions. 50 year surface storage time.

1.4 Summary of TH and THM Modeling

The TH and THM modeling in a generic salt repository provide preliminary output describing the thermal and hydrologic processes in a generic salt repository undergoing crushed salt consolidation. The simulations provided distributions of temperature, saturation and mass of vapor for different input conditions, predicting thermal and moisture front propagation. The simulations also provided sensitivity of output to DRZ and crushed salt parameters. Comparison of peak temperature predictions at different surface storage times with those of analytical methods of Hardin et al. (2012) indicated similar trends. The peak canister surface temperature is mainly a function of waste type, surface aging, and also consolidation of backfill (see Figure 16). Propagation of vapor away from the heat source is limited by the nearly-impermeable intact salt, consolidation of the crushed salt, and the thermal decay of the heat source. The results show that at high heat loads vapor migrates mainly within the un-consolidated backfilled regions, and to a lesser extent within the DRZ. In contrast thermal propagation reaches well into the intact salt, mainly as a result of conduction.

The modeling exercises used SNL's Sierra Mechanics platform and software, as well has high performance computing. Use of such capabilities allowed large scale simulations with the help of multiple processors. Such capabilities will also be of importance for future fully-coupled THM simulations.

Recommendations for future work include:

- A two-way coupled 3-D THM modeling.
- Use of different geometries to accommodate different thermal loading scenarios and to avoid effects on boundary conditions.
- Use of different heat sources.
- Use of a different representation of the DRZ and parameters.
- Representation of salinity in fluids.

2. References

Bechthold, W., Rothfuchs, T., Poley, A., Ghoreychi, M., Heusermann, S., Gens, A., and Olivella, S. 1999: BackBackfilling and Sealing of Underground repositories for Radioactive Waste in Salt (BAMBUS Project), Nuclear Science and Technology, Project report, European Commission, EUR 19124 EN.

Bechthold, W., Smailos, E., Heusermann, S., Bollingerfehr, W., Bazargan Sabet, B., Rothfuchs, T., Kamlot, P., Grupa, J., A., Olivella,S., and Hansen, F. D. 2004: BackBackfilling and Sealing of Underground repositories for Radioactive Waste in Salt (BAMBUS II Project), Nuclear Science and Technology, Project report, European Commission, EUR 20621 EN.

Cinar, Y., Pusch, G., and Reitenbach, V. 2006. Petrophysical and Capillary Properties of Compacted Salt, *Transport in Porous Media* 64: pp. 199-228. Springer 2006.

Clayton, D. J., and Gable, C. W. 2009. 3-D Thermal Analyses of High Level Waste Emplaced in a Generic Salt Repository, SAND2009-0633P, Sandia National Laboratories, Albuquerque, NM.

Clayton, D.J. 2010. Thermal Analyses of a Generic Salt repository with High-Level Waste-10429, Waste management 2010 Conference, March 7-11, 2010, Phoenix, AZ.

Hardin, E., Hadgu, T., Clayton, D., Greenburg, H., Blink, J., Sharma, M., Sutton, M., Carter, J., Dupont, M., and Rodwell, P., 2012. *Disposal Concepts/Thermal Load Management (FY11/12 Summary Report)*. FCRD-USED-2012-000219 Rev. 1. September, 2012. U.S. Department of Energy, Used Fuel Disposition R&D Campaign.

Helton, J.C., J.E. Bean, J.W. Berglund, F.J. Davis, K. Economy, J.W. Garner, J.D. Johnson, R.J. MacKinnon, J. Miller, D.G. O'Brien, J.L. Ramsey, J.D. Schreiber, A. Shinta, L.N. Smith, D.M. Stoelzel, C. Stockman, and P. Vaughn 1998. *Uncertainty and Sensitivity Analysis Results Obtained in the 1996 Performance Assessment for the Waste Isolation Pilot Plant*. SAND98-0365. Albuquerque, NM: Sandia National Laboratories.

Langer, M. and Wallner, M. 1998. Evaluation of Repository Concepts for the Disposal of Spent Fuel on the Basis of Geotechnical Safety Indicators and Exploration Data. Radioactive Waste Management and Disposal, Nuclear Technology, Vol. 121, p. 199-211.

Pudewills, A. and Droste, J., 2003, Numerical Modeling of the Thermomechanical Behavior of a Large-Scale Underground Experiment. Computers and Structures, vol. 81, p. 911-918. Elsevier Science Ltd.